Photoproduction of ρ^0 and Two–photon Production of Lepton Pairs in Ultra–peripheral Pb–Pb Collisions at the CERN LHC

Kyrre Skjerdal

Dissertation for the degree of Philosophiae Doctor (PhD)

Department of Physics and Technology
University of Bergen

March 2014

Acknowledgements

It has been eight years since I started my studies in the experimental heavy–ion physics group in Bergen. It has been eight remarkable years. I have learnt a lot of physics, met a lot of interesting people, some of which I now call friends. I have also travelled to places, I probably wouldn't have visited otherwise.

First of all I would like to thank my main supervisor Joakim Nystrand for excellent guidance through my Ph.D. studies. You have always been available. easy to talk to, and always helpful answering my sometimes simple questions. It has been a pleasure to be your student!

I would also like to thank my co-supervisor Dieter Röhrich for interesting discussions about physics, politics, music and life in general. A special thanks goes to your wife Bianca for excellent food during the group dinners at your home.

In my work I have been part of the ALICE ultra–peripheral collisions analysis working group. To work with such a skilled group has been very educational. A special thanks goes to Christoph Mayer who has helped me a lot with my analysis. Other people that have given me valuable input are Eugenio Scapparone, Daniel Tapia Takaki, Daniele De Gruttola, Andrea Agostinelli, and Jürgen Schukraft.

During the years of my Ph.D. studies I have shared office with different persons: Ketil Røed, Lijiao Liu, Njål Brekke, and Attiq Ur Rehman. It has always been a pleasure being office mates with you. Thanks for all the conversations about physics and non-physics topics. I have also met many nice people through my work in Bergen and at CERN: Kenneth Aamodt, Dag Toppe Larsen, Øystein Djuvsland, Øystein Haaland, Sedat Altinpinar, Hege Erdal, Kalliopi Kanaki, Matthias Richter, Håvard Helstrup, Krisin Fanebust Hetland, Boris Wagner, Kristian Ytre-Hauge, Camilla Stokkevåg, Per-Ivar Lønne, Per-Thomas Hille, Svein Lindal, Henrik Qvigstad, Trine Tveter, Jochen Thaeder, and Torsten Alt. A special thanks goes to Øystein Djuvsland for inviting me to his first date with his girlfriend Julia. It has been a pleasure to learn to know you all! Sorry, to the ones I might have forgotten.

The biggest thanks goes to my beloved and loving girlfriend Hege Beate Kronen. Your patience and support has been remarkable! My daughter Hedda, and my son Vinjar gives me so much joy in life. Thank you for always making me smile, and for taking my mind away from working. To my parents Marit Skjerdal and Lars Kjøde, and my brother Vegard: Your support has meant a lot to me!

Last but not least I would like to mention the man who sparked my interest in physics and science in general, my former teacher Erik Torp "Torpen" Nilssen.

Bergen, March 2014

Kyrre Skjerdal

Abstract

This thesis is based on the analysis of ultra–peripheral collisions collected by the ALICE Collaboration at the CERN LHC. ALICE is a general purpose detector designed to study heavy-ion collisions at ultra–relativistic energies with the purpose of investigating the properties of strongly interacting matter, similar to the matter that existed shortly after the Big Bang.

In this analysis the charged particle tracking system of the central barrel in ALICE is used. The tracking system consists of an Inner Tracking System, with six layers of silicon detectors, and a large Time Projection Chamber. Trigger information is provided by the following detectors: The Silicon-Pixel Detector (SPD), a part of the Inner Tracking System; the Time–Of–Flight (TOF), located outside the TPC; the V0 detectors, plastic scintillators located outside of the central barrel, covering roughly two units of pseudorapidity on either side of mid-rapidity.

Ultra–peripheral collisions are collisions between hadrons, they can be protons or nuclei, where they geometrically miss each other. This implies that the impact parameter is larger than two times the radii of the colliding hadrons. Because of the short range of the strong force, the interactions will be mediated by the electromagnetic field. The electromagnetic field of a moving charged particle can be treated as a flux of virtual photons. Ultra-peripheral collisions can be divided into two categories: two-photon and photonuclear interactions. In a photonuclear interaction a photon from the field of one of the nuclei interacts with the other (target) nucleus. In two–photon interactions one photon from each nucleus interacts and create for example a lepton pair.

In this thesis the focus is the analysis of coherent photoproduction of the vector meson $\rho^0$and two–photon production of e^+e^- pairs. First an introduction to heavy–ion physics and the physics of ultra–peripheral collisions is given and then ALICE detector is described. In the following the analysis procedure is discussed: How the events are reconstructed; the event selection, track cuts and particle identification; how the selected events are corrected for acceptance and efficiency; and how the luminosity of the data set is estimated. In the end the physics results of this thesis are presented. The method for signal extraction, error estimation, and cross section calculation for photoproduction of ρ^0 is described, and the resulting differential cross section is presented. For the process $\gamma\gamma \to e^+e^-$ the event characteristics, event selection and cross section calculation is discussed. The differential cross section for the mass interval $0.45 \leq M_{inv} \leq 2.5$ and with pseudorapidity $|\eta| < 1.5$, and the differential cross section as a function of invariant mass is presented.

Contents

Chapter 1

Introduction

This thesis is based on results obtained from collisions between heavy nuclei at the CERN Large Hadron Collider (LHC). The LHC is the largest accelerator for subatomic particles in the world. It has a circumference of 27 km and is located outside Geneva at the Swiss–French border (see Figure 1.1). The LHC is a storage ring where protons

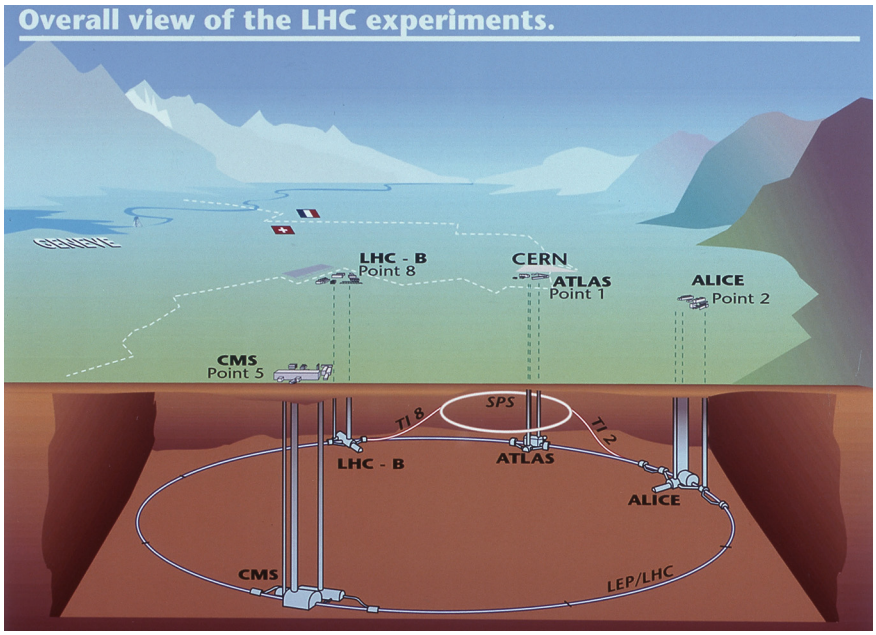

Figure 1.1: An overview of the Large Hadron Collider and its experiments[1].

or heavy nuclei circulate in opposite directions. The particles are brought to collide at certain collision points, which are surrounded by detectors.

The purpose of colliding subatomic particles at higher and higher energies is to obtain a knowledge of the structure of matter at the deepest levels. This can be achieved by discovering new and fundamental particles, such as the recently discovered Higgs boson [2, 3], or by further elucidating the structure of complex nuclei and other states of nuclear matter.

The particles accelerated at the LHC, protons and heavy nuclei, consist of quarks and therefore interact via the strong nuclear force. They do, however, also posses an electric charge and having purely electromagnetic interactions is also possible. The latter type of interactions is the main topic of this thesis.

The data in this thesis have been obtained in ultra–peripheral collisions at the ALICE experiment. Ultra–peripheral collisions are collisions between hadrons, they can be protons or nuclei, where they geometrically miss each other. This implies that the impact parameter is larger than two times the radii of the colliding hadrons. For light vector meson production in Pb–Pb collisions at LHC energy, the median impact parameter is usually in the range 200 – 300 fm. Because such impact parameters are much larger than the short range of the strong interaction, the interactions will be mediated by the electromagnetic field. In this thesis the main topic has been the study of photoproduction of the light vector meson ρ^0, and the interaction where two photons collide and produce a e^+e^- pair, $\gamma\gamma \to e^+e^-$.

This thesis is organised is the following way: Chapter 2 contains a summary of heavy–ion physics, Chapter 3 gives an overview of the physics of ultra–peripheral collisions, Chapter 4 contains a description of the experimental set up at the ALICE experiment, Chapter 5 explains the data analysis method, and in Chapter 6 the physics results are presented. At the end, in Chapter 7, there is a summary and conclusion of the thesis.

Chapter 2

Introduction to Heavy–Ion Physics

The first experiments with ultra-relativistic nuclear collisions were performed with cosmic rays in the 1950's and 60's. Cosmic rays were used, since no accelerator at the time could reach high enough energies. Later accelerators were built and used for this purpose. The Alternating Gradient Synchrotron (AGS) at the Brookhaven National Laboratory (BNL) and the Super Proton Synchrotron (SPS) at CERN both started with fixed target heavy–ion collisions in 1986. At the AGS ^{16}O, ^{28}Si and ^{197}Au were accelerated with center of mass energies from $\sqrt{s_{NN}} = 4.9$–5.4 GeV, whereas at the SPS ^{16}O, ^{32}S, and ^{208}Pb were accelerated with energies up to $\sqrt{s_{NN}} = 19.4$ GeV. Here $\sqrt{s_{NN}}$ is the center–of–mass energy per nucleon pair.

To reach higher energies there has been a change of regime from fixed target experiments to colliders. The Relativistic Heavy Ion Collider (RHIC) at BNL started operation in 2000. RHIC accelerates gold ions (^{197}Au) to a beam energy of 100 GeV per nucleon, giving a center–of–mass energy of $\sqrt{s_{NN}} = 200$ GeV per nucleon pair. In addition to Au+Au collisions, the RHIC experiments has studied p+p, d+Au, Cu+Cu and Cu+Au collisions. At the present time there are two experiments operational at RHIC, STAR and PHENIX. The former experiments PHOBOS and BRAHMS ended their operation in 2005 and 2006, respectively.

The LHC is the latest generation accelerator for high energy physics. An overview of the LHC and the experiments is shown in Figure 1.1 The LHC started operation with a short run of proton–proton collisions with center–of–mass energy $\sqrt{s} = 900$ GeV in 2009. Later there have been proton–proton runs in 2010, 2011 and 2012 with center of mass energies of 7 – 8 TeV. In November and December 2010 the LHC had its first run with Pb–Pb collisions, with $\sqrt{s_{NN}} = 2.76$ TeV. In late 2011 there was another Pb–Pb run, and in January and February 2013 the first p–Pb collisions were collected.

There are four main experiments at the LHC, ATLAS (A Large LHC Apparatus), CMS (Compact Muon Solenoid), LHCb (LHC beauty) and ALICE (A Large Ion Collider Experiment). ATLAS and CMS are general purpose detectors for elementary particle physics, designed to search for new physics, including Higgs searches. The LHCb is a specialized b–physics experiment, designed to study CP-violation in the decay of b–quarks. ALICE which is designed to mainly study heavy–ion collisions, will be described in more detail in Chapter 4

2.1 Basic variables of Heavy–Ion Collisions

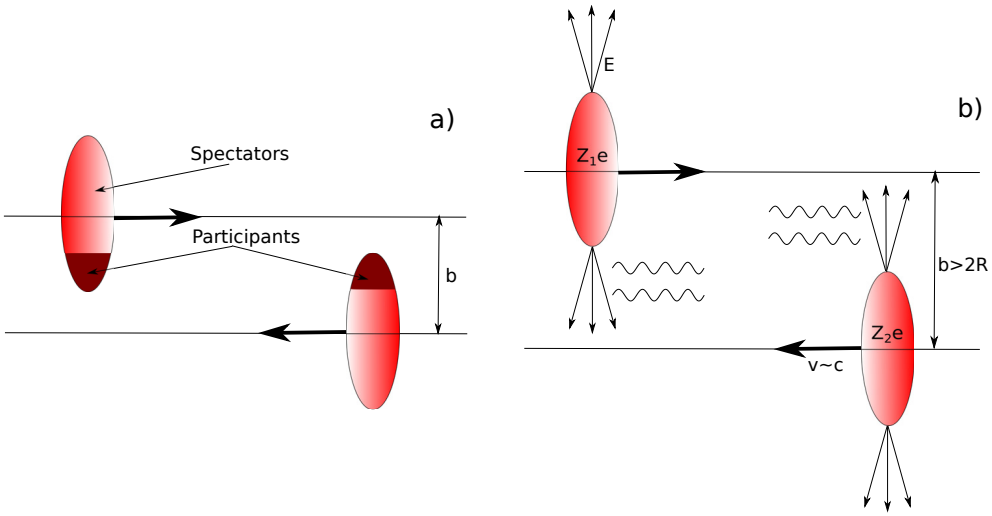

Figure 2.1: a): Schematic view of a heavy–ion collision with overlap. Spectators and participants are indicated. b): Schematic view of an ultra–peripheral heavy–ion collision.

Figure 2.1 shows two types of heavy–ion collisions. In 2.1 a) there is an overlap between the nuclei in the transverse plane, while in 2.1 b) they miss each other. The nucleons contained in the overlapping regions of the two nuclei are called the participants of the collision. The remaining nucleons are the spectators. The hadronic particle production takes place in the overlap or participant region, whereas the spectators fragment without much communication with the rest of the system.

The vector between the centres of the two nuclei in the transverse plane, is defined as the impact parameter, **b**. The smaller the impact parameter, the more central is the collision. Because most of the particles are produced in the fireball, it is relevant to characterize the collisions according to centrality. In ultra–peripheral collisions the impact parameter is larger than two times the radii of the colliding nuclei, and no hadronic interactions can occur. This is a consequence of the short range of the strong force and the short wave lengths of the nucleons at ultra–relativistic energies.

The space–time evolution of a hadronic heavy-ion collision is illustrated in Figure 2.2. When the two nuclei hit each other, their partons will start to scatter and a “fireball” is created. If the energy density is high enough, a Quark Gluon Plasma can be formed inside the fireball. As time evolves the expanding system cools down, and the the hadrons freeze out.

2.1.1 Kinematics

In classical mechanics velocities are added using Galilean transformations. When particles move with velocities close to the speed of the light, one has to use the more complicated Lorentz transformations.

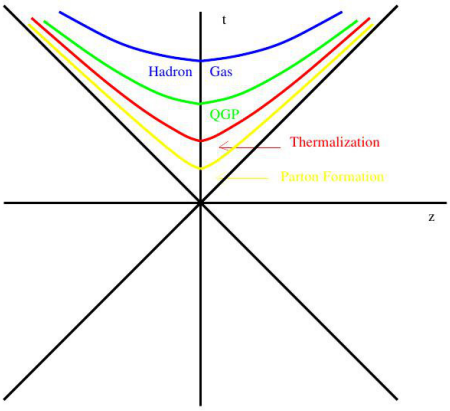

Figure 2.2: Light cone cartoon of the evolution of a heavy ion collision [4].

The Lorentz transformations from a coordinate system K to a coordinate system K', where K' is moving relative to K with velocity v along the z-axis is:

$$\begin{aligned} x &= x' \\ y &= y' \\ z &= \cosh(\tilde{y}) \cdot z' + \sinh(\tilde{y}) \cdot ct' \\ ct &= \sinh(\tilde{y}) \cdot z' + \cosh(\tilde{y}) \cdot ct' \end{aligned} \tag{2.1}$$

or using the variables β and γ:

$$\begin{aligned} x &= x' \\ y &= y' \\ z &= \gamma(z' + vt') \\ ct &= \gamma(ct' + \beta x') \end{aligned} \tag{2.2}$$

where $\beta = v/c$ and $\gamma = 1/\sqrt{1-\beta^2}$ is the Lorentz factor.

The variable $\tilde{y}$ is the rapidity of the transformation. The tilde is here to distinguish the rapidity from the coordinate y. In the following the rapidity will simply be denoted by the letter y. The rapidity is related to the velocity of the transformation, v, through

$$y = \tanh^{-1}\left(\frac{v}{c}\right) = \frac{1}{2}\ln\left(\frac{1+v/c}{1-v/c}\right), \tag{2.3}$$

The rapidity of a particle is similarly defined from the velocity of the particle. For a particle with mass m moving along the z–axis, both the total energy and momentum may be given in symmetric expressions in terms of the rapidity, y. The total energy, E, can be expressed as:

$$E = \frac{mc^2}{\sqrt{1-(\frac{v}{c})^2}} = mc^2\cosh(y), \tag{2.4}$$

and similar for the momentum, p:

$$pc = \sqrt{E^2 - m^2c^4} = \sqrt{m^2c^4\cosh^2(y) - m^2c^4} = mc^2\sinh(y) \tag{2.5}$$

When a scattering occurs or when a particle is produced, the scattered particles have a different direction form the original direction of the projectile. One then introduces the transverse mass, m_T:

$$m_T^2c^4 = p_T^2c^2 + m^2c^4, \tag{2.6}$$

where p_T is the component of the momentum in a direction perpendicular to the original direction. The total energy is given in terms of m_T and y by:

$$E = m_Tc^2\cosh(y) \tag{2.7}$$

Similarly, for the longitudinal momentum one can derive:

$$p_Lc = m_Tc^2\sinh(y). \tag{2.8}$$

From these definitions of E and p_L one can derive another definition for the rapidity, y:

$$y = \frac{1}{2}\ln\left(\frac{E + p_Lc}{E - p_Lc}\right) = \frac{1}{2}\ln\left(\frac{1 + v_L/c}{1 - v_L/c}\right) \tag{2.9}$$

As one can see, when v_L goes towards 0, the rapidity also goes to zero. This means that the rapidity is 0 for a particle going perpendicular to the projectile direction, and is goes towards infinity for a particle moving at the speed of light in the longitudinal direction.

At high energies the rapidity, y, can be approximated by the pseudorapidity, η. If one starts with the rapidity

$$y = \frac{1}{2}\ln\frac{E + p_zc}{E - p_zc} = \frac{1}{2}\ln\left(\frac{\sqrt{p^2c^2 + m^2c^4} + p_zc}{\sqrt{p^2c^2 + m^2c^4} - p_zc}\right). \tag{2.10}$$

At relativistic energies $pc \gg mc^2$, and one can approximate the rapidity with the pseudorapidity, which is consequently defined as:

$$\eta = \frac{1}{2}\ln\left(\frac{p + p_z}{p - p_z}\right) \tag{2.11}$$

If the scattering angle θ is introduced, η may be written

$$\eta = \frac{1}{2}\ln\left(\frac{p + p\cos(\theta)}{p - p\cos(\theta)}\right) = -\ln\left(\tan\left(\frac{\theta}{2}\right)\right) \tag{2.12}$$

A 4–vector is a four dimensional vector which transforms like the vector (ct, x, y, z) in Equation 2.1 under a Lorentz transformation. For a particle with energy E and momentum $\mathbf{p} = (p_x, p_y, p_z)$, the vector (E, p_x, p_y, p_z) is a 4–vector. The components of the vector is related by $E^2 = m^2c^4 + p_x^2c^2 + p_y^2c^2 + p_z^2c^2$. If the mass is known, there are therefore three independent components. In ultra-relativistic nuclear collisions it is sometimes convenient to use the variables y, m_T and ϕ instead of p_x, p_y and p_z. Here

y and m_T is the rapidity and transverse mass as defined above, and ϕ is the azimuthal angle.

In a scattering process $1+2 \to 3+4$ it is convenient to introduce the so called Mandelstam variables

$$\begin{aligned} s &= -c^2(\mathbf{p}_1+\mathbf{p}_2)^2 + (E_1+E_2)^2 \\ t &= -c^2(\mathbf{p}_1-\mathbf{p}_3)^2 + (E_1-E_3)^2 \\ u &= -c^2(\mathbf{p}_1-\mathbf{p}_4)^2 + (E_1-E_4)^2 \end{aligned} \tag{2.13}$$

These are all Lorentz invariant. In the center–of–mass system $\mathbf{p_1}+\mathbf{p_2}=0$ by definition, and s becomes

$$s = (E_1+E_2)^2 \tag{2.14}$$

The variable s is thus the square of the total energy in the center–of–mass system, and it can be defined in any type of collision between two particles. If s and t are known, u is given by the relation $s+t+u = m_1^2+m_2^2+m_3^2+m_4^2$.

For the reaction $\gamma + A \to V + A$ (exclusive photonuclear vector meson production) for example, which is one of the main reactions studied in this thesis, the Mandelstam variable t corresponds to the momentum transfer from the nucleus squared. Approximately, t will be given by the transverse momentum of the vector meson, $t = -p_T^2$.

For a coherent and exclusive interaction, t will be restricted by the form factor of the nucleus.When an electron scatters off a target with an extended structure one has to take the spatial distribution of the target particle into account. The cross section for such scattering is

$$\frac{\mathrm{d}\sigma}{\mathrm{d}\Omega} = \frac{\mathrm{d}\sigma}{\mathrm{d}\Omega_{Mott}} |F(\mathbf{q}^2)|^2, \tag{2.15}$$

where $\frac{\mathrm{d}\sigma}{\mathrm{d}\Omega_{Mott}}$ is the Mott cross section for scattering of a point charge, the multiplicative factor $F(\mathbf{q}^2)$ is the form factor, and $\mathbf{q}^2 = (\mathbf{p}_1-\mathbf{p}_2)^2$ is the momentum transfer squared. For a target of charge Q the charge density can be written as $R\rho(\mathbf{r})$, where $\rho(\mathbf{r})$ is the normalized probability density, $\int \rho(\mathbf{r})\,\mathrm{d}^3r = 1$. The form factor can be written as the Fourier transform of the probability density:

$$F(\mathbf{q}^2) = \int \rho(\mathbf{r}) \cdot e^{i\mathbf{q}\cdot\mathbf{r}/\hbar}. \tag{2.16}$$

2.2 The Quantum Field Theories QED and QCD

2.2.1 Quantum electrodynamics (QED)

The content in this and the next subsections is mostly taken from Reference [5]. In nonrelativistic quantum mechanics particles are described by the *Schrödinger equation*:

$$-\frac{\hbar^2}{2m}\nabla^2\Psi + V\Psi = i\hbar\frac{\partial\Psi}{\partial t} \tag{2.17}$$

In relativistic quantum mechanics particles of spin $\frac{1}{2}$ are described by the *Dirac equation*

$$(i\hbar\gamma^\mu\partial_\mu - mc)\Psi = 0 \tag{2.18}$$

Here μ is an index from 0 to 3 and

$$\partial_\mu = \frac{\partial}{\partial x^\mu} \tag{2.19}$$

and γ^μ is a set of four dimensional matrices, and Ψ is a four element matrix, called the Dirac spinor:

$$\Psi = \begin{pmatrix} \Psi_1 \\ \Psi_2 \\ \Psi_3 \\ \Psi_4 \end{pmatrix} \tag{2.20}$$

In classical electrodynamics the electric and magnetic fields set up by a charge density ρ and a current density $\mathbf{J}$ are described by the Maxwell equations:

$$\begin{array}{ll} \text{(i) } \nabla\cdot\mathbf{E} = 4\pi\rho & \text{(iii) } \nabla\cdot\mathbf{B} = 0 \\ \text{(ii) } \nabla\times\mathbf{E} + \frac{1}{c}\frac{\partial\mathbf{B}}{\partial t} = 0 & \text{(iv) } \nabla\times\mathbf{B} - \frac{1}{C}\frac{\partial\mathbf{E}}{\partial t} = \frac{4\pi}{c}\mathbf{J} \end{array} \tag{2.21}$$

By introducing a four dimensional vector potential, A^μ, and current J^ν

$$A^\mu = (V, \mathbf{A}), \;\; J^\nu = (\rho, \mathbf{J}) \tag{2.22}$$

these can be written

$$\partial_\mu \partial^\mu A^\nu - \partial^\nu(\partial_\mu A^\mu) = \frac{4\pi}{c} J^\nu \tag{2.23}$$

The fields $\mathbf{E}$ and $\mathbf{B}$ can be obtained from

$$\mathbf{B} = \nabla\times\mathbf{A} \tag{2.24}$$

and

$$\mathbf{E} = -\nabla V - \frac{1}{c}\frac{\partial\mathbf{A}}{\partial t} \tag{2.25}$$

The potential formulation has the defect that V and $\mathbf{A}$ are not uniquely determined. Any new potentials, such as

$$A'_\mu = A_\mu + \partial_\mu\lambda \tag{2.26}$$

would work just as well, since $\partial^\mu A^{\nu'} - \partial^\nu A^{\mu'} = \partial^\mu A^\nu - \partial^\nu A^\mu$. Such changes of the potential is called gauge transformations, and have no effect on the fields. The gauge freedom can be used to impose an extra constraint on the potential, called the Lorentz condition:

$$\partial_\mu A^\mu = 0 \tag{2.27}$$

With this, Maxwell's equations simplifies to:

$$\Box A^\mu = \frac{4\pi}{c} J^\mu \tag{2.28}$$

where $\Box = \frac{1}{c^2}\frac{\partial^2}{\partial t^2} - \nabla^2$ is called the d'Alembertian operator.

Even the Lorentz condition does not uniquely specify A^μ. Further gauge transformations are possible provided that the gauge function λ satisfy the wave equation

$$\Box\lambda = 0 \tag{2.29}$$

which is called the Coulomb gauge. Free photons correspond to solutions of Equation 2.28 in empty space i.e. with $J^\nu = 0$.

$$\Box A^\mu = 0 \tag{2.30}$$

A plane–wave solution with $p = (E/c, \mathbf{p})$ is found:

$$A^\mu(x) = a e^{-(i/\hbar)p\cdot x}\epsilon^\mu(p) \tag{2.31}$$

where ϵ^μ is the polarization vector, which characterizes the spin of the photon, and a is a normalization factor. Putting Equation 2.31 into Equation 2.30 one obtains a constraint on p^μ:

$$p^\mu p_\mu = 0 \tag{2.32}$$

such that

$$E = |\mathbf{p}|c \tag{2.33}$$

as it should be for a massless particle.

ϵ^μ has four components, but they are not all independent. The Lorentz condition requires that

$$p^\mu \epsilon_\mu = 0. \tag{2.34}$$

In the Coulomb gauge we have

$$\epsilon^0 = 0, \quad \epsilon \cdot \mathbf{p} = 0 \tag{2.35}$$

which means that the polarization three–vector (ϵ) is perpendicular to the direction of propagation. This means that the photon is transversely polarized. Now, there are two linearly independent three–vectors that are perpendicular to $\mathbf{p}$. If $\mathbf{p}$ points in the z–direction we have:

$$\epsilon_{(\mathbf{1})} = (1,0,0), \quad \epsilon_{\mathbf{2}} = (0,1,0) \tag{2.36}$$

Thus instead of four independent solution for a given momentum, only two are left, which is the correct number of spin states for a massless particle of spin 1.

Quantum electrodynamics (QED) describes the interactions between charged fermions (quarks and leptons) and photons. Formally, the theory is described by a Lagrangian. From this one can derive a set of rules (the Feynman rules) which describe how results can be obtained through perturbation theory using single particle wave functions. For example the amplitude or matrix element of the scattering of an electron in an initial state Ψ_i to a final state Ψ_f in the presence of an extended electromagnetic field can be written $\mathscr{M}_{fi} = ie \int \Psi_f \gamma_\mu A^\mu \Psi_i \, \mathrm{d}^4x$.

To calculate the decay rate or scattering cross section of a process one needs in addition to the amplitude $\mathscr{M}$ the phase space available. The amplitude contains the dynamical information, while the phase space contains the kinematic information.

The transition rate for a given process is determined by the amplitude and the phase space according to Fermi's golden rule:

$$\sigma \propto |\mathscr{M}|^2 \times (\text{phase space}) \tag{2.37}$$

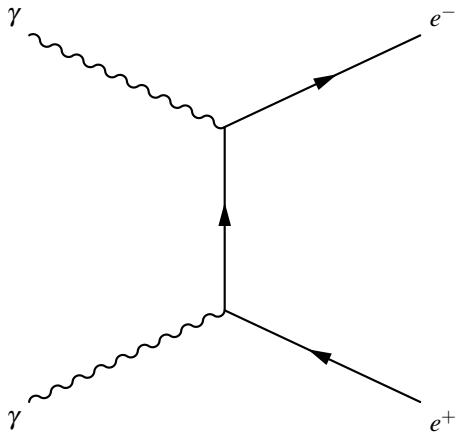

Figure 2.3: Feynman diagram of the process $\gamma\gamma \to e^+e^-$. Time is here from left to right.

To each amplitude there is an associated Feynman diagram. Figure 2.3 shows a Feynman diagram of the process $\gamma\gamma \to e^+e^-$. The cross section for this can be calculated, and the result is known as the Breit–Wheeler cross section of the reaction $\gamma\gamma \to e^+e^-$ [6]:

$$\sigma_{\gamma\gamma\to e^+e^-}(W) = \frac{4\pi\alpha^2}{W^2}\left[\left(2+\frac{8M^2}{W^2}-\frac{16M^4}{W^4}\right)\ln\frac{W+\sqrt{W^2-4M^2}}{2M}-\sqrt{1-\frac{4M^2}{W^2}}\left(1+\frac{4M^2}{W^2}\right)\right] \quad (2.38)$$

where M is the lepton mass, and W the e^+e^- or $\gamma\gamma$ center of mass energy. Two–photon production of e^+e^-–pairs in Pb–Pb collisions at the LHC is one topic that will be discussed in this thesis. The strength of the interaction between a charged particle and the photon is characterized by the coupling constant

$$\alpha = \frac{e^2}{4\pi\varepsilon_0\hbar c} \approx \frac{1}{137} \quad (2.39)$$

usually called the fine structure constant. Here, ε_0 is the permittivity of free space, and e the elementary charge. Since α is small compared to 1, higher order terms are less important, and this makes the application of perturbation theory successful. Contributions from higher order terms, where additional photons are exchanged, contain higher powers of α. Since α is small it is often a reasonable approximation to neglect these in QED as long as singly charged particles are involved.

2.2.2 Quantum chromodynamics (QCD)

The strong interaction between quarks and gluons is described by Quantum chromodynamics (QCD)) which is a quantum field theory in many aspects similar to QED. The gauge field quantum of QCD, the gluon, is like its counterpart, the photon, massless and has a spin of 1. The gluons themselves are "colour–charged" and not neutral as the photon. There are three different colours; red, green and blue, and three anticolours; antired, antigreen and antiblue. The gluons can be considered bicoloured, made up of

a colour and an anticolour. Out of three colours and their anticolours we can make up nine possible combinations. One of these, $r\bar{r}+g\bar{g}+b\bar{b}$, is colour symmetric and the eight other correspond to the gluons. Since the gluons themselves are colour–charged, they can interact with each other and not only with quarks.

No coloured objects, made up of quarks or gluons, can exist freely, but must be combined and confined into colourless hadrons. Only particles corresponding to colourless quark combinations, such as $q\bar{q}$ or qqq are observed. Coloured combinations, such as qq or $qq\bar{q}$, have never been seen. The forces are thus strongly attractive for colourless states and repulsive for other ones. If one tries to separate a quark and an antiquark, the energy required to do so increases linearly with the separation, and it takes infinite energy to "liberate" the particles. Once the energy contained in the field is large enough to create a new $q\bar{q}$–pair from the vacuum, the original $q\bar{q}$–pair splits up into two pairs with no strong field between them. Therefore the quarks are confined in hadrons. QCD has the property that the force becomes weak at short distances. This "asymptotic freedom" of the theory can be tested at high energies and momentum transfers. The QCD analogue of the fine structure constant, α_s, proportional to the square of the coupling constant, $\alpha_s = g_s^2/\hbar c$, varies with momentum transfer:

$$\alpha_s(q^2) = \frac{\alpha_s(\mu^2c^2)}{1+\frac{\alpha_s(\mu^2c^2)}{12\pi}(33-2n_f)\ln(\frac{q^2}{\mu^2c^2})} \tag{2.40}$$

Here μ is a mass that sets the scale, q is the four–momentum transfer and n_f is the number of flavours (six). At a scale equal to the mass of the Z–particle, $\alpha_s(M_Zc^2) = 0.118$ [7]. The fine structure constant of electrodynamics also changes with momentum transfer, but much more slowly and in opposite direction. It becomes larger at higher momentum transfers.

A quark is described in QCD by a four–dimensional Dirac spinor (Equation 2.20) multiplied by a three–dimensional vector representing the colour state (the three dimension corresponding to the three colours red, green and blue). The gluon, being a massless spin–1 object, is described by a wave function similar to Equation 2.31 multiplied by a eight–dimensional vector representing the possible colour states. When performing perturbative calculations one has to sum and average over the possible colour combinations in the initial and final states. Otherwise the calculations are done in the same way as in QED.

An example of a Feynman diagram for quark–antiquark production is shown in Figure 2.4. The cross section for this process is [8]

$$\sigma_{\gamma g\to q\bar{q}}(W) = \frac{1}{2}\cdot e_q^2\cdot\frac{4\pi\alpha\alpha_s(Q^2)}{W^2}\left[\left(2+\frac{8M^2}{W^2}-\frac{16M^4}{W^4}\right)\ln\frac{W+\sqrt{W^2-4M^2}}{2M} -\sqrt{1-\frac{4M^2}{W^2}}\left(1+\frac{4M^2}{W^2}\right)\right] \tag{2.41}$$

It differs from Equation 2.38 by the inclusion of e_q, corresponding to the fractional charge of the quark ($\frac{1}{3}$ or $\frac{2}{3}$), and a replacement of α to α_s for the quark–gluon vertex The "$\frac{1}{2}$" is the so called colour factor, which results from the summing and averaging over the colour states. M is the quark mass.

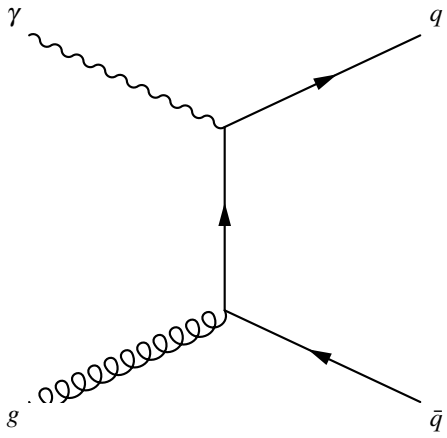

Figure 2.4: Feynman diagram of the process $\gamma g \to q\bar{q}$. Time is here from left to right.

In a nucleon with high energy the momenta of the partons are almost collinear with the momentum of the nucleon, such that the nucleon can be seen as a stream of partons, each carrying a fraction x of the total momentum. How the partons are distributed inside the nucleons is described by the Parton Distribution Functions (PDFs) They are probability density functions describing the probability to find a parton carrying the momentum fraction x at the squared energy scale μ. The PDFs of nucleons are usually measured through Deep Inelastic Scattering (DIS), where a lepton scatters off a nucleon, interacting with a parton through photon exchange. The PDFs can not be determined from pQCD itself, but have to be determined from data at some scale μ.

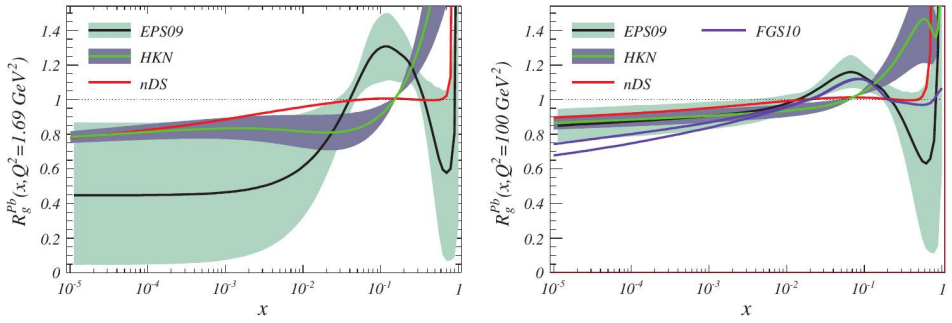

Figure 2.5: Different parametrizations of R_g^{Pb} with $Q^2 = 1.69$ GeV^2 (left) and $Q^2 = 100$ GeV^2 (right) [9].

The PDF of a nucleus is different than the superposition of the constituent nucleon PDFs. The nuclear modifications are described by the nuclear ratio, $R_i^A(x,Q^2)$. For the Nuclear Parton Distribution Function (nPDF) $F^A(x,Q^2)$ and the nucleon PDF $F^{nucleon}(x,Q^2)$ the nuclear ratio becomes [10]:

$$R_F^A(x,Q^2) = \frac{1}{A}\frac{F^A(x,Q^2)}{F^{nucleon}(x,Q^2)} \tag{2.42}$$

Here A is the number of nucleons in the nucleus. x and Q^2 are defined as in DIS. Figure 2.5 shows parametrizations of the nuclear factor for gluons in lead nuclei, R_g^{Pb} for two different scales. The parametrizations can be divided in four regions, from left to right [10]: The shadowing region, where $R_g^{Pb} < 1$ and $x \lesssim 3 \cdot 10^{-2}$; the antishadowing region, where $R_g^{Pb} > 1$ and $3 \cdot 10^{-}2 \lesssim x \lesssim 3 \cdot 10^{-1}$; the EMC (European Muon Collaboration) region where $R_g^{Pb} < 1$ and $0.3 \lesssim x \lesssim 0.8$; and the Fermi motion region where $R_g^{Pb} > 1$ and $x > 0.8$.

2.2.3 Non–pertubative QCD

At extreme temperature and/or density the colour–charges of the quarks and gluons will, according to QCD, be screened. The strong force will therefore decrease, and under these circumstances the constituent quarks and gluons may be freed from the nucleons in which they are normally confined. This is a new state of matter, called the Quark Gluon Plasma (QGP). This phase transition happens at a critical temperature of $T \approx 160$ MeV and critical energy density of $\epsilon_c \sim 0.5$ GeV/fm^3 [11].

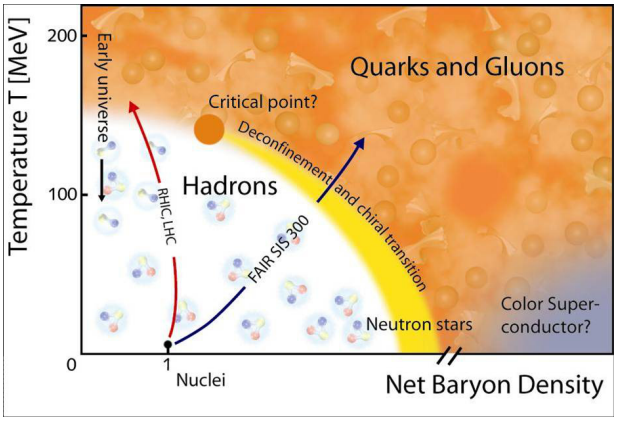

Figure 2.6: QCD phase diagram [12].

A phase diagram of hadronic matter is shown on Figure 2.6 with net baryon density and temperature on the x– and y–axis. In a heavy–ion collision the nuclei are initially of normal density ($\rho \approx 0.17$ fm^{-3}) and temperature ($T \approx 0$). During the collision, the matter is compressed and heated. If the energy is high enough the system may pass the phase boundary and exist for a short while in the form of a quark gluon plasma. As the density and temperature drops, hadrons will be formed as the system freezes out. During a collision, the system will thus follow a certain path in the phase diagram as indicated by the arrows in Figure 2.6.

For the early universe the temperature was extremely high and the net baryon density relatively low. As the temperature dropped to about $T \approx 160$ MeV, the state changed from a QGP to hadronic matter. According to lattice QCD calculations, there will probably be a smooth crossover from QGP to hadronic matter at such baryon densities. If the baryon density is higher the QGP will probably undergo a sharp first–order

transition to hadronic matter.

The cosmological model describing the early development of the universe is called The Big Bang Theory. According to the theory the universe, around 13.7 billion years ago, was in an extremely hot and dense state. Around 1 – 10 μs after Big Bang one believes that the quarks and gluons were deconfined. As the universe expanded and cooled down the quarks was confined in mesons and baryons held together by the strong force. A small excess of quarks to anti–quarks led to an excess in baryons to anti–baryons. A the same time the temperature was no longer high enough to create nucleon–antinucleon pairs, so a mass annihilation followed, which left only 1 out of 10^{10} of the nucleons behind, and none of the antinucleons.

2.3 Important results from central heavy ion collisions

One goal of relativistic heavy–ion collisions is to recreate the Quark Gluon Plasma in the laboratory and thus learn more about the evolution of the early universe. In this context it is of course important to have a good understanding of the nuclear PDFs to be able to disentangle effects produced by the plasma from modifications of the initial state.

To study the properties of the created state of matter, two of the important variables to measure are the anisotropic flow, and the suppression of high–p_T charged particles. Anisotropic flow is an important observable in ultra–relativistic heavy–ion collisions as it signals the presence of multiple interactions between the constituents of the created matter. In non–central heavy–ion collisions the participants form an almond shape, see Figure 2.7 left. This means that the pressure gradient inside the overlap region is larger in the reaction plane than out of plane. The anisotropy in azimuthal angle can be written a a Fourier series:

$$E\frac{\mathrm{d}^3N}{\mathrm{d}^3p} = \frac{1}{2\pi}\frac{\mathrm{d}^2N}{p_T\mathrm{d}p_T\mathrm{d}y}\left(1+\sum_{n=1}^{\infty}2v_n\cos(n(\phi-\Psi_R)\right) \tag{2.43}$$

The azimuthal anisotropic flow is then characterized by the Fourier coefficients [13]:

$$v_n = \langle\cos[n(\phi-\Psi_n)]\rangle, \tag{2.44}$$

where ϕ is the azimuthal angle of the particle, Ψ_n is the azimuthal angle of the initial state spatial plane of symmetry and n is the order of the harmonic. The first harmonic (v_1) is called directed flow, the second harmonic (v_2) elliptic flow and the third harmonic (v_3) triangular flow, etc.

The elliptic flow of charged particles in Pb–Pb collisions at $\sqrt{s_{NN}} = 2.76$ TeV, has been measured by ALICE [14]. The right panel of Figure 2.7 shows the integrated elliptic flow in the 20–30% centrality class, compared to results from lower energies at similar centralities. The integrated elliptic flow is found to increase about 30% from the measurements with Au–Au at $\sqrt{s} = 200$ GeV at RHIC.

One of the signals from a created QGP is the suppression of high–p_T charged hadrons produced in Pb–Pb collisions as compared to pp collisions. The dominant production mechanism for high–p_T hadrons is the fragmentation of high–p_T partons that

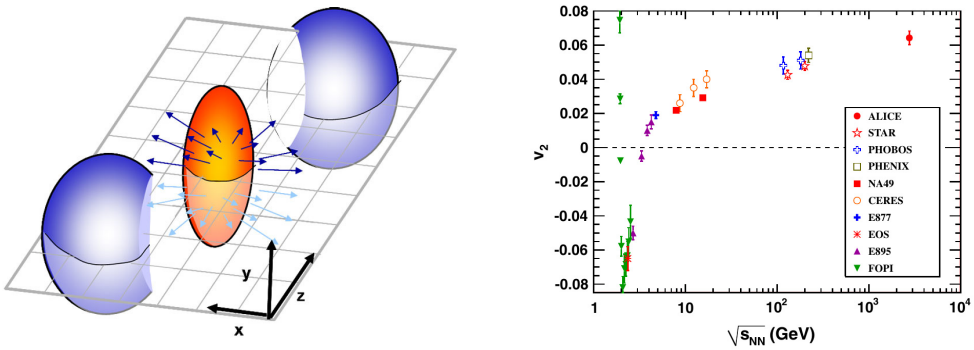

Figure 2.7: Left: Cartoon of elliptic flow in a heavy–ion collision. Right: Integrated elliptic flow at 2.76 TeV in Pb–Pb collisions, 20% to 30% centrality class, measured by ALICE, compared with results from lower energies at similar centralities [14].

come from hard scatterings int the early stages of the collision. The partons lose energy as they transverse the hot and dense QCD medium, and this leads to the suppression.

The nuclear modification factor, R_{AA}, is used to quantify the nuclear medium effects at high p_T. R_{AA} is defined as the ratio of the charged particle yield in Pb–Pb collisions to that in pp collisions, scaled by the number of binary nucleon–nucleon collisions, $\langle N_{coll} \rangle$:

$$R_{AA}(p_T) = \frac{(1/N_{evt}^{AA})\mathrm{d}^2N_{ch}^{AA}/\mathrm{d}\eta\mathrm{d}p_T}{\langle N_{coll}\rangle(1/N_{evt}^{pp}\mathrm{d}^2N_{ch}^{pp}/\mathrm{d}\eta\mathrm{d}p_T}, \tag{2.45}$$

ALICE has measured the R_{AA} in Pb–Pb collisions at center–of–mass energy $\sqrt{s_{NN}}$ = 2.76 TeV (Figure 2.8 left) [15]. As one can see, the suppression is significant in central collisions, but almost absent in peripheral collisions. The interpretation of this is that the partons have to travel a larger distance, and the density of free colour charges is higher in central than in peripheral collisions. In the right panel of Figure 2.8 R_{AA} in central collisions up to $p_T = 50$ GeV/c compared to model calculations is shown.

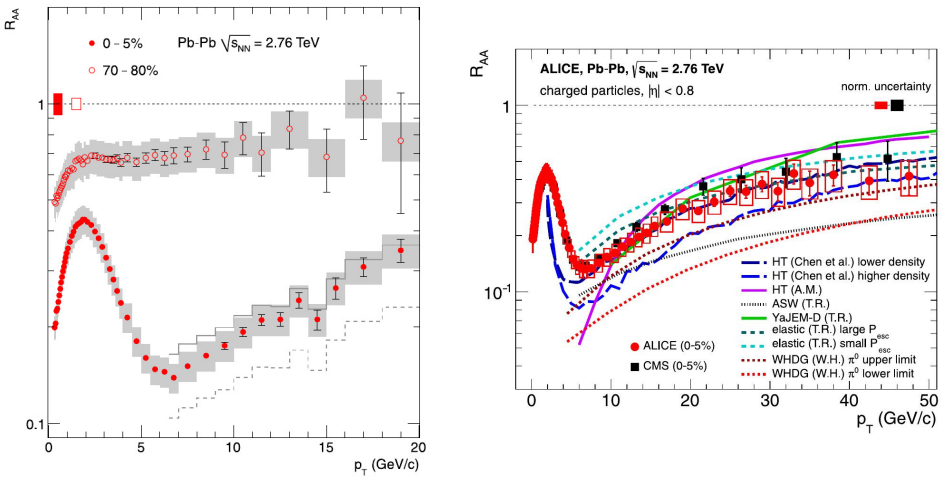

Figure 2.8: Left: R_{AA} in central (0–5%) and peripheral (70–80%) Pb–Pb collisions at $\sqrt{s_{NN}}$ = 2.76 TeV measured by ALICE [15]. Right: R_{AA} in central collisions compared to results from CMS and model calculations [16].

Chapter 3

The Physics of Ultra-peripheral Collisions

3.1 Introduction

In 1924 Enrico Fermi introduced a method which treated electromagnetic fields of moving charged particles as a flux of virtual photons, known as the equivalent photon method [17]. A decade later this method was extended to also include ultra–relativistic particles, by Weiszäcker [18] and Williams [19]. The method is often referred to as the Weiszäcker–Williams method. The electric field of a fast–moving charged particle, will point radially outward, while the magnetic field is circling it. At a point some distance away from the trajectory of the particle, the field will resemble that of a real photon. Fermi therefore replaced the electromagnetic fields from a fast particle with an equivalent flux of photons. The number of photons with energy ω, $n(\omega)$, is given by the Fourier transform of the time–dependent electromagnetic field [20].

In an ultra–peripheral collision between two charged particles at large impact parameters (Figure 3.1), these photons may induce interactions. Ultra-peripheral collisions can be divided into photon–photon interactions and photonuclear interactions. In the first case the radiated photons interact with each other, while in the second case one radiated photon interacts with the other nucleus. The nucleus that emits the photon will in most cases remain intact after the collision, while the target nucleus may break up. Breakup can also occur through the exchange of additional photons. The three processes are illustrated in Figure 3.2.

3.2 The photon flux

The photon energy spectrum depends on the minimum distance between the target and the moving charge, and on the projectile velocity, or in other words, the time a target particle is exposed to the field. To determine the exact from of the photon spectrum one has to do a Fourier transform of the fields. For this, one needs a relativistically correct expression of how the fields from a moving charged particle appear to an observer at rest. Such an expression can be obtained from the Lorentz transformation of the 4–vector potential A^{μ}, which transforms as a 4–vector (cf. Section 2.2.1). The relativistic effects lead to an increase in the **E**–field by the Lorentz factor γ of the beam ($\gamma = 1/\sqrt{(1-\frac{v^2}{c^2})}$) compared with the non–relativistic case. The field is furthermore contracted in the longitudinal direction by the same factor. The shape of the field re-

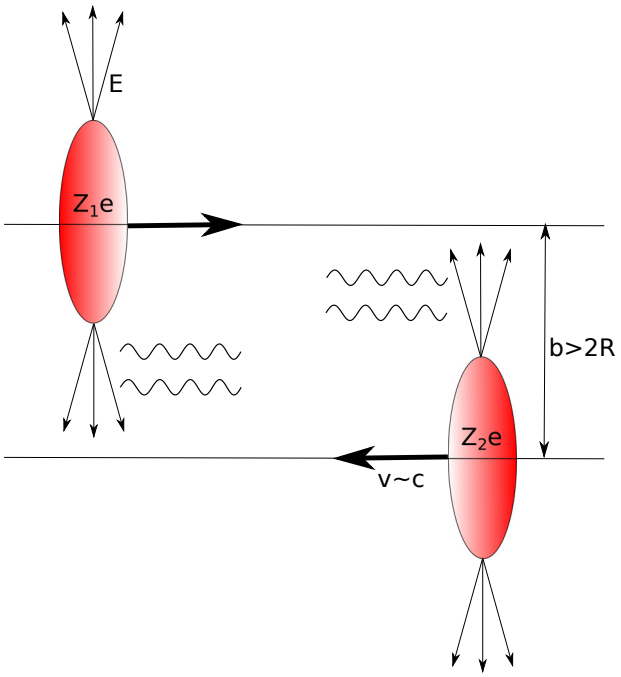

Figure 3.1: The fields of photons surrounding the moving charged particles.

sembles a pancake moving along with the particle (cf. Figure 3.1). The moving charge also induce a magnetic field perpendicular to the **E**–field and with the same strength (in units where $c = 1$). The minimum photon wavelength is the width of the pancake at the target.

The maximum photon energy will thus be of the order of

$$\omega^{max} \sim \frac{\hbar}{\Delta t} = \frac{\gamma\hbar v}{b}, \tag{3.1}$$

In a collision where the two nuclei barley touch each other, the impact parameter is $b_{min} = 2R_A$. The maximum photon energy will then be $\gamma\hbar v/2R_A$, or about a fraction $\hbar/(2R_A A m_p c)$ of the ion energy. Here Am_p is the mass of the ion. For heavy ions, with $R_A \sim 7$ fm, the maximum photon energy is about $0.03/A$ of the ion energy [22]. For protons, assuming a proton radius of 0,7 fm, the maximum photon energy is about 3% of the energy of the proton.

In photon-gold collisions at RHIC ($\sqrt{s_{NN}} = 200$ GeV) one can reach γ–nucleon center–of–mass energies up to 30 GeV per nucleon. In photon–lead collisions at LHC at design energy, the γ–nucleon center–of–mass energy can reach 1 TeV.This is more than an order of magnitude higher than what can be reach anywhere else.

The photon spectrum obtained from the Fourier transform is:

$$n(\omega, b) = \frac{\mathrm{d}N^2}{\mathrm{d}\omega \mathrm{d}b} = \frac{Z^2\alpha}{\pi^2}\frac{1}{\beta^2}\frac{1}{\omega b^2}x^2\left(K_1^2(x) + \frac{1}{\gamma^2}K_0^2(x)\right) \tag{3.2}$$

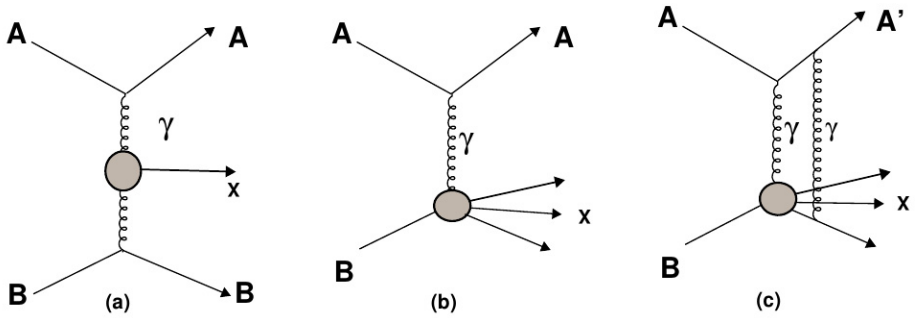

Figure 3.2: A schematic view of (a) an electromagnetic interaction where photons emitted by the ions interact with each other, (b) a photonuclear reaction in which a photon emitted by an ion interacts with the other nucleus, (c) photonuclear reaction with nuclear breakup due to photon exchange. [21]

where $x = b\omega/\beta\gamma$, ω is the photon energy, and $K_0(x)$ and $K_1(x)$ are modified Bessel functions[20]. Here, natural units are used ($\hbar = c = 1$).

The first term, $K_1^2(x)$, gives the flux of photons transversely polarized to the ion direction, and the second term, $K_0^2(x)$ is the flux for longitudinally polarized photons. For ultra–relativistic particles the transverse polarization is dominant.

If the two colliding ions overlap, the hadronic interactions will be totally dominant over the photonuclear interactions. The "useful" photon flux is therefore that for when the ions do not overlap, or the impact parameter, b, is greater than twice the nuclear radius. If one treats the nuclei as hard spheres, one can take $R_A = 1.2A^{1/3}$ fm, where A is the atomic mass number.

The photons can interact with a target nucleus in a one–photon process or with its electromagnetic field in a two–photon process. In photonuclear (one–photon) interaction, the usable photon flux is obtained by integrating Equation 3.2 over $b > b_{min} = 2R_A$ [20]:

$$n(\omega) = \int_{b>2R_A} N(\omega, b)\mathrm{d}^2 b = \frac{2Z^2\alpha}{\pi}\frac{1}{E_\gamma}\left(xK_0(x)K_1(x) - \frac{1}{2}x^2\left(K_1^2(x) - K_0^2(x)\right)\right) \quad (3.3)$$

where $x = 2RE_\gamma/\beta\gamma$. The formulation above, which is based on a Fourier transform of the time dependence of the fields, provide only the photon energy and longitudinal momentum distribution. The virtuality of the photon, and thus its transverse momentum, is determined by the nuclear form factor. This means that $-q^2 < (\hbar/R_A)^2$, which make them almost real.

3.3 Two-photon processes

Two–photon process have been studied at e^+e^- colliders for a long time. They are an excellent tool for many aspects of meson spectroscopy and tests of QED. As an

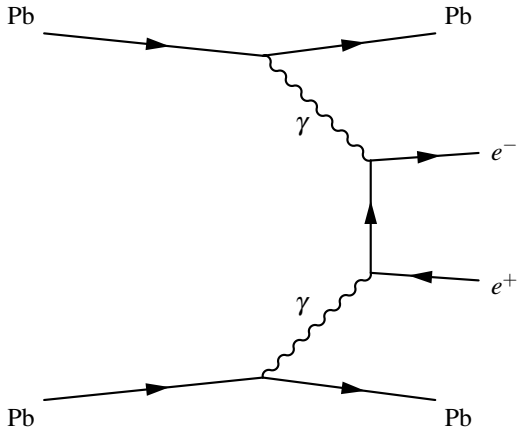

Figure 3.3: Diagram of exclusive production of an e^+e^- pair in a Pb–Pb collision.

example of the use of the method of equivalent photons on two–photon interactions the process $Pb+Pb \rightarrow Pb+Pb\ +\ e^+e^-$ will be discussed.

A Feynman diagram for this reaction is shown in Figure 3.3. This diagram has four vertices and three internal lines, and is too complicated to solve analytically. To calculate the cross section for this process one in practice separates out the subprocess $\gamma\gamma \rightarrow e^+e^-$, for which the cross section was given in Chapter 2. and use the photon flux to determine the total cross section. This can be written:

$$\sigma_X = \int \frac{n(\omega_1)}{\omega_1}\frac{n(\omega_2)}{\omega_2}\sigma_X^{\gamma\gamma}(\omega_1,\omega_2)\,\mathrm{d}\omega_1\mathrm{d}\omega_2, \tag{3.4}$$

where $\sigma_X^{\gamma\gamma}$ is the two–photon cross section.

The photon densities (Equation 3.2) can be integrated over impact parameter to obtain the equivalent differential photon flux (Equation 3.3). Since hadronic interactions will dominate when the nuclear impact parameter is smaller than the sum of the nuclear radii, this region must be excluded [23, 24]. A Θ–function is used to eliminate the contribution from this nuclear overlap, when the photon densities are integrated over impact parameter. The differential two–photon flux is then:

$$\frac{\mathrm{d}^2N_{\gamma\gamma}}{\mathrm{d}\omega_1\mathrm{d}\omega_2} = \int_{b_1>R}\int_{b_2>R} n(\omega_1,b_1)n(\omega_2,b_2)\Theta(|\mathbf{b_1}-\mathbf{b_2}|-2R)\mathrm{d}^2b_1\mathrm{d}^2b_2 \tag{3.5}$$

The Θ–function is Equation 3.5 treats the nuclei as hard spheres. A more realistic model is to also include the diffuseness of the nuclear surface. One can rewrite Equation 3.5 as [25]:

$$\frac{\mathrm{d}^2N_{\gamma\gamma}}{\mathrm{d}\omega_1\mathrm{d}\omega_2} = \int_{b_1>R}\int_{b_2>R} n(\omega_1,b_1)n(\omega_2,b_2)[1-P_{int}(|\mathbf{b}_1-\mathbf{b_2}|)]\mathrm{d}^2b_1\mathrm{d}^2b_2 \tag{3.6}$$

where $P_{int}(b)$ is the hadronic interaction probability for a nuclear collision at impact parameter b. Hadronic interaction are also possible at impact parameters larger than $2R$. The probability for such an interaction can be calculated using the Glauber model [25]:

$$P(b) = 1-\exp\left(-\sigma_{nn}\int T_A(r)T_B(b-r)\mathrm{d}^2r\right) \tag{3.7}$$

where σ_{nn} is the hadronic nucleon–nucleon cross section, and $T(r)$ is the nuclear thickness function, which is calculated using the nuclear density function ρ [25]:

$$T(\mathbf{b}) = \int \rho(\mathbf{b}, z)\mathrm{d}z \tag{3.8}$$

To calculate ρ a Wood–Saxon distribution is used:

$$\rho(r) = \frac{\rho_0}{1+\exp\left(\frac{r-R_{nuc}}{c}\right)} \tag{3.9}$$

where R_{nuc} is the nuclear radius and c is the skin–thickness.

The individual photon energies ω_1 and ω_2 can be converted to the $\gamma\gamma$ center–of–mass energy W, and the rapidity, Y:

$$\begin{array}{ll} \omega_1 = \frac{1}{2}We^{Y} & W = \sqrt{4\omega_1\omega_2} \\ \omega_2 = \frac{1}{2}W^{-Y} & Y = \frac{1}{2}\ln(\omega_1/\omega_2) \end{array} \tag{3.10}$$

Equation 3.5 now translates to:

$$\frac{\mathrm{d}^2N_{\gamma\gamma}}{\mathrm{d}W\mathrm{d}Y} = \frac{W}{2}\frac{\mathrm{d}^2N_{\gamma\gamma}}{\mathrm{d}\omega_1\mathrm{d}\omega_2} \tag{3.11}$$

The cross section for lepton pairs is given by the Breit–Wheeler formula (2.38). The cross section for the reaction $A+A \to A+A+l^+l^-$ is calculated by convoluting the $\gamma\gamma$ cross section with $\mathrm{d}^2N/\mathrm{d}W\mathrm{d}Y$:

$$\sigma(A+A \to A+A+l^+l^-) = \int\int \frac{\mathrm{d}^2N}{\mathrm{d}W\mathrm{d}Y}\sigma_{\gamma\gamma\to l^+l^-}(W)\mathrm{d}W\mathrm{d}Y \tag{3.12}$$

This approach is only valid for higher photon–photon invariant masses ($W >\sim 500$ MeV at the LHC). For lower invariant masses the interaction probability will be higher than 1, and higher order terms need to be included.

3.4 Photonuclear processes

Heavy–ion collisions at ultrarelativistic energies have been used to study various types of photonuclear interactions. Reviews can be found in [21, 22]. The focus has been on exclusive vector meson production, originally proposed in [26], but also photonuclear excitation e.g. into a Giant Dipole Resonance has been studied [27]. Photonuclear interactions have also been found to be an important background to peripheral, hadronic interactions [28].

The cross section for the reaction $A+A \to A+X$, proceeding via $\gamma+A \to X$ can be written using the equivalent photon approximation:

$$\sigma(A+A \to A+X) = \int \frac{n(\omega)}{\omega}\cdot\sigma_{\gamma+A\to X}(\omega)\mathrm{d}\omega, \tag{3.13}$$

where $n(\omega$ is the photon spectrum from a single nucleus discussed in Chapter 3.2, and $\sigma_{\gamma+A\to X}(\omega)$ is the photoproduction cross section. For a symmetric system, where any nucleus can be the photon emitter or target, the total cross section will be twice as large.

3.4.1 Exclusive vector meson production

There are some data on exclusive vector meson production at fixed target experiments. Coherent ρ^0 production on heavy nuclei was studied in the early 1970's at energies up to $W_{\gamma p} = 4.2$ GeV [29]. There are also some data on ω [30] and ϕ [31] photonuclear production at similar energies. More data, at higher energies have come from ultra–peripheral collisions at RHIC, and recently the LHC, as will be discussed in Section 3.5.

Exclusive photoproduction can be either coherent or incoherent. In coherent processes the photon couples coherently with the whole target nucleus. These processes are characterized by small transverse momentum for the final state ($\langle p_T \rangle \sim 60$ MeV/c). In most cases both nuclei will remain intact after the interaction. In an incoherent interaction a photon from one nucleus interacts with a single nucleon in the target nucleus. This will cause the target nucleus to break up, but except for single nucleons or fragments from the broken nucleus in the forward direction, no other particles are produced. The transverse momentum is higher than in coherent interactions ($\langle p_T \rangle \sim 500$ MeV/c).

Exclusive vector meson production is the dominant coherent interaction leading to the production of a hadronic final state [26]:

$$A + A \rightarrow A + A + V \tag{3.14}$$

In such reactions a vector meson is produced when a photon from the electromagnetic field of one of the nuclei interacts with the nuclear field of the other nucleus.

One can use Equation 3.13 to calculate the total vector meson cross section in A+A or p+p collisions. Changing variable from the photon energy ω to the rapidity y and differentiating results in:

$$\frac{\mathrm{d}\sigma(A + A \rightarrow A + A + V)}{\mathrm{d}y} = n(\omega_1)\sigma_{\gamma A \rightarrow VA}(\omega_1) + n(\omega_2)\sigma_{\gamma A \rightarrow VA}(\omega_2) \tag{3.15}$$

The relationship between ω and y is $\omega_{1,2} = (M_V c^2/2)\exp(\pm y)$, and M_V is the vector meson's mass. The differential cross section, $d\sigma/dy$, is therefore a direct measurement of the vector meson photoproduction cross section, if the photon flux is known. Away from $y = 0$ there is a two–fold ambiguity in the photon energy. At mid–rapidity, $y = 0$, the ρ^0 mass of 775 MeV/c^2 corresponds to a photon energy of $\omega = 388$ MeV. The equivalent γ–nucleon center–of–mass energy is then

$$W_{\gamma p} = \sqrt{4\omega E_p}, \tag{3.16}$$

where E_p is the energy of the beam. At LHC this corresponds to $W_{\gamma p} = 46$ GeV.

Exclusive photoproduction of vector meson has earlier been studied at HERA in $\gamma p \rightarrow V p$ interactions. The energy dependence of the cross section for photoproduction of different vector mesons, $\sigma(\gamma p \rightarrow V p)$, is shown in Figure 3.4. W is the center of mass energy of the photon–proton system. The energy dependence can be parametrised as W^{δ}, where δ represents the slope. The energy dependence is stronger for heavier vector mesons, like J/ψ ($\delta = 0.80$) than for lighter, like ρ^0 ($\delta = 0.22$).

Exclusive vector meson production can be understood from Vector Meson Dominance [33]. A photon will not always appear as a pure photon. According to quantum mechanics, it may with a certain probability fluctuate to a hadronic state. The photon

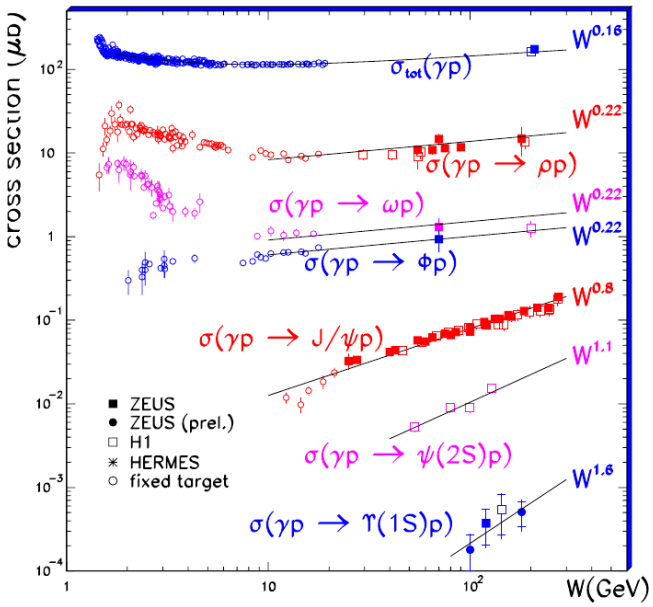

Figure 3.4: The cross section for diffractive vector meson production in the photoproduction kinematic regime ($Q^2 \sim 0$ GeV/c^2) in $\gamma p \to V p$ interactions. The results for various vector mesons are shown as a function of the center–of–mass energy of the γp system W, together with fits of the form W^{δ} [32].

has quantum numbers $J^{PC} = 1^{--}$, therefore it will fluctuate to a vector meson. The fluctuation's life time is determined by the uncertainty principle. A photon with energy E_γ and virtuality Q which fluctuates to a state of mass M_V has the lifetime of order:

$$\Delta t \approx \frac{\hbar}{\sqrt{M_V^2 2c^4 + Q^2 c^4}} \approx \frac{\hbar}{M_V c^2} \tag{3.17}$$

Because of the low virtuality of the photons, the last approximation is always true for hadron colliders.

The wave function of the photon can be written as a Fock decomposition:

$$|\gamma\rangle = C_{bare}|\gamma_{bare}\rangle + C_\rho|\rho\rangle + C_\omega|\omega\rangle + C_\phi|\phi\rangle + \ldots + C_q|q\bar{q}\rangle, \tag{3.18}$$

where $C_{bare} \approx 1$ and $C_V \sim \sqrt{\alpha_{em}}$ ($V = \rho, \omega, \phi \ldots$). The coefficients C_V, which represent the probability of finding the photon in state V,are related to the photon–vector meson coupling, f_V, through [22]

$$C_V = \frac{\sqrt{4\pi\alpha_{em}}}{f_V} \tag{3.19}$$

The coupling f_V can be determined from the measured leptonic decay widths, $\Gamma(V \to e^+e^-)$.

For pure Vector Meson Dominance, the scattering amplitude for the process $\gamma+A \rightarrow V+A$ can be written

$$A_{\gamma+A\rightarrow V+A}(s,t) = C_V A_{V+A\rightarrow V+A}(s,t) \tag{3.20}$$

The momentum transfer from the elastic scattering of the vector meson is assumed to be enough to make it real. This means that the photoproduction cross section is related to the elastic vector meson cross section:

$$\frac{\mathrm{d}\sigma(\gamma+A\rightarrow V+A)}{\mathrm{d}t} = C_V^2 \frac{\mathrm{d}\sigma(V+A\rightarrow V+A)}{\mathrm{d}t}, \tag{3.21}$$

where t is the momentum transfer from the target nucleus squared, and $d\sigma/dt = |A|^2$. In the Generalized Vector Meson Dominance Model (GVDM) one includes also so called cross terms $V'+A \rightarrow V+A$, and the relation between the photoproduction amplitude and the hadronic amplitudes is more complicated:

$$A_{\gamma+A\rightarrow V+A}(s,t) = \sum_V C_V' A_{V'+A\rightarrow V+A}(s,t) \tag{3.22}$$

The hadronic form factor determines the momentum transfer of the elastic scattering:

$$\frac{\mathrm{d}\sigma}{\mathrm{d}t} = \left.\frac{\mathrm{d}\sigma}{\mathrm{d}t}\right|_{t=0} |F(t)|^2 \tag{3.23}$$

The form factor reflects the size and shape of the target, as discussed in Chapter 2. If the spatial distribution is known it can, in principle, be calculated. An exponential function is a good representation of the form factor for proton targets. The form factor is then $|F(t)|^2 = \exp(-b|t|)$ with slope $b \approx 10$ GeV^{-2}c^2 for light vector mesons (ρ, ω) and $b \approx 4$ GeV^{-2}c^2 for the J/ψ. Because of the much smaller momentum transfer the form factor is peaked at much smaller momentum transfers for nuclear targets. The forward scattering amplitude, $d\sigma/dt(t=0)$, contains the dynamical information, which is related to the total vector meson cross section, through the optical theorem [22]:

$$\left.\frac{\mathrm{d}\sigma}{\mathrm{d}t}\right|_{t=0} = C_V^2 \frac{\sigma_{tot}^2(VA)}{16\pi\hbar^2}(1+\eta^2), \tag{3.24}$$

where η is the ratio of the real to the imaginary part of the scattering amplitude.

The forward scattering amplitude for heavy vector mesons has been calculated using the two–gluon exchange in QCD. To leading order, the result was [34]::

$$\left.\frac{\mathrm{d}\sigma(\gamma p\rightarrow Vp)}{\mathrm{d}t}\right|_{t=0} = \frac{\alpha_s^2\hbar^2\Gamma_{ee}}{3\alpha M_V^5 c^6} 16\pi^2 \left[xg(x,M_v^2/4)\right]^2, \tag{3.25}$$

where x is the fraction of the proton or nucleon momentum carried by the gluons. The gluon distribution, $g(x,Q^2)$, is evaluated at a momentum transfer $Q^2 = (M_V/2)^2$. Exclusive vector meson production is a very sensitive probe of the gluon distribution in protons and nuclei, due to the dependence of $\mathrm{d}\sigma/\mathrm{d}t$ on $(g(x))^2$.

3.4.2 Inclusive photonuclear processes

Because of the large total photon–hadron cross section and the high photon flux in hadron colliders, the rates for photonuclear interactions is high [22]. The photonuclear cross section is about 1/3 of the total Au+Au cross section, for photon–nucleon center–of–mass energies above 4 GeV, in Au+Au collisions at RHIC. Resolved interactions, where the photon fluctuates to a $q\bar{q}$ state, make the majority of the interactions. They are therefore similar to inelastic hadron–nucleon or hadron–nucleus collisions. The kinematics is similar to that of fixed target interactions, because the photon energies are much lower than the beam energies.

The photon may, however, also interact directly with a parton in the target nucleus. A pair of quarks can for example be produced through γ–gluon fusion. By convoluting the partonic cross section with the equivalent photon flux, $n(\omega)$, and the nuclear/nucleon gluon distribution, $G^A(x,Q^2)$, one gets the total photoproduction cross section $\sigma(A[\gamma]A \to Aq\bar{q}X)$:

$$\sigma(A[\gamma]A \to Aq\bar{q}X) = \int\int \frac{n(\omega)}{\omega} G^2(x,Q^2)\sigma_{\gamma g}(W_{\gamma g})\Theta(W_{\gamma g} - 2m_q c^2)\mathrm{d}\omega\mathrm{d}x \qquad (3.26)$$

Where $\sigma_{\gamma g \to q\bar{q}}(W_{\gamma g})$ is the cross section for the photoproduction of a $q\bar{q}$–pair,from photon–gluon fusion, which was discussed in Section 2.2.2 (Equation 2.41). $W_{\gamma p}$ is the γ–gluon center–of–mass energy and $W_{\gamma g}^2 = 2\omega x\sqrt{s}$, if the gluon carries a fraction x of the nucleon momentum.

Equation 3.26 is essentially equivalent to Equation 3.4 for two–photon interactions with the photon flux from the one nucleus replaced by the gluon distribution $G^A(x,Q^2)$. The final state $q\bar{q}$ rapidity depends on the gluon x and the photon energy. The cross section for $q\bar{q}$ peaks near the threshold $W_{\gamma g} \approx 4m_q^2$. In heavy–ion collisions at the LHC, mid–rapidity production of $c\bar{c}$– and $b\bar{b}$–pairs therefore mainly probes x–values of $x \sim 1 \cdot 10^{-3}$ ($c\bar{c}$) and $x \sim 3 \cdot 10^{-3}$ ($b\bar{b}$).

Colliding system	Flavour	σ [mb] No shadowing	σ [mb] EKS98	σ [mb] FGS
LHC Pb+Pb	$c\bar{c}$	1250	1050	850
LHC Pb+Pb	$b\bar{b}$	4.9	4.7	4.4

Table 3.1: $q\bar{q}$ cross sections in heavy ion collisions through direct photon–gluon fusion [22].

In Table 3.1 the cross sections for $c\bar{c}$ and $b\bar{b}$ are listed. A calculation that doesn't include shadowing is compared to calculations that include nuclear modifications. The effect of the shadowing is largest on the production of lighter quarks ($c\bar{c}$) (EKS98, FKS). It is worth noting that the cross section for $c\bar{c}$ production in Pb+Pb interactions at the LHC is about 1/6 of the total hadronic cross section.

Quark pairs can also be produced in two–photon interactions, or when a parton from the resolved photon interacts with a parton in the target, called anomalous interactions. Depending on quark flavour and collision energy, the anomalous cross sections are about 1–20% of the direct cross sections, while the two–photon cross sections are usually 1% of the anomalous cross sections.

3.5 Model predictions for photoproduction of ρ^0

Three different models predict the cross section for ρ^0 production at LHC energies. All models calculate the photon spectrum in impact parameter space as has been discussed above. The difference is in how the photonuclear cross section is calculated and the effects of the nuclear medium on the scattering.

In the Glauber model, a two–dimensional Fourier transform of the nuclear profile function, $\Gamma(b)$, gives the elastic amplitude [22]:

$$\frac{\mathrm{d}\sigma(\gamma+A\rightarrow V+A)}{\mathrm{d}t}=\frac{\pi}{\hbar^2}\left|\int e^{i\mathbf{p_T}\cdot\mathbf{b}/\hbar}\Gamma(\mathbf{b})\mathrm{d}^2b\right|^2 \tag{3.27}$$

The nuclear profile function is a function of the vector meson–nucleon forward scattering amplitude, f_{VN} and the distribution of matter inside the nucleus, $\rho(b,z)$:

$$\Gamma(b)=1-\exp\left[\frac{2i\pi\hbar c}{\omega}\int\rho(b,z')f_{VN}(0)\mathrm{d}z'\right] \tag{3.28}$$

This works for high photon energies, when $c\gamma\beta\Delta t > R_>$ when the interaction is longitudinally coherent over the whole nucleus.

Starlight [26, 35] is a Monte Carlo event generator developed by S. R. Klein and J. Nystrand. Experimental data for $\gamma+p\rightarrow\rho^0+p$ is used in combination with a Glauber model, neglecting the elastic part of the cross section.

The total vector meson nucleon cross section, $\sigma_{tot}(VN)$, was extracted using data on vector meson photoproduction with proton targets. This result was then used to calculate the total vector meson nucleus cross section, $\sigma_{tot}(VA)$, from the nuclear geometry.

Meson	**Au+Au, RHIC σ [mb]** $\sqrt{s_{NN}}=200$ **GeV**	**Pb+Pb, LHC σ [mb]** $\sqrt{s_{NN}}=5.5$ **TeV**
ρ^0	590	5200
ω	50	490
ϕ	39	460
J/ψ	0.29	32

Table 3.2: Cross sections for exclusive vector meson production in Au+Au and Pb+Pb interactions at RHIC and LHC at design energy, respectively[26].

A model developed by Frankfurt, Strikman and Zhalov (from now on called GGM) [36, 37] uses a generalized vector dominance model in the Gribov–Glauber approach. It includes non–diagonal transitions, $\gamma\rightarrow\rho'\rightarrow\rho$. The model uses the cross section $\sigma(\rho+\text{nucleon})$ from the Donnachie–Landshoff model, which is in agreement with HERA and lower energy data.

The coherent ρ^0 production cross section in Au+Au collisions at RHIC, was calculated using the Glauber model, in [36], resulting in a cross section of 934 mb, which is about 50% higher than the results in Table 3.2. This difference comes from the fact that the calculations in Table 3.2 were done assuming that $\sigma_{tot}(\rho A)\approx\sigma_{inel}(\rho A)$,

while [36] included the contribution from off–diagonal elements, corresponding to $\rho' + Au \rightarrow \rho + Au$ scattering, and a non–zero real part of the forward scattering amplitudes (η in Equation 3.24).

A model developed by Gonçalves and Machado (from now on called GM) [38] is based on the color dipole model in combination with saturation from a Color Glass Condensate model.

The predictions for the different models can be seen in Table 3.3 and Figure 3.5. For a discussion about the models compared to the results from RHIC see Section 3.6.

Model	**Cross section**, $d\sigma/dy$ **[mb]**
GGM	720
GM	470
Starlight	380

Table 3.3: Predicted cross section at mid–rapidity ($y = 0$), for Pb–Pb collisions at $\sqrt{s_{NN}} = 2.76$ GeV, for the three models, GGM[36, 37], GM[38] and Starlight[26, 35].

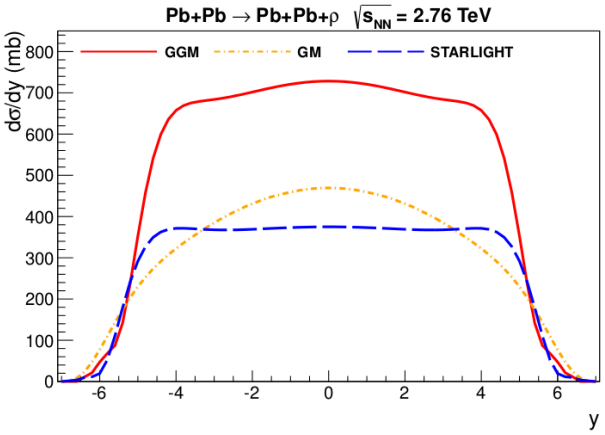

Figure 3.5: Model predictions for the models GGM [36, 37], shown with a full red line, GM [38], shown with a yellow chained line and Starlight [26, 35], shown with a blue dashed line.

3.6 Results from RHIC

Photoproduction of ρ^0's has earlier been studied by the STAR experiment at the Relativistic Heavy Ion Collider (RHIC) in Au–Au collisions at 62.4 GeV, 130 GeV and 200 GeV [39–41]. The PHENIX collaboration has studied photoproduction of J/ψ, and high mass e^+e^- pairs in ultra–peripheral Au–Au collisions at $\sqrt{s_{NN}} = 200$ GeV [42].

3.6.1 Photoproduction of ρ^0 in STAR

In STAR the charged particle tracks are reconstructed in a cylindrical Time Projection Chamber (TPC), which is a 4.2 meter long barrel with 2 meter radius operated in a magnetic field. In the studies discussed here, the TPC was surrounded by 240 Central Trigger Barrel (CTB) scintillator slats. Two zero degree hadron calorimeters (ZDCs) are located ± 18 meters from the interaction point. The ZDCs are sensitive to the neutral remnants from nuclear break up, with an acceptance close to unity. [39–41]

Three different triggers were used for ultraperipheral collisions, a low multiplicity topology trigger and two minimum bias triggers. For the topology trigger the CTB was divided in four azimuthal quadrants. A coincidence between left– and right–side quadrants was required, while the top and bottom quadrants was used as vetoes to suppress cosmic rays. The topology trigger was used for data collection at $\sqrt{s_{NN}}$ = 130 GeV and $\sqrt{s_{NN}}$ = 200 GeV. For the first minimum bias trigger (trigger A), a coincidence signal in both ZDCs was required. This was used to collect data for all three data samples. For the data collection at $\sqrt{s_{NN}}$ = 62.4 GeV, an additional minimum bias trigger (trigger B) was used, which also required a charged particle signal in the CTB, in coincidence with the ZDC signal. [39–41]

In the analysis of the three data samples events with exactly two oppositely charged tracks, forming a common vertex, was selected. A ρ^0 event from photoproduction should have exactly two tracks in the TPC, but additional tracks may come from overlapping interactions. Events with at least one neutron (*xn, xn*), exactly one neutron (*1n, 1n*), or no neutrons (*0n, 0n*) in each ZDC, and events with at least one neutron in exactly one ZDC (*xn, 0n*), were selected using the energy deposit in the ZDCs. The latter two can only occur with the topology trigger. The selected events were required to have $p_T < 150$ MeV/c. The background in the analysis consisted of peripheral hadronic interactions, other photonuclear interactions, e^+e^- pairs from two–photon processes, beam–gas interactions, cosmic ray muons, and pile–up events. Cuts in total multiplicity, vertex position and other event characteristics reduced the background. Because of the low background after the selection cuts, all track pairs were assumed to be pions.

Integrated luminosities of 45 mb^{-1}, 59 mb^{-1}, and 461 mb^{-1} were collected with trigger A at $\sqrt{s} = 62.4$ GeV, 130 GeV, and 200 GeV respectively. At $\sqrt{s_N N}$ = 62.4 GeV and additional 781 mb^{-1} was collected with trigger B. At this energy the analysis is therefore based on the data from trigger B.

The STAR detector is in many aspects similar to the central barrel in ALICE. Both experiments have a TPC as the main tracking detector, and both have a trigger detector for charged particles surrounding it (CTB in STAR, TOF in ALICE). Both experiments are equipped with Zero–Degree Calorimeters for detecting forward neutrons. The principles for the event selection is also very similar, as will be discussed further in Chapter 5.

But there are also some difference. STAR had to apply a topology cut for the CTB trigger. This was not necessary in ALICE. ALICE is located $\sim$60 meters underground and the cosmic ray flux is therefore substantially reduced. Furthermore, one of the ALICE UPC triggers required a hit in the SPD which occupies a much smaller volume than the surface of the TPC. STAR was able to trigger on a ZDC–signal at the lowest trigger level. This is not possible in ALICE because of the trigger latency and the much longer distance from the collision point to the ZDCs (116 m).

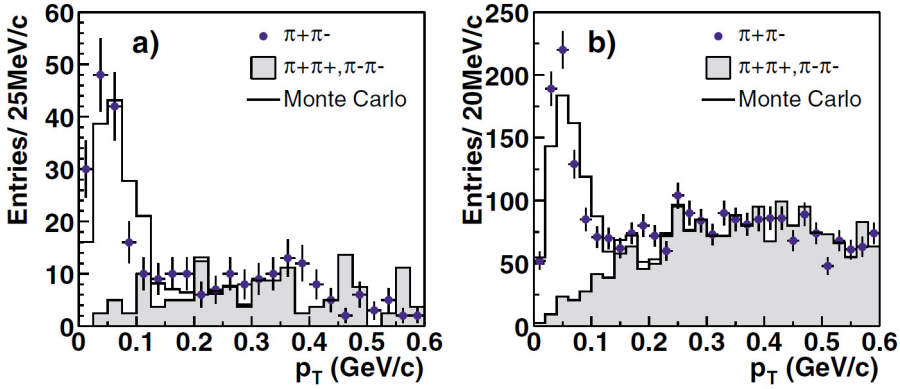

Figure 3.6: The p_T spectra of pion pairs for the two–track events selected by (a) the topology trigger (*0n, 0n*) and (b) the minimum bias trigger (*xn, xn*) Points are oppositely charged pairs, and the shaded histograms are the normalized like–sign combinatorial background. The open histograms are simulated ρ^0 superimposed onto the background [40].

The uncorrected transverse momentum spectra of pion pairs for the two track events samples of the topology trigger (*0n, 0n*), and the minimum bias trigger (*xn, xn*) at $\sqrt{s_{NN}}$ = 130 GeV are shown in Figure 3.6. As expected for coherent photoproduction, both spectra peak around 50 MeV/c. The peak is not seen in a background model from like sign pairs.

The $d\sigma(AuAu \to Au^*Au^*\rho)/dM_{\pi\pi}$ invariant mass spectrum for the (*xn, xn*) events, with $p_T < 150$ MeV/c from the 200 GeV data sample is shown in Figure 3.7. The spectrum is fitted with:

$$\frac{\mathrm{d}\sigma}{\mathrm{d}M_{\pi\pi}} = \left| A\frac{\sqrt{M_{\pi\pi}M_\rho\Gamma_\rho}}{M^2_{\pi\pi} - M^2_\rho + iM_\rho\Gamma_\rho} + B \right|^2 + f_p \tag{3.29}$$

Here

$$\Gamma_\rho = \Gamma_0 \cdot (M_\rho M_{\pi\pi} \cdot [(M^2_{\pi\pi} - 4m^2_\pi)/(M^2_\rho - 4m^2_\pi)]^{3/2} \tag{3.30}$$

is the momentum dependent width, M_{ρ^0} is the mass of the ρ^0, A is the amplitude for the Breit–Wigner function, B is the amplitude for the direct $\pi^+\pi^-$ production, and f_p is the fixed second–order polynomial used to describe the background. The same fit function was used to fit the invariant mass spectra at all three energies. The invariant masses, widths, and $|B/A|$ ratios coming from the fits at the different energies are listed in Table 3.4.

Figure 3.8 shows the ρ^0 spectrum as a function of momentum transfer squared, t, for the minimum bias data set. The $d^2\sigma/dydt$ distribution was fitted with Equation 3.31.

$$\frac{\mathrm{d}^2\sigma}{\mathrm{d}y\mathrm{d}t} = A_{coh}\exp(-B_{coh}t) + A_{inc}\exp(-B_{inc}t) \tag{3.31}$$

To find the ratio between the incoherent and coherent total cross sections, the two exponentials in Equation 3.31 were integrated.

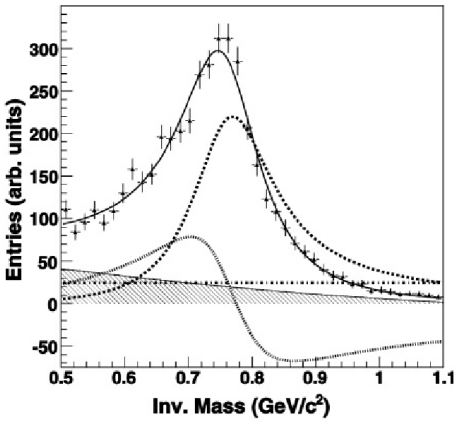

Figure 3.7: The invariant mass distribution of the coherently produced ρ^0 candidates from the minimum bias sample with the cut on the transverse momentum $p_T < 150$ MeV/c. The hatched area is the contribution from the combinatorial background. The solid line corresponds to Equation 3.29, which encompasses the Breit–Wigner part (dashed), the mass–independent contribution from the direct $\pi^+\pi^-$ production (dash–dotted), and the interference term (dotted) [41].

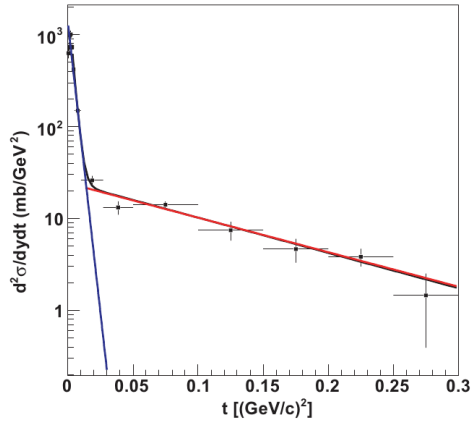

Figure 3.8: ρ^0 production cross section as a function of the momentum transfer squared, t, together with the fit of Equation 3.31 [41].

Data sample	M_ρ (MeV/c^2)	Γ_ρ (MeV/c^2)	$\lvert B/A \rvert$
62.4 GeV	764 ± 9	140 ± 13	$0.88 \pm 0.009 \pm 0.009$
130 GeV	777 ± 7	139 ± 13	$0.81 \pm 0.08 \pm 0.20$
200 GeV	775 ± 3	162 ± 7	$0.89 \pm 0.08 \pm 0.09$

Table 3.4: Invariant mass, width and the fraction $|B/A|$ from the three different data samples [39–41].

The cross sections were extrapolated from $|y| > 1$ to the full 4π acceptance, using extrapolation factors obtained from simulations from the Starlight Monte Carlo. In Table 3.5 the resulting cross sections for the coherent photoproduction of ρ^0 at full rapidity is listed.

	STAR		
Cross section	$\sqrt{s_{NN}}$ = 62.4 GeV (mb)	$\sqrt{s_{NN}}$ = 130 GeV (mb)	$\sqrt{s_{NN}}$ = 200 GeV (mb)
σ_{XnXn}	$10.5 \pm 1.5 \pm 1.6$	$28.3 \pm 2.0 \pm 6.3$	$31.9 \pm 1.5 \pm 4.5$
σ_{0nXn}	$31.8 \pm 5.2 \pm 3.9$	$95 \pm 60 \pm 25$	$105 \pm 5 \pm 15$
σ_{0n0n}	$78 \pm 14 \pm 13$	$370 \pm 170 \pm 80$	$391 \pm 18 \pm 55$
σ_{total}	$120 \pm 15 \pm 22$	$460 \pm 220 \pm 110$	$697 \pm 25 \pm 73$

Table 3.5: The total cross section extrapolated to the full rapidity range for coherent and coherent ρ^0 production at $\sqrt{s}$ = 62.4 GeV, 130 GeV and 200 GeV, accompanied by nuclear breakup and without nuclear breakup. The first error is statistical and the second error is systematic [39–41].

In Figure 3.9 a comparison of the measurements of the differential cross section at $\sqrt{s_{NN}}$ = 200 GeV to theoretical models, is shown. Because of the limited rapidity acceptance, it was not possible to distinguish the different theoretical models based on the shape. The amplitude can however be used to eliminate models that that significantly overestimate the total production cross section in the measured rapidity range.

In Figure 3.10 the results from the three measurements are compared with models [26, 36, 37, 43]. The measured rise in cross section with energy was smaller than predicted by the two models that use Glauber calculations, KN and FSZ, which predicted ratios around 6.1. The measured ratio was closer to the models IPSAT–GM and IIM–GM, which predicted 3.5 and 4.2 respectively. The measured 12% increase in the coherent photoproduction cross section from $\sqrt{s_{NN}}$ = 130 GeV to $\sqrt{s_{NN}}$ = 200 GeV is much less than predicted by all three models ([25], [36] and [44]), which predict cross section increases of between 70% and 80% [41].

These results from STAR and the energy dependence of the ρ^0 cross section will be compared with the result from LHC in this thesis in Chapter 6.

3.6.2 Photoproduction of J/ψ at $\sqrt{s_{NN}}$ = 200 GeV in PHENIX

The PHENIX detector is quite different from STAR and ALICE. Its central tracking system, which consists of two arms, is focussed on reconstructing electrons. Each of the arms consist of multi–layer drift chambers (DC) followed by Multiwire Proportional

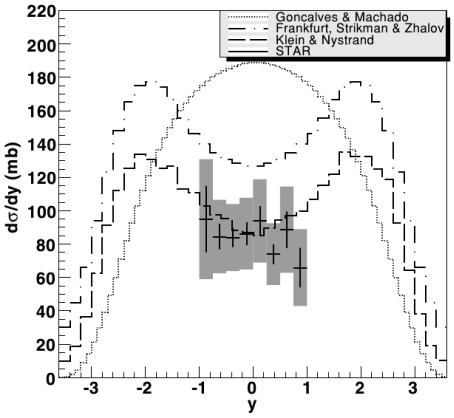

Figure 3.9: Comparison of theoretical predictions to the measured differential cross section for coherent ρ^0 production. The statistical errors are shown by the solid vertical line at each data point. The sum of the statistical and systematic error bars is shown by the grey band [41].

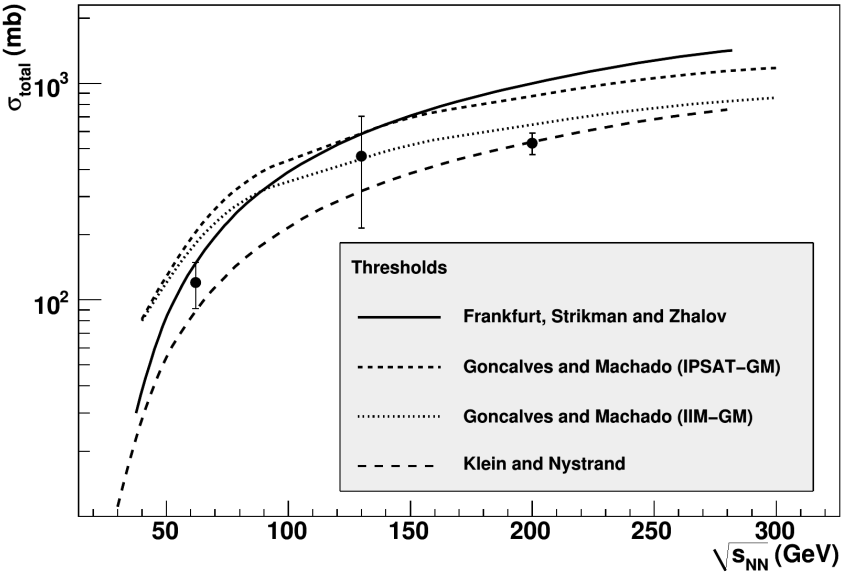

Figure 3.10: Comparison of the measured total cross section of photoproduced ρ^0 to different theoretical models [39].

Chambers (MWPC), Ring–Imaging Čerenkov Detectors (RICH), and electromagnetic calorimeters (EMCal), for electron and positron identification. The two arms each have a rather narrow acceptance of $|\eta| < 0.35$, and $\Delta\phi = \pi/2$. In addition to the central tracking system, there are muon detectors at forward and backward rapidities, as well as hadronic Zero–Degree Calorimeters placed 18 m up– and down–stream of the interaction point.

The events used in the analysis of ultra–peripheral collisions were collected using a special UPC trigger during the 2004 Au–Au run [42]. The trigger required a veto on coincident signals in both Beam–Beam Counters (BBC), which covers $3.0 < |\eta| < 3.9$ and full azimuth, to select events with large rapidity gaps on each side of the central arm. It was also required an EMCal trigger with a threshold of 0.8 GeV. To select events with forward nuclear emission from a single or double Au* decay, it was required that at least 30 GeV energy was deposited in one or both ZDCs. The trigger efficiency was estimated to be $\varepsilon_{trigg}^{e^+e^-} = 0.9 \pm 0.1$. In total 6.7 million events which satisfied standard data quality assurance criteria were collected, corresponding to an integrated luminosity of $114 \pm 12\ \mu\mathrm{b}^{-}1$.

Several cuts were applied to the data. The events were required to have only two tracks, to select only exclusive processes with two particles in the final state. The tracks should have a signal in RICH and at least one of the tracks should have an EMCal energy above 1 GeV. In addition to these cuts only events where the two e^+e^- candidates were detected in opposite arms were selected. After these cuts were applied there were no remaining like–sign background.

In Figure 3.11 a) the invariant mass distribution of the measured e^+e^- signal is shown. Only pairs with $m_{e^+e^-} > 2$ GeV/c^2 were included, since the requirement that at least one of the particles should have energy larger than 1 GeV caused a sharp drop in efficiency for $m_{e^+e^-} < 2$ GeV/c^2. The invariant mass distribution was fitted with a Gaussian for the J/ψ peak, and an exponential function for the continuum. The dashed curves show the maximum and minimum e^+e^- continuum distributions considered, including the statistical and systematic uncertainties. In Figure 3.11 the fitted exponential continuum distribution was subtracted from the total distribution of e^+e^- pairs. The total number of J/ψ found were $N_{J/\psi} = 9.9 \pm 4.1$ (stat.) ± 1.0 (syst.), while the total number of e^+e^- continuum pairs were $N_{e^+e^-}(2.0 \leq M_{inv} \leq 2.8)\mathrm{GeV/c}^2 = 13.7 \pm$ (stat.) ± 1.0 (syst.).

The cross section for photoproduction at mid–rapidity in ultra–peripheral gold–gold collisions was calculated using the yields of J/ψ's and e^+e^- pairs. The cross section for dielectrons at mid–rapidity are given in Table 3.6 and compared with Starlight.

The differential cross section at mid–rapidity for the J/ψ was found to be:

$$\left.\frac{\mathrm{d}\sigma_{J/\psi+Xn}}{\mathrm{d}y}\right|_{|y|<0.35} = 75 \pm 31\ (\mathrm{stat.})\ \pm 15\ (\mathrm{syst.})\ \mu\mathrm{b} \tag{3.32}$$

The PHENIX e^+e^- measurements have large statistical errors, but are in good agreement with Starlight.

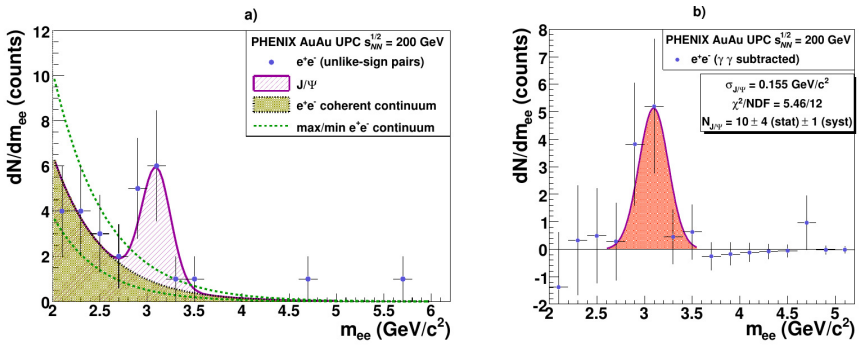

Figure 3.11: a): Invariant mass distribution of e^+e^- pairs fitted to the combination of an exponential function for the dielectron continuum and a Gaussian for the J/ψ signal. The two dashed curves indicate the maximum and minimum continuum contributions. b): J/ψ invariant mass distribution after subtraction of the fitted dielectron continuum signal [42].

$m_{e^+e^-}$ GeV/c^2	Data	Starlight
e^+e^- (2.0 – 2.8)	86 ± 23 (stat.) ± 16 (syst.)	90
e^+e^- (2.0 – 2.3)	129 ± 47 (stat.) ± 28 (syst.)	138
e^+e^- (2.3 – 2.8)	60 ± 24 (stat.) ± 14 (syst.)	61

Table 3.6: e^+e^- photoproduction cross sections at mid–rapidity in Au–Au collisions at $\sqrt{s_{NN}} = 200$ GeV compared with Starlight predictions [42].

3.7 UPC results from LHC

The ALICE collaboration has measured photoproduction of J/ψ in ultra–peripheral Pb–Pb collisions at $\sqrt{s} = 2.76$ TeV at forward [45] and mid–rapidity [46]. These measurements will be discussed further below. In addition, LHCb has measured exclusive photoproduction of J/ψ in pp collisions [47], and CMS has measured two–photon production of $\mu^+\mu^-$–pairs [48] and W^+W^-–pairs [49] in pp collisions.

3.7.1 Photoproduction of J/ψ

The content in this section based on references [45, 46].

The J/ψ is measured through its muon decay channel, using the muon spectrometer, which has a rapidity acceptance of $-3.6 < y < -2.6$, and at central rapidity using the central barrel. The analyses were done on events collected with special triggers during the 2011 Pb–Pb run. The trigger (FUPC) was configured to select two–muon events coming from $\gamma\gamma \to \mu^+\mu^-$ processes or J/ψ decays. The trigger required a single muon trigger with $p_T > 1$ GeV/c in coincidence with at least one hit in VZERO–C and no hits in VZERO–A. (The VZERO detectors are arrays of scintillator detectors at forward and backward rapidity which will be further discussed in Chapter 4.) In addition a special barrel ultra-peripheral collisions trigger (BUPC) was set up. The trigger required at

least two hits in the ALICE Si–pixel detector; between two and six fired pads in the Time–Of–Flight detector, where at least two of them difference in azimuth in the range $150^\circ \leq \Delta\phi \leq 180^\circ$; and no hits in VZERO–A or VZERO–C detectors.

Each event should have exactly two electrons or muons, and the rest of the detector should be empty. For the central barrel analysis the VZERO detectors on both sides were used as veto, whereas for the muon arm analysis only the VZERO–A (on the opposite side of the muon arm) was used.

In the central barrel the event selection was based on the following requirements [46]:

- The event was required to have between one and ten tracks, based on loose track requirements: Each track should have at least 50% of the findable TPC clusters, where at least 20 clusters match those found in the ITS.
- The event was required to have a reconstructed primary vertex.
- The event was required to have exactly two tracks passing stricter requirements: Each track should have at least 70 TPC cluster, one ITS cluster, and no kink. In addition the tracks should be extracted back to the primary vertex.
- At least one of the two accepted tracks, should have a $p_T > 1$ GeV/c, to reduce the background without affecting the signal.
- It was required that there were no signal in the VZERO–A or VZERO–C detectors.
- The energy loss of the tracks was required to be compatible with either muons or electrons. are plotted versus the energy loss of the negative leptons.
- The two tracks were required to have either opposite or the same charge, depending on the analysis.
- The invariant mass of the track pairs should be in the range $2.2 < M_{inv} < 6.0$ GeV/c^2.

Similar cuts were applied in the ρ^0 analysis of this thesis as will be discussed in Chapter 5. In addition to the requirements above a sample with a cut in transverse momentum, $p_T < 200$ MeV/c for muon pairs and $p_T < 300$ MeV/c for electron pairs, was made to increase the number of coherent events. An additional cut on the energy deposited in the Zero–Degree Calorimeters, corresponding to six neutrons, was also done. A sample with at enrichment of incoherent events was also made, by requiring $p_T > 200$ MeV/c for muon pairs, and $p_T > 300$ MeV/c for electron pairs.

To calculate the efficiency and acceptance of the J/ψ reconstruction Starlight [35] events folded with the detector Monte Carlo simulation was used. The ratio between the number of selected events to the number of generated events was taken as the product of the acceptance and efficiency, $Acc \times Eff$.

Figure 3.12 shows the invariant mass distribution for opposite sign muon pairs in the range $2.8 < M_{inv} < 3.4$ GeV/c^2, measured by the muon spectrometer. A J/ψ peak can be seen on top of a continuum from $\gamma\gamma \to \mu^+\mu^-$. The number of J/ψ's was extracted by fitting the invariant mass spectrum in the range $2.2 < M_{inv} < 4.6$ GeV/c^2

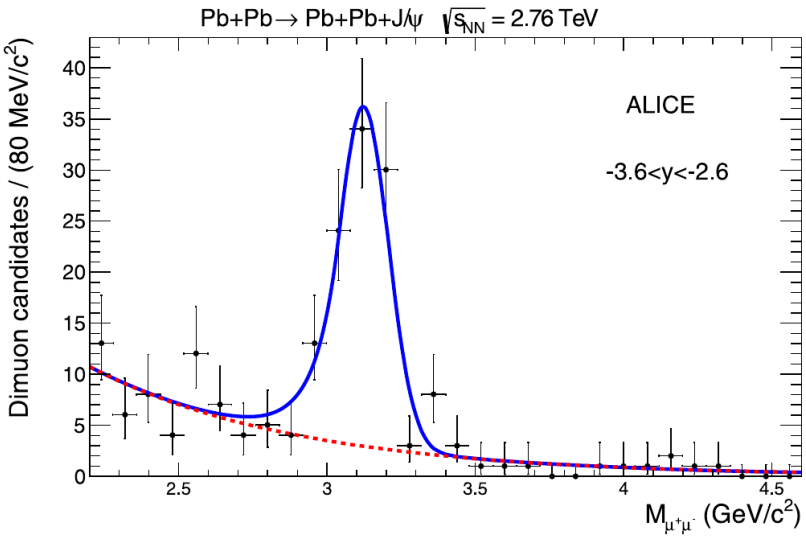

Figure 3.12: Invariant mass distribution for events with exactly two oppositely charged muons satisfying the event selection described in the text [45].

with a Crystal Ball function [50] for the J/ψ signal, and an exponential function for the underlying continuum. The extracted number of J/ψ's at forward rapidity was $N_{yield} = 96 \pm 12(\text{stat.}) \pm 6(\text{syst.})$. For the central barrel a yield of $N_{yield} = 265 \pm 40$ (stat.) $\pm$ 12 (syst.) was obtained in the $J/\psi \to e^+e^-$ channel, while in the $J/\psi \to \mu^+\mu^-$ sample a yield of $N_{yield} = 291 \pm 18$ (stat.) ± 4 (syst.) was found. The systematic error in the yield was found from varying the bin size and and replacing the exponential with a polynomial function for the $\gamma\gamma$ spectrum.

In Figure 3.13 the transverse momentum distributions for the dielectron (right) and dimuon (left) samples are shown. The peak at low p_T mainly comes from coherent photoproduction, while the tail extending to $\sim$1 GeV/c mainly comes from incoherent photoproduction. The fraction of incoherent events (f_I) under the coherent peak was estimated using theoretical calculations and by using six different functions to fit the measured p_T spectrum: Coherent J/ψ production, incoherent J/ψ production, J/ψ from coherent ψ' decay, J/ψ from incoherent ψ' decay, $\gamma\gamma$ continuum, and J/ψ produced in peripheral hadronic collisions.

The fraction, f_D, of the J/ψ mesons coming from decaying ψ' was estimated, for both the forward and the central rapidity region. The fraction was found to be in the region of 10%. The fraction of incoherent events under the coherent peak, was found to be about 12–15% for muons at forward and central rapidity, and about 5% for the electron channel in the central barrel.

The total number of coherently photoproduced J/ψ's was calculated using the formula [45, 46]:

$$N^{coh}_{J/\psi} = \frac{N_{yield}}{1 + f_I + f_D} \tag{3.33}$$

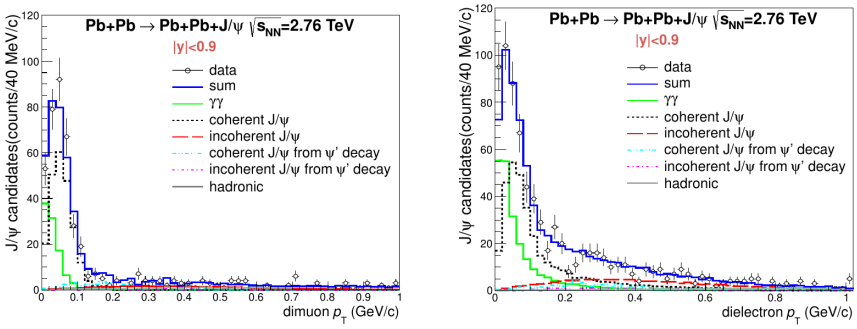

Figure 3.13: Transverse momentum distributions for the muon pairs (left) and electron pairs (right) for UPC events measured in the ALICE central barrel at $\sqrt{s_{NN}} = 2.76$ TeV, in the rapidity interval $-0.9 < y < 0.9$. For the muon pairs the invariant mass range is $3.0 < M_{inv} < 3.2$ GeV/c^2, while it is $2.2 < M_{inv} < 3.2$ GeV/c^2 for the electron pairs. The p_T range is extended to 1 GeV/c on a linear scale. Six Monte Carlo templates were used to fit the data points: Coherent J/ψ production (black), incoherent J/ψ production (red), J/ψ from coherent ψ' decay (light blue), J/ψ from incoherent ψ' decay (violet), $\gamma\gamma$ (green), and J/ψ produced in peripheral hadronic collisions (grey). The solid blue histogram is the sum of the Monte Carlo templates [46].

which gave $N^{coh}_{J/\psi}(\mu^+\mu^-) = 255 \pm 16$ (stat.) $^{+14}_{-13}$ (syst.) and $N^{coh}_{J/\psi}(e^+e^-) = 212 \pm 32$ (stat.) $^{+14}_{-13}$ (syst.) in the central barrel, and $N^{coh}_{J/\psi} = 78 \pm 10$ (stat.) $^{+7}_{-11}$ (syst.) in the muon arm.

The ultra–peripheral muon arm trigger selected $\gamma\gamma \to \mu^+\mu^-$ events, in addition to the exclusive J/ψ events. The characteristics of such events are very similar to that of the J/ψ. The ratio of the cross section of $\gamma\gamma \to \mu^+\mu^-$ events and J/ψ events is independent of luminosity and trigger efficiency [45]:

$$\frac{\mathrm{d}\sigma^{coh}_{J/\psi}}{\mathrm{d}y} = \frac{1}{BR(Jpsi \to \mu^+\mu^-)} \cdot \frac{N^{coh}_{J/\psi}}{N_{\gamma\gamma}} \cdot \frac{(Acc \times Eff)_{\gamma\gamma}}{(Acc \times Eff)_{J/\psi}} \cdot \frac{\sigma_{\gamma\gamma}}{\Delta y}, \tag{3.34}$$

where $N_{\gamma\gamma}$ was found by counting the number of events in the invariant mass ranges $2.2 < M_{inv} < 2.6$ GeV/c^2 and $3.5 < M_{inv} < 6.0$ GeV/c^2, which gave $N_{\gamma\gamma} = 43 \pm 7$ (stat.) and $N_{\gamma\gamma} = 15 \pm 4$ (stat.) respectively. Starlight was used to determine $\sigma_{\gamma\gamma}$. The cross section for dimuon invariant mass between $2.2 < M_{inv} < 2.6$ GeV/c^2 or $3.5 < M_{inv} < 6.0$ GeV/c^2, with dimuon rapidity in the interval $-3.6 < y < -2.6$ and each muon satisfying $-3.7 < \eta_{1,2} < -2.5$ is $\sigma_{\gamma\gamma} = 17.4\mu$b [45]. The $(Acc \times Eff)_{\gamma\gamma}$ for events satisfying the same selection was calculated using Starlight including detector response. The data cuts were the same as for the J/ψ data analysis, which gave an $(Acc \times Eff)_{\gamma\gamma}$ of 42.1% [45]. The differential cross section for coherent J/ψ production integrated over the rapidity interval $-3.6 < y < -2.6$ was found to be $\mathrm{d}\sigma^{coh}_{J/\psi}/\mathrm{d}y = 1.0 \pm 0.18(\mathrm{stat.})^{+0.24}_{-0.26}(\mathrm{syst.})$ mb [45].

The differential cross section for coherent J/ψ production in the central barrel was

calculated using [46]:

$$\frac{\mathrm{d}\sigma^{coh}_{J/\psi}}{\mathrm{d}y} = \frac{N^{coh}_{J/\psi}}{(Acc \times Eff) \cdot BR(J/\psi \to l^+l^-) \cdot \mathscr{L}_{int} \cdot \Delta y}, \tag{3.35}$$

where $N^{coh}_{J/\psi}$ is the number of J/ψ candidates from Equation 3.33 $(Acc \times Eff)$ is the acceptance times efficiency, $BR(J/\psi \to l^+l^-)$ is the branching ratio for a J/ψ to decay into two leptons, Δy is the rapidity interval, and $\mathscr{L}_{int}$ is the integrated luminosity. In the electron channel this gave $\frac{\mathrm{d}\sigma^{coh}_{J/\psi}}{\mathrm{d}y} = 3.19 \pm 0.50\ (\text{stat.})\ ^{+0.45}_{-0.31}\ (\text{syst.})$ mb, and in the muon channel the result was $\frac{\mathrm{d}\sigma^{coh}_{J/\psi}}{\mathrm{d}y} = 2.27 \pm 0.14\ (\text{stat.})\ ^{+0.30}_{-0.20}\ (\text{syst.})$ mb. The weighted average of the differential cross section from the two channels gave $\frac{\mathrm{d}\sigma^{coh}_{J/\psi}}{\mathrm{d}y} = 2.38^{+0.34}_{-0.22}$ (stat. + syst.) mb. The fraction of coherent events with no neutron emission was calculated to be $F_n = 0.70 \pm 0.05$ (stat.) , compared to the estimates from Starlight of $F_n = 0.68$ and Reference [51] of $F_n = 0.76$.

In the central barrel analysis also the cross section for incoherent photoproduction of J/ψ was calculated, using a similar approach as for the coherent photoproduction. The extracted yield was $N_{yield} = 61 \pm 14\ (\text{stat.})\ ^{+16}_{-7}\ (\text{syst.})$ for the electron sample and $N_{yield} = 91 \pm 15\ (\text{stat.})\ ^{+7}_{-5}\ (\text{syst.})$ for the muon sample. The fraction of incoherent J/ψ's coming from $\psi' \to J/\psi + X$, f_D, was calculated using Starlight and Reference [51]. Using the average of these models gave the results $f_D = (9.5 \pm 5.5)\%$ for the muon channel and $f_D = (11 \pm 7)\%$ for electrons. The fraction of coherent events in the incoherent sample, f_C, was estimated by fitting the measured transverse momentum distribution in Figure 3.13. For the dielectron sample the result was $f_C = (0.47 \pm 0.09)$, while a fraction of $f_C = (0.03 \pm 0.03)$ was extracted for the dimuon channel. This was compatible with model calculations, and used in the cross section calculation. The total number of incoherently produced J/ψ's was calculated using [46]:

$$N^{inc}_{J/\psi} = \frac{N_{yield}}{1 + f_C + f_D}, \tag{3.36}$$

which gave $N^{inc}_{J/\psi}(e^+e^-) = 39 \pm 9\ (\text{stat.})\ ^{+10}_{-5}\ (\text{syst.})$ for the electrons and $N^{inc}_{J/\psi}(\mu^+\mu^-) = 81 \pm 13\ (\text{stat.})\ ^{+8}_{-6}\ (\text{syst.})$ for the muons. This corresponds to differential cross sections of $\mathrm{d}\sigma^{inc}_{J/\psi}/\mathrm{d}y = 0.87 \pm 0.20\ (\text{stat.})\ ^{+0.26}_{-0.14}\ (\text{syst.})$ mb and $\mathrm{d}\sigma^{inc}_{J/\psi}/\mathrm{d}y = 1.03 \pm 0.17\ (\text{stat.})\ ^{+0.15}_{-0.12}\ (\text{syst.})$ mb respectively. The weighted average of these to results gave $\mathrm{d}\sigma^{inc}_{J/\psi}/\mathrm{d}y = 0.98^{+0.19}_{-0.17}$ (stat. + syst.) mb [46].

The cross section for the process $\gamma\gamma \to e^+e^-$ was calculated using the formula:

$$\sigma_{\gamma\gamma} = \frac{N_{\gamma\gamma}}{(Acc \times Eff) \cdot \mathscr{L}_{int}}, \tag{3.37}$$

where $N_{\gamma\gamma}$ is the number of lepton pairs, which was obtained by fitting the continuum in the invariant mass intervals $2.2 < M_{inv} < 2.6$ GeV/c^2 and $3.7 < M_{inv} < 10.0$ GeV/c^2. This gave a yield of $N^{e^+e^-}_{\gamma\gamma} = 186 \pm 13\ (\text{stat.})\ \pm 4\ (\text{syst.})$ for the lower interval and $N^{e^+e^-}_{\gamma\gamma} = 93 \pm 10\ (\text{stat.})\ \pm 4\ (\text{syst.})$ for the lower interval. The $(Acc \times Eff)$

was estimated to be about 5% in both intervals. For the lower invariant mass interval this gave a cross section of $\sigma_{\gamma\gamma}^{e^+e^-} = 154 \pm 11$ (stat.) $^{+16.6}_{-10.8}$ (syst.) μb, and $\sigma_{\gamma\gamma}^{e^+e^-} = 91 \pm 10$ (stat.) $^{+10.9}_{-8.0}$ (syst.) μb. Starlight predicts $\sigma = 128$ μb and $\sigma = 77$ μb for the higher and lower invariant mass interval respectively.

3.7.2 Comparison of the J/ψ cross sections with models

The results on the cross sections at forward and mid–rapidity was compared to different models [26, 51–55]. The differences between the models come mainly from the way the photonuclear interaction is treated.

The models can be divided in three categories [45, 46]:

1. In the model that includes no nuclear effects (AB–MSTW08) all the nucleons contribute to the scattering, and the differ cross section $\mathrm{d}\sigma/\mathrm{d}t$ at $t = 0$, where t is the momentum transfer from the target nucleus squared, scales with the number of nucleons squared.

2. The models Starlight, GM, CSS and LM use a Glauber approach to calculate the number of nucleons that contributes to the scattering. The calculated cross section depends on the nuclear geometry and the total J/ψ cross section.

3. The models AB–EPS08, AB–EPS09, AB–HKN07, and RSZ–LTA are partonic models where the cross section is proportional to the nuclear gluon distribution squared.

The predictions from the models are compared to the measurement of the coherent cross section of $\mathrm{d}\sigma_{J/\psi}^{coh}/\mathrm{d}y = 1.0 \pm 0.18(\mathrm{stat.})^{+0.24}_{-0.26}(\mathrm{syst.})$ mb at forward rapidity, and the coherent cross section $\frac{\mathrm{d}\sigma_{J/\psi}^{coh}}{\mathrm{d}y} = 2.38^{+0.34}_{-0.22}$ (stat. + syst.) mb at mid–rapidity. Figure 3.14 a) shows a comparison of the cross section integrated over the rapidity range $-3.6 < y < -2.6$ [45] and $-0.9 < y < 0.9$ [46]. In addition the reflection of the data point at forward rapidity is shown. At mid–rapidity the model AB–EPS09, which include nuclear gluon shadowing, is in very good agreement with the measured cross section. This model is also in agreement (within one standard deviation) with the measurement at forward rapidity. The models using a Glauber approach overestimates the cross section with more than three standard deviations at mid–rapidity. The same is true for the model AB-HKN07, which includes less gluon shadowing than AB–EPS09.

The model AB–EPS08 agrees within one standard deviation with the measurement at forward rapidity, but underestimates the cross section at mid–rapidity with about five standard deviations. The same is true for the model RSZ–LTA, which is within one standard deviation from the measurement at forward rapidity, but 2–3 standard deviations from the measurement at mid–rapidity.

At mid–rapidity the measured incoherent cross section of $\mathrm{d}\sigma_{J/\psi}^{inc}/\mathrm{d}y = 0.98^{+0.19}_{-0.17}$ (stat. + syst.) mb was compared with the models LM, Starlight, and RSZ–LTA (Figure 3.14 b)). The prediction from Starlight is 60% to high, while the LM and RSZ–LTA models both underestimates the cross section in their predictions [46]. A further check was done by calculating the ratio between the incoherent and coherent cross sections.

In data this ratio was measured to be $0.41^{+0.10}_{-0.08}$ (stat. + syst.). The ratio from the models was 0.21 (LM), 0.41 (Starlight), and 0.17 (RSZ–LTA). The models RSZ–LTA and LM both underpredicts the incoherent–to–coherent cross section ratio, even though the RSZ–LTA model is quite close for the coherent cross section. Starlight does not predict either the coherent or incoherent cross sections well individually, but has about the right ratio.

At forward rapidity a further check was done by dividing the rapidity interval into two, and the ratio between the cross section in each of the intervals was computed. This will cause some of the systematic errors to cancel, and the dominant remaining error will be statistical. The result was $R = \sigma(-3.1 < y < -2.6)/\sigma(-3.6 < y < -3.1) = 1.36 \pm 0.36$ (stat.) ± 0.19 (syst.) [45]. The measured ratio was compared to the models. Two models deviated with more than one standard deviation: AB–MSTW08 (1.7 standard deviations) and AB–HKN07 (1.5 standard deviations). In summary the models which include nuclear gluon shadowing (RSZ–LTA, AB–EPS08 and AB–EPS09) was in best agreement with the measurement at forward rapidity [45].

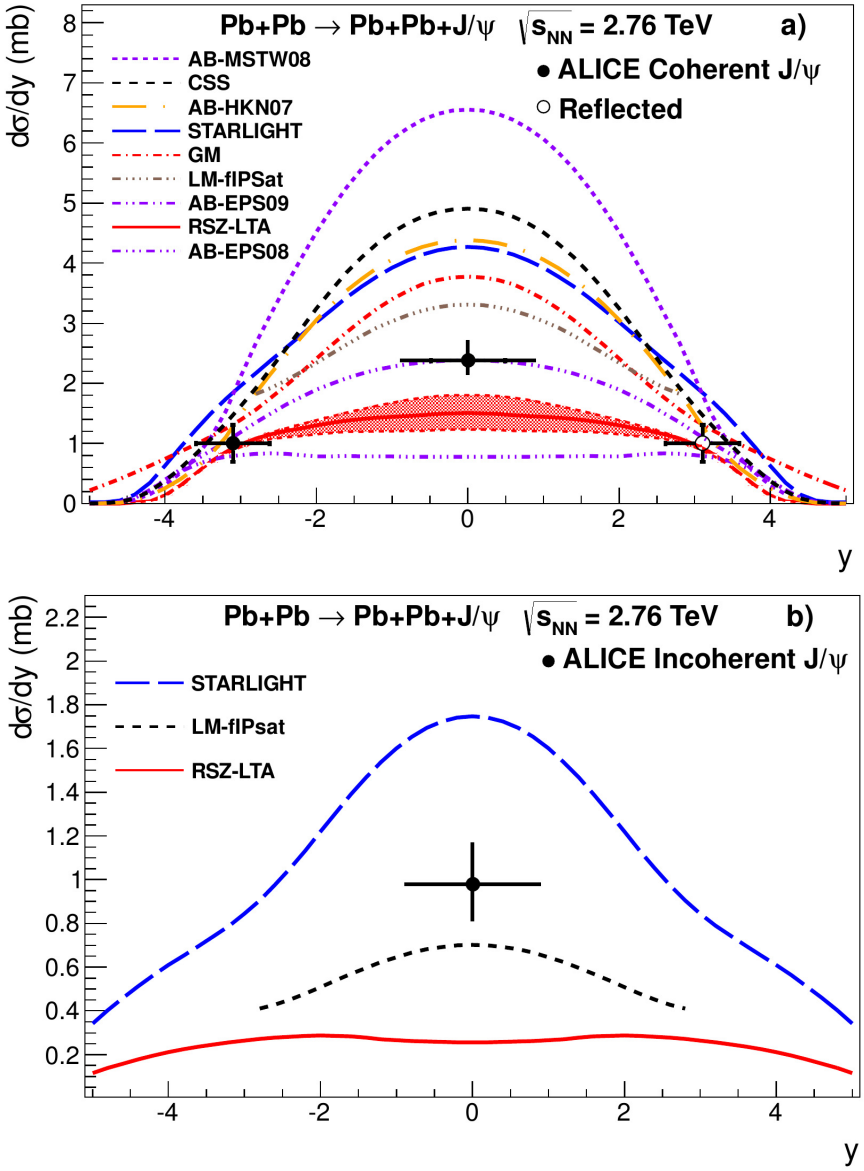

Figure 3.14: a): The measured coherent cross section for J/ψ photoproduction at mid– and forward rapidity. b):The measured incoherent cross section for J/ψ photoproduction at mid–rapidity [46].

Chapter 4

ALICE – A Large Ion Collider Experiment

ALICE is one of the four main experiments at the Large Hadron Collider. ALICE is a multi-purpose detector designed to study the physics of strongly interacting matter at extreme densities and temperatures. It is the only dedicated heavy-ion experiment at the LHC [56]. An overview of the ALICE detector is shown in Figure 4.1. Although primarily designed to study heavy–ion collisions with multiplicities of more than 1000 charged particles, it has turned out to work very well also for ultra–peripheral collisions. The ALICE experiment consists of a central barrel, a forward muon arm, and a set of smaller forward detectors.

This chapter contains a short presentation of the subdetectors in ALICE. For a full technical description see [57].

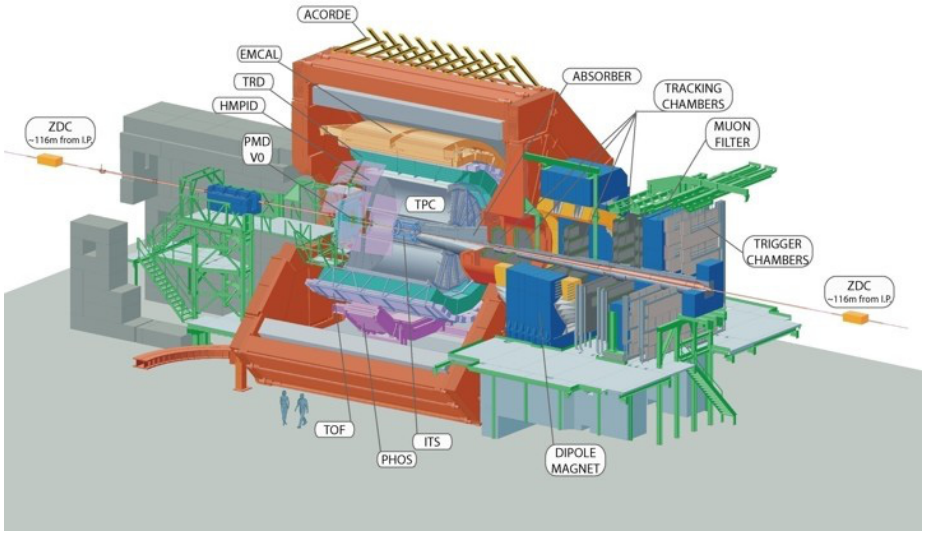

Figure 4.1: The ALICE experiment.

4.1 The central barrel detectors

The central barrel has a charged particle tracking system consisting of an Inner Tracking System (ITS) in combination with a cylindrical Time Projection Chamber (TPC). Particle identification is obtained from the energy loss in the tracking detectors alone or in combination with data from a Time–Of–Flight detector (TOF), a Transition Radiation Detector (TRD) and the High Momentum Particle Identification Detector (HMPID). In addition the central barrel contains a high resolution Photon Spectrometer (PHOS) and an Electromagnetic Calorimeter (EMCAL). The central barrel covers a pseudorapidity region $|\eta| < 0.9$. The calorimeters and HMPID have partial azimuthal coverage.

The central barrel is surrounded by the L3 magnet. The magnet, which has a diameter of 16 m and weighs 8000 tonnes, produces a magnetic field of 0.5 T, from a 30 kA current.

The central barrel is designed to handle multiplicities up to $\mathrm{d}n_{ch}/\mathrm{d}\eta = 8000$ at mid-rapidity. All charged particles with momenta (p_T) greater than 0.2 GeV/c can be reconstructed. Charged particles in the magnetic field surrounding the central barrel, will follow helical paths. Since the direction of the magnetic field is along the z–axis, they will be bent in the transverse plane (perpendicular to the z–axis). The curvature of the particles/tracks is used to determine their momenta.

The muon arm covers a pseudorapidity range $-2.5 > \eta > -4.0$. The muon arm is capable of reconstructing J/ψ and Υ vector mesons with vanishing p_T through their di-muon decay channel.

Several smaller detectors are located at forward angles. These are the Photon Multiplicity Detector (PMD), the Forward Multiplicity Detector (FMD), the T0 and VZERO detectors and the Zero–Degree Calorimeter (ZDC). Some of the detectors will be described in more detail in the following sections.

4.1.1 Inner Tracking System

The innermost tracking detector in ALICE is the Inner Tracking System (ITS) [57, 58]. The ITS is used to determine the primary vertex and secondary vertices, which is necessary for the reconstruction of heavy quark decays. It is also an important detector for particle identification of low momentum particles, and for improvement of the momentum and angle measurements of the TPC. Particles with momenta below 100 MeV/c are only measured by the ITS.

The ITS consists of six cylindrical layers of silicon detectors, placed at radii $r = 4$, 7, 15, 24, 39 and 44 cm from the beam pipe (see Figure 4.2). The layers are centred around the collision point, and measure the position with an accuracy better than 1 mm (see Table 4.1.1).

The density of particles can reach 80 particles per cm^2 close to the collision point. A Silicon Pixel Detector (SPD) have therefore been chosen for the two innermost layers, and a Silicon Drift Detector (SDD) for the two next layers. The track density will be lower in the two outer layers, below one particle per cm^2, and these consist of Silicon Strip Detectors (SSD).

The ITS has a coverage in pseudorapidity of $|\eta| < 0.9$. The first layer of the SPD has an extended pseudorapidity coverage of $|\eta| < 1.98$ to provide continuous coverage for the measurement of charged particle multiplicity together with the FMD detector.

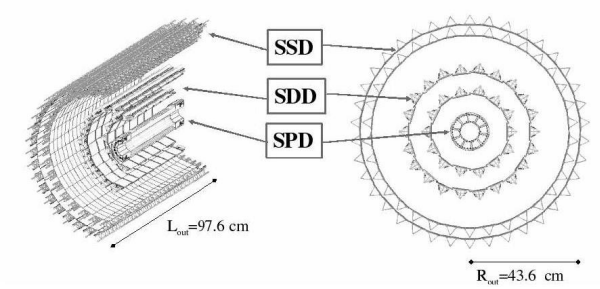

Figure 4.2: Schematic view of the ITS detector [57].

Parameter		Pixel	Drift	Strip
Spatial resolution, rϕ	[μm]	12	35	20
Spatial precision, z	[μm]	100	25	830
Two track resolution, rϕ	[μm]	100	200	300
Two track resolution, z	[μm]	850	600	2400
Cell size	[μm^2]	50×425	202×294	95 × 40000
Total number of readout channels	[k]	9835	133	2608

Table 4.1: ITS properties [57]

4.1.2 Time Projection Chamber

The Time Projection Chamber technique was first proposed by David R. Nygren [59, 60]. A TPC consist of a large volume filled with a drift gas. The end plates of the volume are equipped with a layer of multiwire proportional chambers (MWPC). Parallel electric and magnetic fields are applied over the gas volume. Electrons formed by an ionizing particle traversing the detector, will drift parallel to the **E**– and **B**–fields, towards one of the end plates The image of the ionizing track will be broadened by the transverse diffusion of electrons during the drifting. The magnetic field will reduce this effect by forcing the electrons to go in helical paths around the magnetic field. The magnetic field will also bend the paths of the ionizing particles, making it possible to measure their momentum from the curvature of the track. TPCs have previously been used by the ALEPH experiment at LEP, the STAR experiment at RHIC, and in fixed target experiments such as NA49 at SPS.

The ALICE TPC (Figure 4.3) is a cylindrical gaseous detector, with a hole through the central axis where the ITS and beam pipe is placed. The TPC has a length of 510 cm, an inner radius of 80 cm and an outer radius of 250 cm. This makes a volume of 90 m^3. This volume is filled with a 85.7% Ne, 9.5% CO_2 and 4.8% N_2 gas mixture [61, 62]. An **E**–field is set up along the z-axis, which will make the electrons drift towards the end–plates. At the end plates, which are divided in 18 sectors, MWPCs will create an avalanche of electrons in the strong field around the anode wires. The released electrons will induce a signal on the cathode plane, which is divided into pads of size 4–6 mm (ϕ–direction) and 7.5–15 mm (r–direction). The signals on the pads are amplified and digitized by the Front–End electronics and passed further to the Data

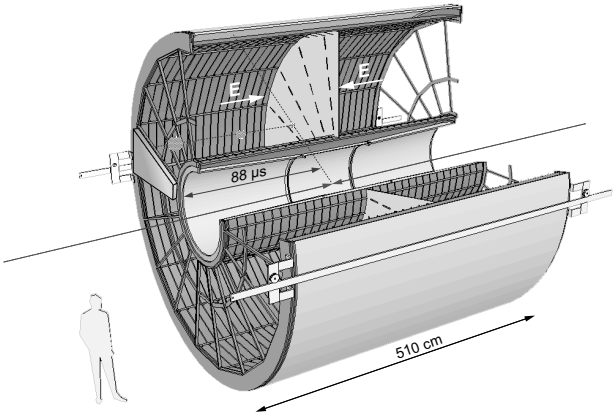

Figure 4.3: The ALICE TPC.

Acquisition system. The location of the signal on the pad plane gives the $r\phi$–position of the track. The last component, z, is given by the drift time. This gives a three dimensional measurement of the track.

The ALICE TPC [57, 62] is the main tracking device in the central barrel. It is built to give, together with the other central barrel detectors, charged particle momentum with good separation between tracks, particle identification with energy loss measurements, and vertex determination. In addition, the data is used to generate a fast online trigger with the High Level Trigger (HLT).

The TPC covers a pseudorapidity range of $-0.9 \leq \eta \leq 0.9$ and 2π in azimuthal angle. It is designed to handle multiplicities up to $\mathrm{d}n_{ch}/\mathrm{d}\eta = 8000$. The position resolution in $r\phi$ is varying from 800 μm for the inner radius, to 1100 μm for the outer radius. The resolution in the z–direction is varying from 1250–1100 μm. The dE/dx resolution is 5% for isolated tracks, and 6.8% at $\mathrm{d}n_{ch}/\mathrm{d}\eta = 8000$ [57, 61]. A p_T range from 0.1 GeV/c to 100 GeV/c is covered by the detector [57]. The momentum resolution is p_T dependent. The relative transverse momentum resolution for the TPC+ITS combined tracking is shown for $p_T < 50$ GeV/c in Figure 4.4.

4.1.3 Transition Radiation Detector

The next layer of detectors is the Transition Radiation Detector (TRD) [57, 63]. The TRD identifies electrons with momenta greater than 1 GeV/c. Transition radiation from electrons with momenta greater than 1 GeV/c, can be used to obtain the necessary pion rejection capability. Together with the data from TPC and ITS, one can study the production of vector mesons and the dielectron continuum in both pp and Pb–Pb collisions.

Since the TRD is a fast tracker, it could be used as a trigger for high momentum electrons. It can participate in the Level 1 trigger and can be used to enhance the recording of high–p_T J/ψ, Υ and jets. In the 2010 Pb–Pb run, the TRD trigger was however not in use.

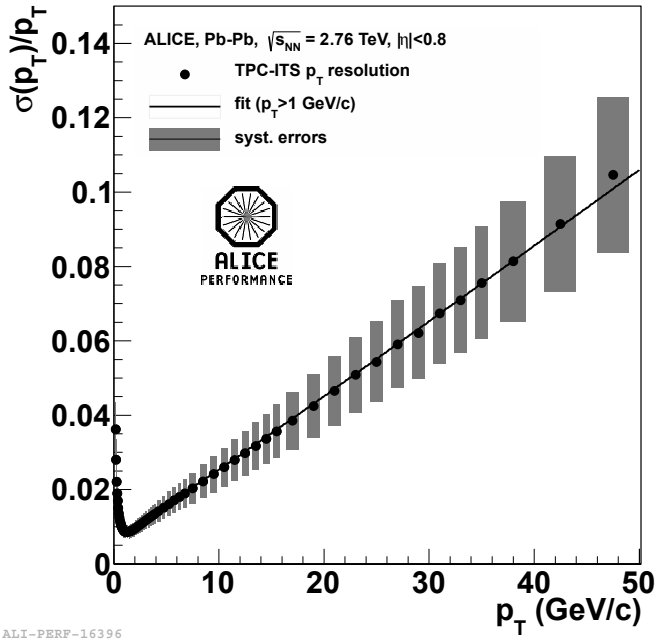

Figure 4.4: Relative transverse momentum resolution for TPC+ITS combined tracking.

4.1.4 Time–Of–Flight detector

The identification of particles in the intermediate momentum range, is done by the Time–Of–Flight detector (TOF) [57, 64]. The TOF together with the ITS and the TPC provide event–by–event identification of pions, kaons and protons. The TOF can separate kaons from pions up to 2.5 GeV/c and protons from kaons up to 4 GeV/c. In Figure 4.5 the particle separation performance of TOF is shown.

The detector covers a pseudorapidity range $|\eta| < 0.9$ and is divided into 18 sectors in the azimuthal direction (ϕ), and 5 segments in the longitudinal direction (z). This design has been adopted to match the geometry of the TPC. The whole detector is located inside a cylindrical volume with an inner radius of 370 cm and an outer radius of 399 cm.

The granularity of the TOF is given by the requirement to identify as many charged particles as possible at a charged particle density of $\mathrm{d}N_{ch}/\mathrm{d}\eta = 8000$. Simulations show that a pad size of 3.5×2.5 cm^2 gives an occupancy of 16% at the highest charged particle density, including secondary particles. The detector is built up by Multigap Resistive Plate Chamber (MRPC) strips, with and area of 122×13 cm^2. A charged particle entering an MRPC, will create ionization in the detector material. An electron from this primary ionization will gain momentum from a constant electric field, creating an avalanche effect, which induce a signal on pick–up pads close to the electrodes [65]. Each strip has 96 pads (3.7×2.5 cm^2) in two rows. The detector has about 1.6×10^6 readout channels. It can participate in the L0 trigger decision and makes use of the L1 and L2 trigger signals for readout[64].

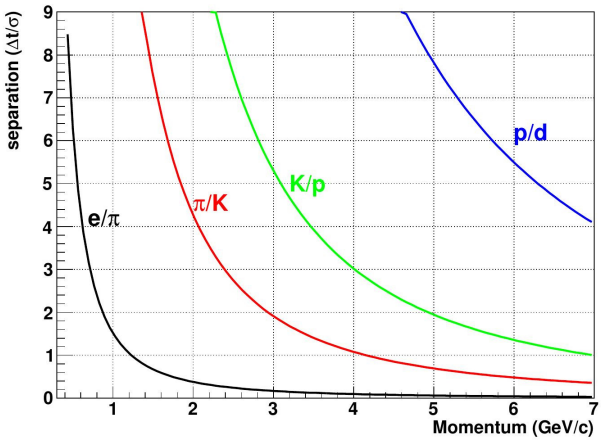

Figure 4.5: Particle separation with the TOF detector [65].

4.1.5 Calorimeters

There are two electromagnetic calorimeters in ALICE: The Photon Spectrometer (PHOS) and the Electromagnetic Calorimeter (EMCAL). Electrons, positrons and photons produce electromagnetic showers in the detector material (crystals for PHOS, lead for EMCAL), while hadrons produce showers with a different shape. One can distinguish between charged particles, photons and hadrons by combining shower shape analysis and track matching information from the tracking detectors.

The Photon Spectrometer (PHOS) [57] (Figure 4.6) is a high resolution electromagnetic calorimeter, which covers a limited range of pseudorapidity and azimuthal angle; -0.12 $\leq \eta \leq$ 0.12 and 220° $\leq \phi \leq$ 320° respectively. PHOS is divided into five independent modules, where currently three are installed. It is positioned in the bottom of ALICE at a distance 460 cm from the interaction point. Each module has a total of 3584 detection cells, which consist of a lead–tungstate crystal, coupled to an Avalanche Photo-Diode (APD), followed by a low–noise preamplifier. Scintillation photons from atoms excited by the shower will go through the crystals and make a signal in the photodetectors attached to each crystal. The main physics objectives are the analysis of thermal and dynamical properties of the initial phase of the collision extracted from low–p_t direct photons and the study of jet quenching through the measurement of high–p_T π^0 and η spectrum and γ–jet correlations.

The Electromagnetic Calorimeter (EMCAL)[57] (Figure 4.7) is a Pb-Scintillator sampling calorimeter. It is located $\sim$ 4.5 m from the interaction point. The detector covers a pseudorapidity range of -0.7 $\leq \eta \leq$ 0.7 and an azimuthal angle of $\Delta\phi = 107°$, and is placed approximately opposite to PHOS in azimuth. The EMCAL is important for jet physics in ALICE. The detector also measures the neutral component of the jet. In combination with the TPC, EMCAL has good jet energy resolution in Pb–Pb collisions, and sensitivity to the full range of jet– quenching effects expected at the LHC.

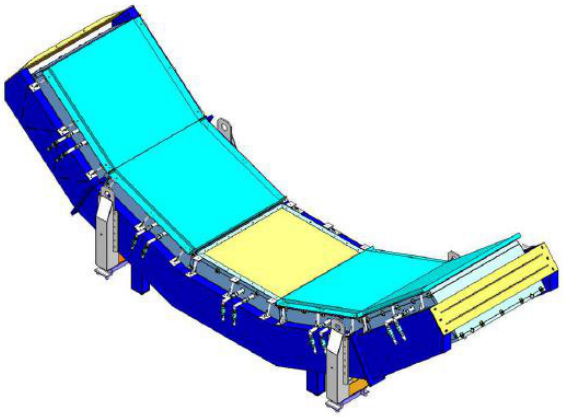

Figure 4.6: The PHOS detector [57].

4.2 Muon spectrometer

The muon spectrometer [57] is shown in Figure 4.8. The spectrometer consists of a passive front absorber; a tracking system; a dipole magnet; a passive muon filter wall, followed by four planes of trigger chambers; an inner beam shield to protect the chambers from primary and secondary particles, produced at large rapidities. The angular acceptance is $-4.0 < \eta < -2.5$.

The 4 m long front absorber, with a fiducial volume of concrete and carbon, is located inside the solenoid magnet. The front absorber is there to prevent hadrons from entering the spectrometer, and it is designed to limit small angle scattering and energy loss by traversing muons, in addition to protect other detectors from secondary particles produced in the absorber itself. A dense absorber of tungsten, lead and stainless steel is surrounding the beam pipe, to shield the spectrometer. An 1.2 m thick iron muon filter is placed after the last tracking chamber, in front of the trigger chambers, to give additional protection for the trigger chambers. The front absorber and the muon filter stop muons with $p < 4.0$ GeV/c.

The tracking chambers consist of cathode pad chambers, arranged in five stations. Each station has two chambers. Two of the stations are placed before the dipole magnet, one is placed inside, and two after the magnet. The tracking system covers a total area of $\sim$100 m^2. It was designed to achieve a spatial resolution of 100 μm, and can operate at the maximum hit density of about 5×10^{-2} cm^{-2} expected in central Pb+Pb collisions.

To provide two–dimensional hit information each of the chambers has two cathode planes. The first station is placed right behind the absorber to provide precise measurements of the exit points. A fine–granularity segmentation of the read–out pads is needed to keep the occupancy low. Since the hit density is higher close to the beam pipe the pads are smallest here, and the pads are larger at larger radii. The total number

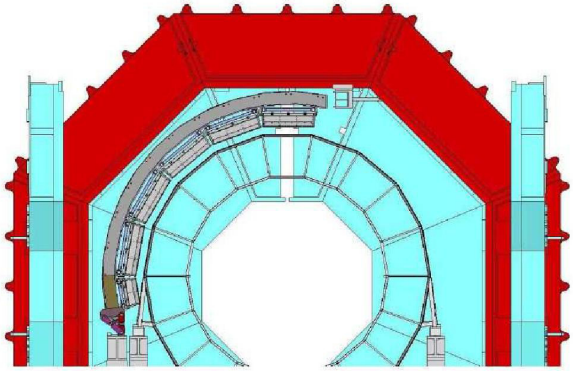

Figure 4.7: The EMCAL in ALICE [57].

of channels is about one million.

In the trigger system two programmable cuts (low–p_T and high–p_T) are performed in parallel by the trigger electronics. The p_T thresholds can vary from ∼0.5 GeV/c to ∼2.0 GeV/c. Less than 800 ns after the interaction the following six trigger signals are delivered to the ALICE Central Trigger Processor (CTP): at least one single muon track above either the low– or high–p_T cut; at least two unlike–sign muon tracks above either the low– or high–p_T cut; at least two like–sign muon tracks above either low– or high–p_T cut.

The space resolution for the trigger detector is required to be better than 1 cm to perform the correct p_T selection. Resistive Plate Chambers (RPCs) are used to achieve this resolution. The trigger system has two stations with two RPC planes in each. The stations are placed one meter apart from each other, behind the muon filter. Each plane consists of 18 RPC modules with a total active area of about 140 m^2.

Quantity	Value
Muon detection	
Polar angle coverage	$171^\circ \leq \theta \leq 178^\circ$
Azimuthal angle coverage	360°
Minimum muon momentum	4 GeV/c
Pseudorapidity coverage	$-4.0 < \eta < -2.5$

Table 4.2: Muon detection capabilities of the muon spectrometer [57].

4.3 Forward detectors

4.3.1 The VZERO detectors

The VZERO detectors [57] are two arrays of scintillator detectors located at each side of the interaction point (VZERO–A and VZERO–C). VZERO–A is located 329 cm

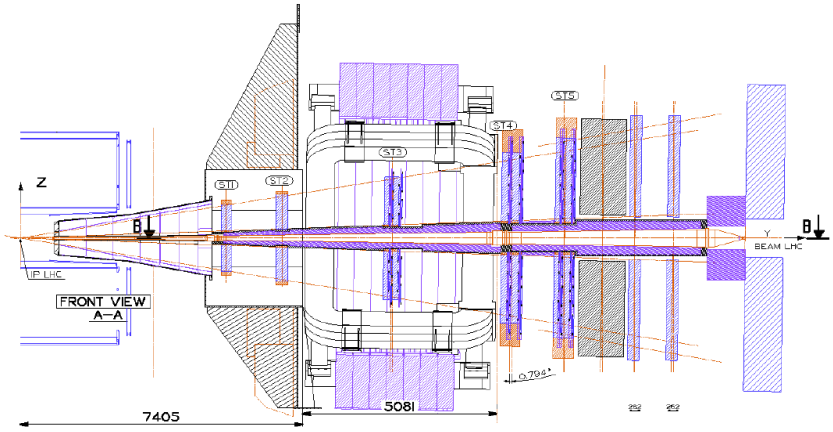

Figure 4.8: The muon spectrometer longitudinal section [57].

from the center of the interaction region on the opposite side of the muon spectrometer and covers the pseudorapidity rage $2.8 < \eta < 5.1$. VZERO–C is located 87 cm from the interaction region on the same side as the muon spectrometer and covers $-3.7 < \eta < -1.7$. They are segmented into 32 individual counters, distributed in four rings (Table 4.3.1).

Ring	**V0A** η_{max}/η_{min}	**V0C** η_{max}/η_{min}
0	5.1/4.5	-3.7/-3.2
1	4.5/3.9	-3.2/-2.7
2	3.9/3.4	-2.7/-2.2
3	3.4/2.8	-2.2/-1.7

Table 4.3: Pseudorapidity acceptance of the rings of VZERO–A and VZERO–C [57].

The VZERO detectors are used to provide a minimum–bias Level 0 trigger for both pp and Pb–Pb collisions. The particles that trigger the detector can be both primary and secondary, but since the dependence of the numbers of particles hitting the VZERO and and the number of emitted particles is monotone, the VZERO detectors is used to indicate the centrality of the collision. Cuts on the number of fired counters and on the total charge can be used for centrality triggers [57]. For ultra–peripheral collisions the VZERO detectors are used as veto detectors and are required to be empty to suppress hadronic interactions.

4.3.2 Zero–Degree Calorimeter

In ALICE two sets of Zero–Degree Calorimeters (ZDCs) [57] are located 116 m on each side of the interaction point. These are hadron calorimeters. In addition two sets

of electromagnetic calorimeters (ZEM) are placed on each side of the beam pipe, about 7 m from the interaction point. Spectator protons are separated from neutrons by the magnetic elements of the LHC beam line. Therefore each ZDC is made by to different detectors, one for protons (ZP) and one for neutrons (ZN). A schematic view of the ALICE beam line with the ZDCs is shown in Figure 4.9, and a front view of the ZDC is shown in Figure 4.10. For details and characteristics of the ZDC detectors see table 4.3.2.

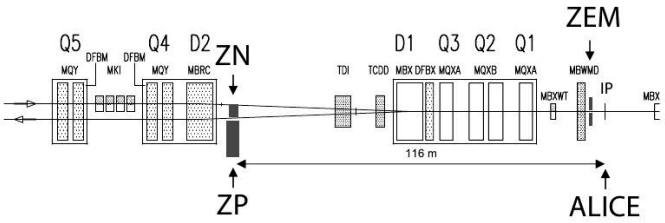

Figure 4.9: Schematic view of the ALICE beam line opposite to the muon arm. The ZDCs for protons (ZP), neutrons (ZN) and the electromagnetic calorimeters (ZEM) are shown [57].

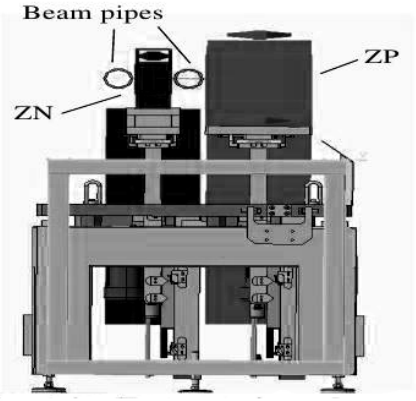

Figure 4.10: Front view of the ZDC[57].

	ZN	ZP	ZEM
Dimensions (cm^3)	7.04×7.04×100	12×22.4×150	7×7×20.4
Absorber	tungsten alloy	brass	lead
$\rho_{absorber}$ (g cm^{-3})	17.6	8.5	11.3
Length (In X_0 units)	251	100	35.4
Length (In λ_I units)	8.7	8.2	1.1
Number of PMTs	5	5	1

Table 4.4: Dimensions and main characteristics of the ZDC [57].

One can estimate the number of participant nucleons in an A–A collision by measuring the energy carried in the forward direction by spectator nucleons. The number of participants is directly related to the geometry of the collision. In ALICE the number of spectators is detected by the ZDCs. If it had been possible to detect all spectators, the number of participants would have been given by [57]:

$$N_{spectators} = \frac{E_{ZDC}(TeV)}{E_{nucleon}(TeV)}$$

$$N_{particpants} = A - N_{spectators}$$

Here $E_{nucleon}$ is the energy per nucleon in the lead beam at the LHC. In a collider, however, it is not possible to use such a simple estimate since many are bound in heavier fragments, which do not reach the ZDCs. The centrality information from ZDC may be used to trigger at Level 1 (L1). The ZDCs can also be used to study neutrons emitted following electromagnetic excitation in ultra–peripheral collisions.

4.3.3 Forward Multiplicity Detector

The main purpose of Forward Multiplicity Detector (FMD)[57] is to measure the charged particle multiplicity in the pseudorapidity ranges -3.4 $< \eta <$ -1.7 and 1.7 $< \eta <$ 5.0. There is an overlap in the pseudorapidity coverage between FMD and the ITS pixel detector (SPD).

FMD consists of three rings, FMD1, FMD2 and FMD3. FMD2 and FMD3 each consists of and inner and an outer ring of silicon sensors and are located on either side of the ITS detector. FMD1 was placed further from the interaction point to extend the charged particle multiplicity coverage.

The inner rings consists of 10 silicon sensors, and the outer rings of 20 silicon sensors. The beam pipe constraints the inner radius of the rings, while the TPC inner radius constraints the outer radius of the rings. The inner sensors consist of two azimuthal sectors, each with 512 silicon strips. The outer sensors also consist of two sectors, but with 256 sensors each. Each ring has a total of 10,240 silicon strips, giving the FMD a total of 51,200 strips.

4.4 Trigger system

By design there are four trigger levels in ALICE: Level 0 (L0), Level 1 (L1), Level 2 (L2) and the High Level Trigger (HLT).

The trigger logic is handled by the Central Trigger Processor (CTP), which combines the information from the trigger input detectors and sends trigger signals to read out the subdetectors. To fit the detector requirements, fast first response from the triggers is needed. The tracking detectors has to deal with the high multiplicities in Pb–Pb collisions. For some detectors this has led to the use of non-pipelined 'track–and–hold' electronics, and these require a strobe at 1.2 μs. The fast part of the trigger is split into L0 and L1 to achieve this. The L0 signal reaches the detectors after 1.2 μs, but this is to fast for some of the trigger inputs. Therefore there is in addition a L1 signal arriving after 6.5 μs.

The hight multiplicities of Pb–Pb collisions in ALICE make events containing more than one central collision unreconstructable. Because of this, past–future protection can be implemented in the L2 triggers. The L2 trigger waits for the end of the past–future interval (88 μs) to verify that the event can be recorded. The L2 trigger can also be used for running more advanced trigger algorithms. The trigger latencies associated with the L0, L1 and L2 triggers are listed in Table 4.5

Signal status	L0 [μs]	L1 [μs]	L2 [μs]
Last trigger input at CTP	0.8	6.1	87.6
Trigger output at CTP	0.9	6.2	87.7
Trigger output at detector	1.2	6.5	88.0

Table 4.5: Latencies associated with the different trigger levels at the CTP [66].

During the 2010 Pb–Pb run, the triggers used consisted of logical combinations of L0 inputs. No selection at the L1, L2, or HLT level was done.

4.4.1 Trigger inputs

The ALICE trigger system [57] has 24 L0 inputs, 24 L1 inputs and 12 L2 inputs. The L0 inputs active in the 2010 Pb–run are listed in Table 4.6 and the L1 inputs in table 4.7. The trigger input detectors used for the UPC analysis in this thesis are TOF, SPD and VZERO.

The VZERO detector has four different basic signals, which corresponds to hits on either side of the interaction region in the time windows for beam–gas and beam interactions. The SPD also provides L0 trigger signals.There are several inputs for SPD triggers. In addition to simple multiplicity requirements, other signals, such as triggers with cuts on the event topology can be implemented. For example a trigger for ultra–peripheral collisions requiring that the two SPD hits are back–to–back was used during the 2013 p–Pb run.

For the triggers for ultra-peripheral collisions in the 2010 Pb–Pb run, four different trigger inputs were used: 0OM2, 0SM2, 0VBA and 0VBC. The 0SM2 input requires at least two fired chips in the outer layer of the SPD detector, while the 0OM2 trigger requires hits in at least two pads of the TOF detector. The 0VBA and 0VBC are VZERO beam–beam triggers for the A–side and C–side, requiring a hit in the VZERO–A or VZERO–C respectively. The threshold for a hit is set to about the mean energy deposited by a minimum ionizing particle [67].

4.4.2 Clusters and classes

A trigger class [57, 70] is a set of logical conditions demanded for the L0 inputs, the set of detectors required for read–out, past–future protection requirements, handling of Region–of–Interest data and handling of rare triggers.

The trigger classes define how CTP inputs are configured, and trigger clusters how CTP outputs are configured. A trigger class defines which trigger detectors that are used to trigger one kind of event, while a trigger cluster defines which detectors that

No.	Code	Detector	Description
1	0SMB	SPD	SPD minimum bias single
2	0VBA	VZERO	beam–beam A–side
3	0VBC	VZERO	beam–beam C–side
4	0BPA	BPX	bptx A–side
5	0BPC	BPX	bptx C–side
6	0MUL	MTR	Di-muon unlike low p_T
7	0MSL	MTR	Di–muon single
8	0MLL	MTR	Di–muon like low p_T
9	0MUH	MTR	Di–muon unlike high p_T
10	0SM5	SPD	At least five hits in SPD
11	0SM1	SPD	At least one hit in SPD
12	0SCO	SPD	SPD cosmic
13	0SM2	SPD	At least two hits in SPD
14	0SMH	SPD	SPD high multiplicity
15	0LSR	Laser	Hardware calibration trigger
16	0OM2	TOF	Two or more hits in TOF
17	0OUP	TOF	TOF ultra–peripheral
18	0OM3	TOF	Three or more hits in TOF
19	0VBK	VZERO	VZERO background
20	0TCE	T0	T0 central
21	0TSC	T0	T0 semi–central
22	0EMC	EmCal	EmCal level 0
23	0PH0	PHOS	PHOS level 0

Table 4.6: L0 trigger inputs which were active during the 2010 Pb+Pb run [68, 69].

should be read–out. The total number of classes can be 50, while there is a maximum of six clusters. The name of a trigger class is divided in five elements separated by a dash (–) [71]:

- The first element is a *descriptor* of the trigger inputs.
- The second element is a *bunch crossing mask*, which defines in which orbit the trigger is active. This can be *B* (beam from both sides), *A* (beam from the A–side),*C* (beam from the C–side), or *E* (empty).
- The third element gives the *past–future protection scheme* for the class. It defines the conditions for the bunch crossings preceding or following the trigger. For all runs in this analysis recorded during the 2010 Pb–Pb run, this was *NOPF*, i.e. past–future protection was not applied.
- The fourth element gives the *detector cluster* to be read–out.
- The fifth optional element is a *rare flag*. Special time intervals are reserved for triggers defined as rare. The presence of the letter R in the end of the class name indicates that it is a rare trigger.

No.	Code	Detector	Description
1	1EJE	EmCal	Jet trigger
2	1EGA	EmCal	Gamma trigger
3	1PHL	PHOS	
4	1PHM	PHOS	
5	1PHH	PHOS	
6	1HCO	TRD	TRD cosmic trigger
7	1ZMD	ZDC	
8	1ZMB	ZDC	
9	1ZED	ZDC	
10	1ZSD	ZDC	

Table 4.7: L1 trigger inputs which were active, although not used for selecting events, during the 2010 Pb+Pb run [68, 69].

A generic name will be as follows:
C[*descriptor code*]–[*bunch crossing mask code*]–[*past–future protection code*]–[*detector cluster code*]–[*rare flag*]. An example is C0SMH–B–NOPF–ALL–R, which has the descriptor D0SMH, bunch crossing mask code B, past–future protection code NOPF, cluster code ALL and the rare flag.

The descriptor is defined by a logical function of input codes. Input codes has the form n[*3–char code*].For single input descriptors, *n* indicates the trigger level. The second character tells which detector the input is from. E.g. 0SMH means "level 0 input SPD high multiplicity. A descriptor code starts with the letter D and and have a minimum of five characters. E.g. DVBAND, which is the descriptor code for the logical AND for the V0A and V0C detectors. If the descriptor is defined by a single trigger input, the code is simply the letter D followed by the trigger input code. E.g. D0SMH which is a descriptor corresponding to the single input 0SMH, or D0OM2 which corresponds to the input 0OM2, which is at least two hits in the TOF detector. Use of digits as the second character is reserved for such single input descriptors.

The detector cluster code tells which detectors that are read out when the trigger class is fired. ALL indicates that all ALICE detectors are read out.

Trigger class	Description	L0 Combination
C0SMH–B–NOPF–ALL	SPD high multiplicity	0SMH
C0OM2–B–NOPF–ALL	Two or more hits in TOF	0OM2
CMBS2A–B–NOPF–ALL		0SM2 & 0VBA
CMBS2C–B–NOPF–ALL		0SM2 & 0VBC
CMBAC–B–NOPF–ALL		0VBA & 0VBC
C0SMB–B–NOPF–ALL	SPD minimum bias single	0SMB
C0SM5–B–NOPF–ALL		0SM5

Table 4.8: Some trigger classes from the first part of the 2010 Pb+Pb run [68].

Each trigger class has six counters, L0b, L0a, L1b, L1a, L2b and L2a, where *b* and *a* stand for before and after. L0b gives the number of times a trigger class is counted,

Trigger class	Description	L0 Combinations
C0SMH–B–NOPF–ALL	SPD high multiplicity	0SMH
CMBACS2–B–NOPF–ALL	Minimum bias	0SM2 & 0VBA & 0VBC
C0SMB–B–NOPF–ALL	SPD minimum bias single	0SMB
C0MSL–B–NOPF–ALL	Di–muon single	0SML
CMUP1–B–NOPF–ALL	Di–muon ultra–peripheral	
CCUP2–B–NOPF–ALL	Central barrel ultra–peripheral	0SM2 & 0OM2 & !0VBA & !0VBC

Table 4.9: Some trigger classes from the last part of the 2010 Pb+Pb run [68].

and L2a gives the number of times the same trigger class passes the CTP and detector dead–time, and other possible vetos like downscaling. In the 2010 Pb+Pb run, all L0 triggers went through L1 and L2 without any cuts.

Table 4.8 and Table 4.9 list some of the trigger classes which were active during the early and the late part of the 2010 Pb-Pb run, respectively. The analysis presented in the following chapters is based on the 0OM2, CCUP2, and 0SM2 triggers. In the first part of the data taking period, when the luminosity was low, a trigger which required at least two hits in the TOF detector was used. This is the C0OM2 trigger class. Later in the data taking period, when the luminosity was higher, a stricter trigger definition was needed. Therefore a trigger which required at least two hits in the TOF detector, at least two hits in the Si–pixel detectors and a veto in the VZERO counters was implemented and used for the last part of the run. This trigger was named CCUP2.

4.5 High Level Trigger (HLT)

The collision rate in ALICE can be of the order of 200 Hz for central collisions. The TPC alone can produce 15 GB/s of data, but one can only write $\sim$1.5 GB/s to disk. The purpose of the High Level Trigger (HLT) [72] is to reduce the data rate with at least one order of magnitude, while using the full luminosity. The main tasks of the HLT can be summarized in three points:

- **Trigger** on events based on a detailed online analysis of the physics observables.
- **Select** relevant parts of the events, or regions of interest.
- **Compress** the parts of the event which is read out and reduce the recording rate as much as possible without losing important physics.

The processing hierarchy of HLT is shown in Figure 4.11. The raw data from the ALICE detectors is received through 454 DDLs in layer one. In layer two the basic calibration is performed, and hits and clusters are extracted. In the third layer the event is reconstructed for each detector individually, before the next layer combines the processed and calibrated information to a complete event. Using the reconstructed physics observables the selection of events or region of interest is performed in layer 5, based on run specific selection criteria. The selected data is further subjected to complex data compression algorithms.

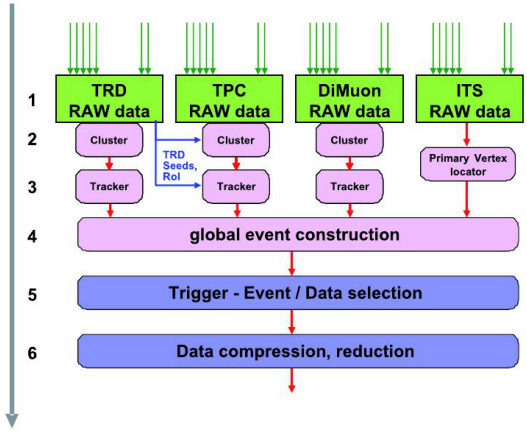

Figure 4.11: Architectural overview of the High–Level Trigger [57].

During the 2011 Pb–Pb run ESDs produced by HLT was used to check the functionality of the UPC triggers before the offline reconstruction was available.

4.6 Data Acquistion System (DAQ)

The ALICE Data Acquistion System (DAQ) [66] takes care of the collection of data from the subdetectors, building the events and transporting the data to storage.

All the subdetectors use the same protocol for data transfer, the Detector Data Link (DDL). The data is collected from the detectors though the DDL cables and transferred to a Local Data Consentrator (LDC), which perform subevent building. From the LDC the data is transferred, via the Event Building Network, to a Global Data Consentrator (GDC). In the GDC the final event building from all detectors, according to trigger class, is done.

The DAQ system has three modes of operation:

- **DAQ only – HLT disabled**
  This mode is the initial mode of operation. DAQ falls back to this mode if the HLT is not running.

- **DAQ + HLT analysis**
  In this mode the HLT is active, but not enabled to trigger or modify the data. It may though, add data to the events. The purpose of this mode is to be able to check the HLT algorithms.

- **DAQ + HLT enabled**
  In this mode the HLT is enabled and fully operational. It can reject and accept events, and also modify them.

4.7 Detector Control System (DCS)

The ALICE Detector Control System (DCS) [57, 66] takes care of controlling and monitoring of the experimental equipment, such as cooling systems, power supplies and front–end electronics.

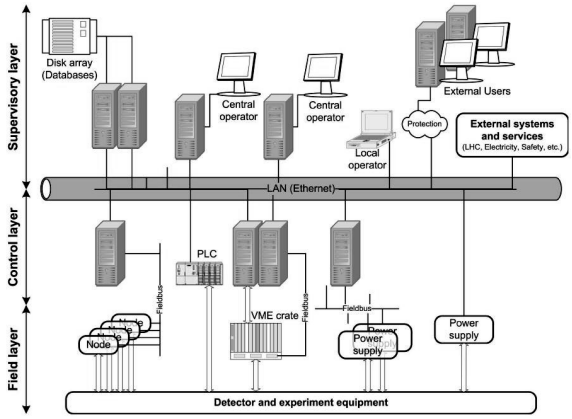

Figure 4.12: Architectural overview of the Detector Control System [57].

The DCS hardware architecture is divided in three layers, as can be seen in Figure 4.12. The top layer is the supervisory layer. This layer consists of computers with a user interfaces for the operator, who controls and monitors the system. The supervisory layer communicate with the control layer which consists of worker nodes, PLCs and PLC–like devices, which interface the experimental equipment. The control layer communicate with the field layer, and make the information from this layer available for the supervisory layer. At the same time it receives commands from the supervisory layer and distribute it to the field layer. The field layer consists of devices like power supplies, front–end electronics, cooling systems, sensors etc. The software architecture of DCS is a tree structure of nodes representing subdetectors, their subsystems and devices. Each node in the tree has a single parent, except for the top node. Nodes may have zero, one or more children. There are three type of nodes; Control Units (CU), Logical Units (LU) and Device Units (DU). The CUs and LUs model and control the subtree below, and the DUs drives a device. The software hierarchy is shown in Figure 4.13.

The functionality of each unit in the tree is modelled and implemented as a Finite State Machine (FSM). The object to be modelled by an FSM is thought of as having a set of stable states. It can transit between the states by executing so called actions triggered by the operator, other components or events such as state changes or some value going over a threshold. There are two types of objects in the FSM: Abstract object, represented by LUs or CUs, and physical objects represented by DUs in the tree. The core software in the control system is PVSS–II (Prozessvisualisierungs- und Steuerungssystem – Process visualization and control system), which is a commercial SCADA (Supervisory Control and Data Acquistion) system. PVSS–II is used by all

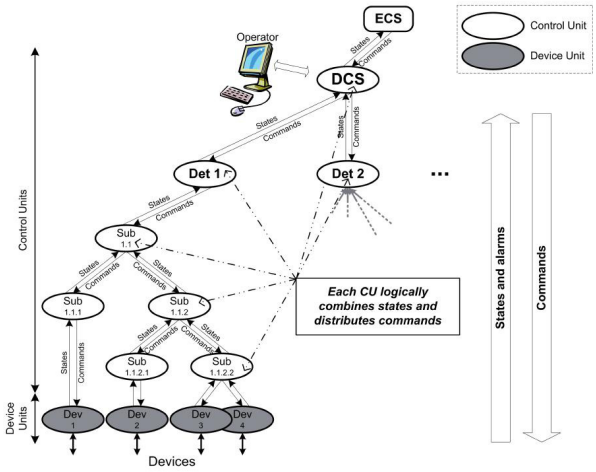

Figure 4.13: DCS software hierarchy [57].

four LHC experiments. Around the PVSS–II software CERN has built a framework called the JCOP–framework (Joint Control Project). The JCOP–frame work provides tools and components for implementation of common tasks that are expected from the control system, such as FSM, databases, access control, basic user interfaces etc. It also provides interfaces to several hardware devices that are commonly used by the LHC experiments.

Chapter 5

Data Analysis

In this chapter the data analysis is described starting with how the events are reconstructed, and continuing with the event selection criteria, the particle identification, luminosity estimate, and a description of the correction for acceptance and efficiency.

5.1 Event reconstruction

The raw data collected by the ALICE experiment are stored on magnetic tapes at the Tier–0 computing center, located at CERN. To store the data safely, it is shared to large regional Tier–1 computing centres around the world. The initial cluster finding and tracking is done on the Tier–0 center, while additional calibration and verification can be done also at the Tier–1 centres [73].

The digitised signal (ADC count) obtained by a sensitive pad in a detector at a certain time is called a digit. A set of adjacent digits in space and time, that are assumed to be generated by the same particle, is called a cluster. From the center of gravity of the cluster a space point were the particle crossed the detector element is reconstructed. The cluster finding is done for each detector separately. A detector specific cluster finding procedure is used for each detector to reconstruct the space points, and their uncertainty. This information is then passed on for track reconstruction. Detectors like the ITS and the TPC are able to measure the produced ionization, which can be used for particle identification. In the calorimeters, the energies of the particles are measured by measuring the total energy of the cluster.

The track finding [57] starts with the vertex reconstruction, using information from hits in the two layers of the SPD. Pairs of reconstructed points in the two layers, which are close in azimuthal angle in the transverse plane, are selected. A linear extrapolation is then used to reconstruct the z–position of the vertex from the z–coordinates of the space points. A similar procedure is done in the transverse plane to determine the x– and y–positions of the vertex.

The further track reconstruction is based on the Kalman filter approach. The tracking starts with seed values for the track parameters, obtained from the reconstructed space points in the TPC. In the first tracking pass the primary vertex is used as a constraint on the track, while secondary tracks are found in the second pass. The tracking starts by combining space points from the pad rows in the outermost part of the TPC. This combination provides a calculated track position inn the neighbouring pad row, and if a matching space point is found in that pad row, it is added to the track and the

track parameters are updated. From each seed the track is followed towards the center of the TPC, until it reaches the outermost layer of the ITS. Both track samples, with and without vertex constraints, are then propagated to the outer layers of the ITS, starting with the track with the highest momentum. If more than one cluster is found in the prolongation of the track, each assignment is followed to the innermost ITS layer. Based on the χ^2, a decision for the best track is made in the end. The process is then reversed, starting from the innermost layers of the ITS, each track using the parameters from the inwards tracking, is followed to the outermost part of the TPC. This procedure, called refitting, leads to higher precision and wrongly assigned space points are removed from the track. When the end of the TPC is reached the track is propagated further to the TRD, and matched with space points in the TOF and HMPID. In the end the tracks are refitted one more time, by reversing the process again.

The output of the reconstruction is Event Summary Data (ESD), which contains the reconstructed particle tracks, information about particle identification, vertex position, clusters reconstructed in the calorimeters, trigger information etc [57, 74].

The physics analysis starts from the ESDs created in the reconstruction. From the ESDs Analysis Object Data (AOD) can be created, to be used for further analysis, but in this work the analysis is done directly on the ESDs.

In ALICE several passes of reconstruction is done. In the first pass, pass1, high–precision alignment and calibration data, and the first set of ESD and AOD, is produced. For the second pass, pass2, the feedback from pass1 is used to tune the code, and to reconstruct tracks not coming from the primary vertex.

5.2 Analysis software

AliRoot [75] is the analysis framework for the ALICE experiment, written in C++. It is based on the software packages ROOT [76] and GEANT [77, 78]. AliRoot is used for event reconstruction, physics analysis, and simulation in ALICE.

ROOT is an object oriented software framework for high energy physics and provides a basic set of features and tools. It has the capability of handling and analyse large amount of data. It includes histogramming, curve fitting, function evaluation, minimization, graphics and visualization classes. It is possible to run macros without compilation, using the CINT C++ interpreter. The built in C++ complier can be used, if better performance is needed.

Data from root can be saved in different data structures. One such data structure is a TTree. A TTree can have several nodes called branches (of class TBranch), where each branch can store several variables. Variables on a TBranch are called leafs (of class TLeaf). A TTree can hold any kind of data, such as object, arrays or simple types.

GEANT is a toolkit that describes the passage of elementary particles through matter. It was originally designed for high energy physics, but is today also used in medical and biological sciences, radioprotection and astronautics.GEANT simulates the energy loss and possible interactions of particles as they are tracked through the detector material. This information provides the basis for the simulation of the detector response. It includes simulation of electromagnetic, hadronic and optical processes, over an energy ranges starting from 250 eV up to the TeV scale. It can handle the interactions of a set of elementary particles with a variety of materials and elements.

5.3 ALICE computing and The Grid

The large data amounts produced by ALICE require huge computing power for analysis and data storage in the order of petabytes to store the raw and analysed data. ALICE makes use of the grid platform to distribute and analyse all raw and Monte Carlo data among the 88 grid sites that participate in the ALICE collaboration [79].

The Worldwide LHC Computing Grid (WLCG) is built up by so called "Tiers" around the world. Each Tier can consist of several computing centres. There are four levels of tiers: 0, 1, 2, and 3. The Tier–0 is the CERN Data Center, which provides 20% of the Grid's total computing capacity. The Tier–0 is responsible for safe storage of the raw data from the LHC experiments, and performs the first reconstruction pass. The raw data and reconstructed output is then distributed to the Tier–1 centres. Seven of the eleven Tier–1 centres are located in Europe, three in North–America (USA and Canada), and one in Taipei, Taiwan. Each center is responsible for storage of a proportional share of the raw and reconstructed data. The Tier–1 centres also performs large scale reprocessing of the data, and stores the corresponding output, and distribute data to the Tier–2 centres. The Tier–2 centres are usually located at universities and other scientific institutions, and handle analysis requirements and do a proportional share of production and reconstruction of simulated events. There are currently 140 Tier–2 centres all over the world, where one is partly located in Bergen. Local computing resources, such as a cluster or even just an individual PC, are sometimes referred to as Tier–3 centres. These have no formal connection to the WLCG.

Grid middleware distributions are large software systems, which include a set of components providing a basic functionality, including, job management, storage management, authentication and authorization, and resource monitoring.

AliEn [80] is a set of middleware tools and services that implement a grid infrastructure used in ALICE. AliEn can be used not only as a standalone Grid, but also in collaboration with existing grids [81]. Since 2005, AliEn has been used both for data production and end–user analysis. The basic AliEn components are as follows:

- File catalogue with metadata capabilities.
- Data management tools for data transfers and storage.
- Authentication and authorization.
- Workload management system.
- Interfaces to other grid implementations.
- ROOT interface.
- Monitoring.

5.4 Data analysis on The Grid with AliEn

The analysis framework in AliRoot makes it possible for users to analyse large data sets. The analysis is done with so called analysis tasks. There are two ways of doing the analysis; in scheduled analysis trains, centrally at CERN, or end–user analysis

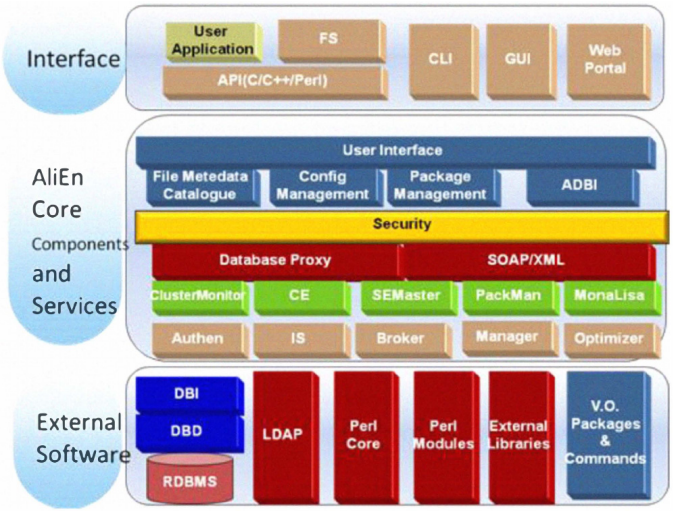

Figure 5.1: The Grid architecture for the ALICE experiment [79].

using The Grid. In analysis trains, several analysis tasks are grouped together to run simultaneously. The advantage is that each event is read and the analysis algorithms applied to it only once [57].

An analysis task is a C++ class used to do analysis in AliRoot. The user's analysis task inherits from a base analysis task, e.g. AliAnalysisTaskSE. It must have some basic functions: Constructor, UserCreateOutputObjects(), UserExec() and Terminate().

AliAnalysisTaskUPC is the analysis task which does the analysis of UPC collision data on The Grid. The output of the task is a TTree, which contains event and track information for the selected events. The output from the analysis task, is subject to further analysis on a local workstation or PC. In addition to the TTree a few histograms, containing information on triggers, cuts, etc., are created by the analysis task.

5.5 Analysis of reconstructed data

5.5.1 Standard track cuts

The cuts on the individual tracks are defined in the class AliESDtrackCuts in AliRoot. The cuts for this analysis is the standard ITS + TPC tracks cuts for 2010. The requirements for a track to be accepted are:

- At least 70 clusters in the TPC.
- The χ^2 per cluster for a TPC track must be lower than 4.
- Not have kink daughters.
- Requires ITS and TPC refit.

- There must be at least one hit in one of the SPD layers of the ITS.
- The maximum DCA to vertex is set to $DCA_L \leq 2$ cm in the longitudinal direction. In the transverse plane orthogonal to the beam direction a p_T dependent DCA cut was applied: $DCA_T \leq 0.0182 + 0.0350 \cdot p_T^{1.01}$ cm, where p_T is in GeV/c.
- The χ^2 per cluster for an ITS track must be lower that 36.

These cuts have been developed jointly in the collaboration, and are applied to the analyses in ALICE using primary tracks.

5.5.2 Event selection

Based on the characteristics of an UPC event, a set of cuts were applied to the data:

- The events were required to satisfy one of the two UPC triggers (C0OM2 or CCUP2), at hardware level.
- There must be exactly two accepted ITS+TPC tracks. The requirements for a track to be accepted are described in subsection 5.5.1.
- The event must have a reconstructed primary vertex, where the z–position of this vertex is within 10 cm from the central interaction region of the detector. The distribution of the vertex position from data is shown in Figure 5.2.
- The VZERO detectors on both the A–side and the C–side should be empty, to define rapidity gaps.
- To identify pions the energy loss of the particle in TPC was used. In the next section the particle identification method is described in detail.
- The rapidity of the mother particle is required to be $|y| < 0.5$. This is to avoid edge effect.
- The transverse momentum of the mother particle is required to be below $p_T^{pair} <$ 150 MeV/c to get the coherent events.
- In the end the tracks were required to have opposite charge, and the like–sign background was subtracted.

All the cuts, and the number of events surviving each of them, are listed in Table 5.1 and Table 5.2. The like sign background is less than 2% for the final selection

5.5.3 Particle identification

To distinguish pions in the final selection from electrons, the energy loss in the TPC is used. The clusters from the 159 pad rows of the TPC provide up to 159 ionization samples for track reconstruction, which can be used to calculate the energy loss (dE/dx) of the track. The dE/dx of a track is calculated as the truncated mean of the dE/dx of the clusters associated with the track. The truncated mean is used in order to reduce the fluctuations in cluster energies resulting from the Landau tail [82].

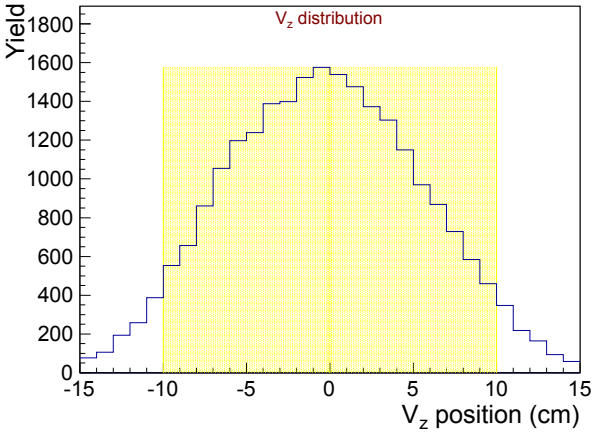

Figure 5.2: Distribution of the z–position of the vertex for events with two tracks from data. The selected range is marked with yellow.

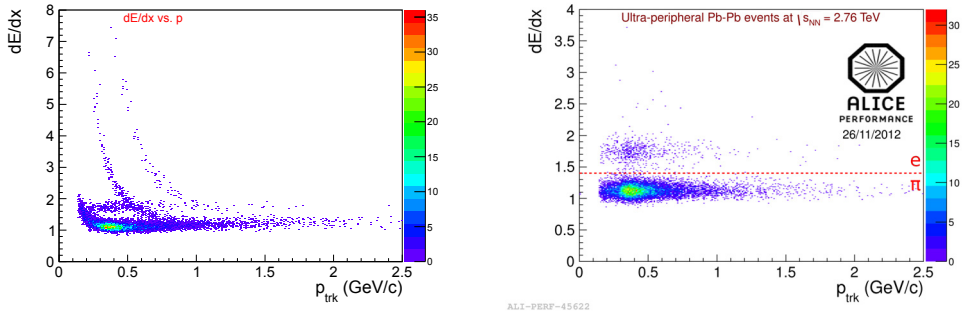

Figure 5.3: TPC energy loss vs. track momentum. Left: All triggered events with two accepted tracks. Right: After all cuts, except PID cut.

In Figure 5.3 left, the energy loss of the particles is plotted versus the track momentum, for all triggered events with two accepted tracks. As one can see the pion band is contaminated by electrons in the low momentum region ($p_{trk} < 200$ MeV/c) and by kaons and protons for higher momenta. On the right panel of Figure 5.3 the energy loss is plotted versus track momentum, for events which pass the final event selection, except the PID cut. There are still electrons left in the sample, but they are clearly distinguished from the pions. To select only pions for the final selection a cut is made on the energy loss of the track in the TPC, $\mathrm{dE/dx^{TPC}} \leq 1.4$ (a.u.).

Figure 5.4 shows the energy loss of particle 1 plotted versus the energy loss of particle 2 for events with two tracks, for the data samples from the C0OM2 trigger (left) and the CCUP2 trigger (right). The red square indicates the energy loss range $1.5 < \mathrm{dE/dx^{TPC}} < 2.1$. In Figure 5.5 the same distributions are plotted for the Starlight simulation processed through Geant for simulation of the detector response. The position in data is used to decide the energy loss selection criteria.For a track to be identified

Cut	Number of surviving events
Events analysed	3,870,215
Triggered events	1,332,041
Primary vertex	850,409
Two accepted tracks	47,978
$\|V_z\| < 10$ cm	43,413
VZERO veto	8,848
PID cut	7,588
$\|y\| < 0.5$	5,887
$p_T < 0.15$ GeV/c	2,749
Unlike sign pairs	2,699
Like sign pairs	50

Table 5.1: Number of events surviving different cuts for the C0OM2–trigger.

Cut	Number of surviving events
Events analysed	5,503,486
Triggered events	110,595
Primary vertex	94,272
Two accepted tracks	23,915
$\|V_z\| < 10$ cm	21,898
VZERO veto	15,875
PID cut	13,892
$\|y\| < 0.5$	10787
$p_T^{pair} < 150$ MeV/c	5,612
Unlike sign pairs	5,528
Like sign pairs	84

Table 5.2: Number of events surviving different cuts for the CCUP2–trigger.

as an electron it was required to have track momentum $p_{trk} > 250$ MeV/c, and have energy loss $1.5 \leq\leq 2.1$ (a.u.). The transverse momentum of the e^+e^-–pair was required to be $p_T < 200$ MeV for the event to be selected.

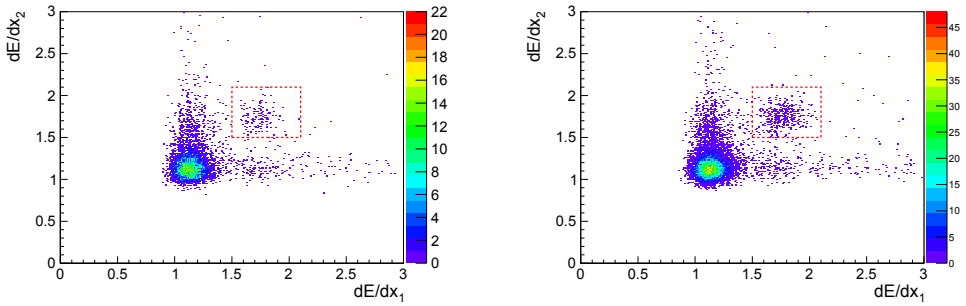

Figure 5.4: The energy loss of particle 1 vs. the energy loss of particle 2, for the C0OM2 (left) and CCUP2 (right) trigger samples.

5.5.4 Data set

The collision data are analysed with an analysis task as described above. For this analysis data recorded during the 2010 Pb–Pb run, at center–of mass energy $\sqrt{s_{NN}} = 2.76$ TeV, are used. Two different trigger classes was used to trigger the events: C0OM2 and CCUP2. A description of these trigger classes can be found in Section 4.4

For this analysis eight runs from each of the trigger classes were selected for analysis. For the C0OM2 period, this is all the good runs available, while for the CCUP2 period, the eight runs with most statistics are selected. These sixteen runs gives enough statistics for the analysis, and since the simulations used for $Acc \times Eff$ corrections needs to be anchored in the same runs, no more runs were selected to reduce the use of

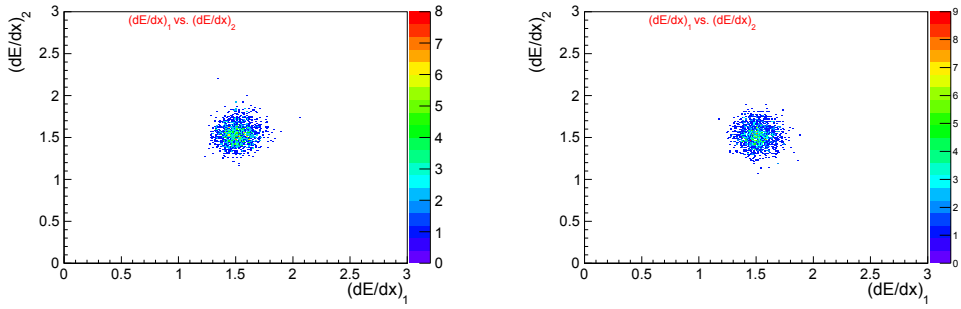

Figure 5.5: The energy loss of particle 1 vs. the energy loss of particle 2, for the C0OM2 (left) and CCUP2 (right) trigger samples, from Starlight electron events processed through Geant for detector response simulation.

simulation resources. The runs used and the number of UPC triggers in them are listed in Table 5.3 and 5.4

Run number	Run period	C0OM2 L0B triggers	C0OM2 L2A triggers
137161	LHC10h	170,071	158,348
137162	LHC10h	145,132	136,819
137230	LHC10h	200,875	141,955
137231	LHC10h	552,540	404,838
137232	LHC10h	246,197	189,866
137235	LHC10h	63,768	48,421
137236	LHC01h	145,211	116,083
137243	LHC10h	164,771	134,526
Total	LHC10h	1,688,565	1,330,856

Table 5.3: Runs with C0OM2 trigger.

5.5.5 Uncorrected distributions

In Figure 5.6 the transverse momentum spectra of all track pairs with C0OM2 (left panel) and CCUP2 (right panel) triggers are shown. The low–p_T peaks, coming from coherent photoproduced vector mesons, are clearly visible in both spectra. The background above $p_T >\sim 100$ MeV/c is relatively higher in the C0OM2 data sample, than in the CCUP2 data sample. This is as expected, since the trigger requirements are stricter for the CCUP to trigger, than for the C0OM2 trigger. In particular, no veto on VZERO is applied to the C0OM2 sample.

The uncorrected transverse momentum spectra when all event selection cuts in Section 5.5.2 are applied are shown in Figure 5.7. The data points for the unlike sign track pairs are indicated with dark red squares, and the datapoints for the like sign track pairs are indicated with blue triangles. The left column is for the C0OM2 data sample, and the right column is for the CCUP2 data sample. In the bottom row the distributions for the final selection is shown, while in the top row the distributions with all cuts, except the PID selection are shown. In the distribution for the unlike sign track pairs, a

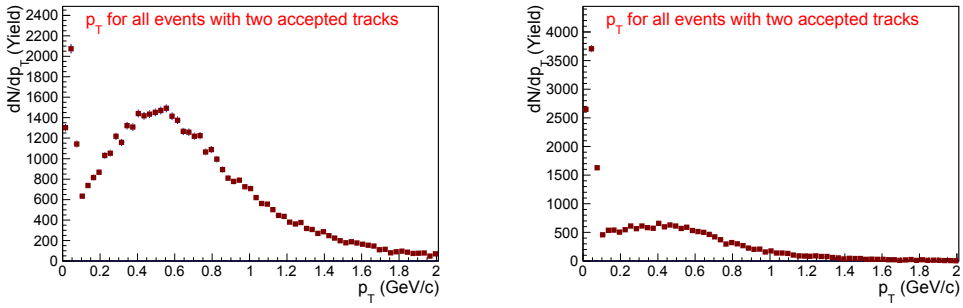

Figure 5.6: Transverse momentum for events with two accepted tracks and C0OM2 trigger (left) or CCUP2 trigger (right).

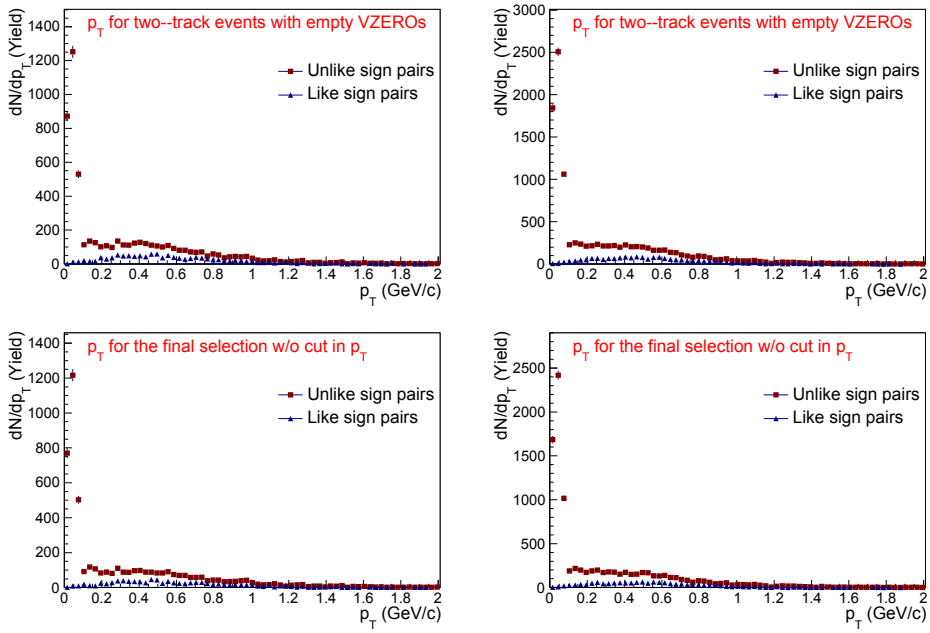

Figure 5.7: *Top row:* Transverse momentum for unlike sign and like sign track pairs with C0OM2 trigger (left) or CCUP2 trigger (right), two accepted tracks, z–position of the primary vertex within 10 cm from the central interaction region, empty VZERO detectors and $|y| < 0.5$. *Bottom row:* Same cuts as above and in addition pion PID.

Run number	Run period	CCUP2 L0B triggers	CCUP2 L2A triggers
139038	LHC10h	94,962	15,105
139107	LHC10h	145,330	19705
139173	LHC10h	78,504	11,754
139314	LHC10h	55,467	7,895
139329	LHC10h	67,095	9,276
139437	LHC10h	131,303	17,382
139465	LHC01h	169,492	23,520
139507	LHC10h	93,405	10,987
Total	LHC10H	835,564	115624

Table 5.4: Runs with CCUP2 trigger.

low–p_T peak, which is not present in the like sign distribution, is clearly visible. This peak comes from the coherent photoproduction of vector mesons.

In Figure 5.8 the transverse momentum of the track pairs is plotted versus invariant mass. In the top row all track pairs with C0OM2 trigger (left) or CCUP2 trigger (right) are shown, and in the bottom panel unlike sign track pairs with C0OM2 trigger (left) or CCUP2 trigger (right), and all other event selection cuts is Section 5.5.2, except PID at p_T cuts are shown. The peak from photoproduced ρ^0 mesons is clearly visible on all four histograms. As expected the background is higher for the C0OM2 sample, than for the CCUP2 sample. This is especially evident in the histograms for all track pairs, with no further selection.

The uncorrected invariant mass spectra for all track pairs in the C0OM2 (left) and CCUP2 (right) data samples are shown in Figure 5.9. As expected there is relatively more background in the C0OM2 sample, than in the CCUP2 sample, due to the looser trigger requirements.

In Figure 5.10 the uncorrected invariant mass distributions for both data samples are shown. In the top row all cuts, except the PID selection, has been applied. In the bottom row the distributions for the final selection are plotted. For the final selection the contribution to the background from like sign track pairs is below 2%.

It is assumed that the spectrum of like sign track pairs gives a good estimate of the combinatorial background of unlike sign track pairs, therefore the like sign spectrum is subtracted from the unlike sign spectrum. This is shown in Figure 5.11, for the C0OM2 (left) and CCUP2 (right) data samples.

5.6 Acceptance and Efficiency Corrections

The invariant mass distributions from the data analysis needs to be corrected for detector acceptance and efficiency. The geometrical acceptance is related to the coverage of the detector. In the case of photoproduced ρ^0s a number of events will be rejected because one or both tracks will hit outside of the detection region. The geometrical acceptance can then be defined as the ratio of the number of events where both tracks hits the detector and the total number of track pairs. Not all particles that goes through the detector will be reconstructed. The reconstruction efficiency is the ratio of the num-

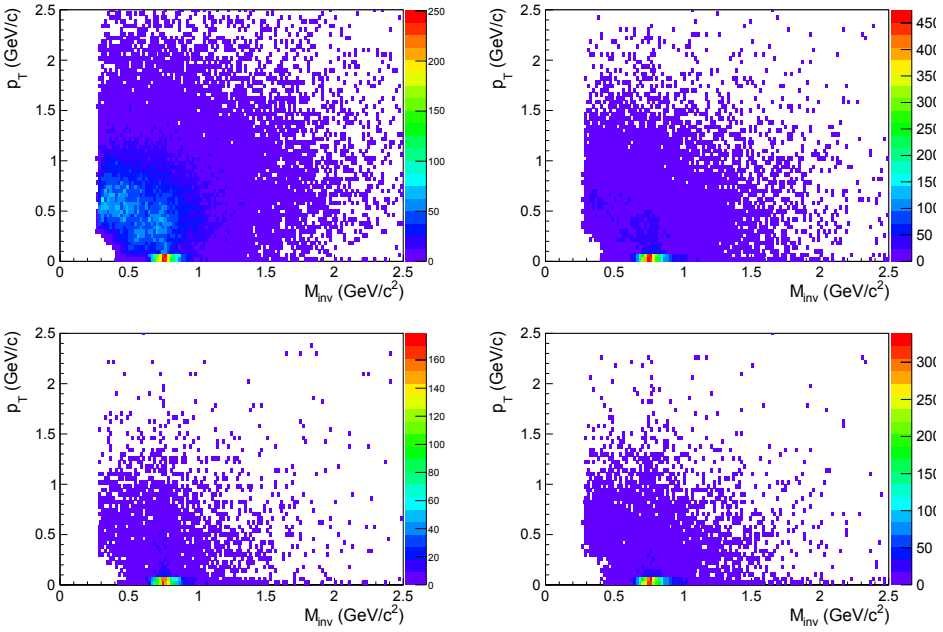

Figure 5.8: Transverse momentum plotted versus invariant mass. *Top row:* For all track pairs with C0OM2 trigger (left) or CCUP2 trigger (right). *Bottom row:* For unlike sign track pairs with C0OM2 trigger (left) or CCUP2 trigger (right), primary vertex within 10 cm from the central interaction region, empty VZERO detectors and $|y| < 0.5$. Note the different scale.

ber of reconstructed tracks to the number of particles traversing the detector. The total efficiency, or $(Acc \times Eff)_{\rho^0}$, is the product of the geometrical acceptance of the detector and the reconstruction efficiency. It can be defined as the ratio of events with two reconstructed tracks to the total number of events with a photoproduced ρ^0.

5.6.1 Simulation of a flat invariant mass distribution

To estimate $(Acc \times Eff)_{\rho^0}$ a Monte Carlo (MC) simulation is used. The ratio of the number of reconstructed events to the number of generated events was used as the product of acceptance and efficiency. In the case of the ρ^0 a simulation of two pions with a flat invariant mass distribution is used. The flat distribution was chosen because the shape of the ρ^0 peak would give low statistics for the correction at the tails of the distribution.

A simulation of two pions $(\pi^+ + \pi^-)$ with a flat invariant mass distribution in the range $2m_\pi \leq M_{inv} \leq 1.5$ GeV/c^2 was made. The transverse momentum range is $0 \leq p_T \leq 0.15$ GeV/c. The azimuthal angle distribution is uniform over $-\pi \leq \phi \leq \pi$, and it is assumed that the two pions are emitted from a transversely polarized parent, as expected for coherently produced ρ^0's. This means that the pions will be emitted with an angular distribution $\mathrm{d}n/\mathrm{d}\cos(\theta) = (1-\cos^2(\theta)) = \sin^2(\theta)$ in the rest frame of the parent The simulated particles are processed through the transport engine GEANT,

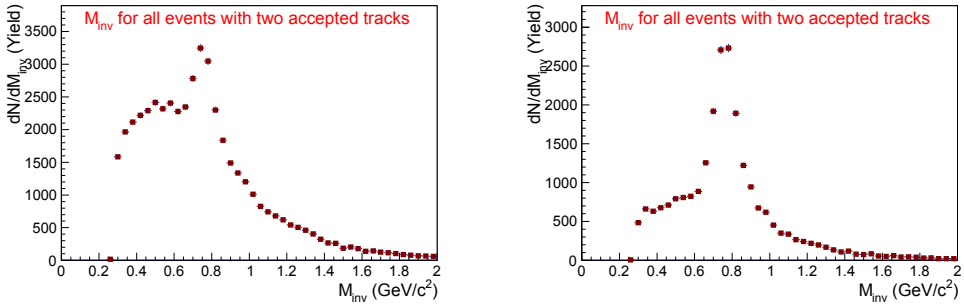

Figure 5.9: Uncorrected invariant mass distribution for all track pairs with C0OM2 (left) or CCUP2 (right) trigger.

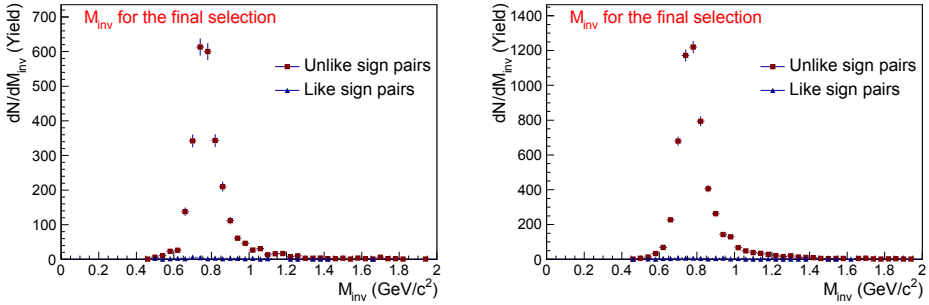

Figure 5.10: Uncorrected invariant mass distributions for the C0OM2 (left) and CCUP2 (right) data samples. Data points for unlike sign track pairs are indicated with dark red squares, and data points for like sign track pairs are indicated with blue triangles. Track pairs with primary vertex within 10 cm from the central interaction region, empty VZERO detectors, $|y| < 0.5$, $p_T < 150$ MeV/c and PID cut.

to simulate the detector response, and reconstructed with AliRoot with the same algorithms as the collision data. In the analysis one requires a trigger (C0OM2 or CCUP2) and the same selection criteria as for collision data.

The running conditions of the detector may change with time. The TPC drift time depends on the temperature and pressure. The number of active channels may vary from one run to another. The gain settings may be different during different running periods etc. The information on the status of the detector is stored in the Offline Conditions Data Base (OCDB) for each run. In the simulations, this information is used to reproduce exactly the condition of the detector. The simulations thus have to be "anchored" to a specific run.

In Figure 5.12 the invariant mass distributions for the generated and reconstructed flat invariant mass simulation is shown for run 137231 in the C0OM2 data sample (left) and run 139038 in the CCUP2 data sample (right). This is used to estimate $(Acc \times Eff)_{\rho^0}$, by taking the ratio of the reconstructed and generated events, bin by bin. Two different approaches were investigated. The first approach was to divide the rapidity interval into two, $-0.5 < y < 0.0$ and $0.0 < y < 0.5$, and correct the invariant mass

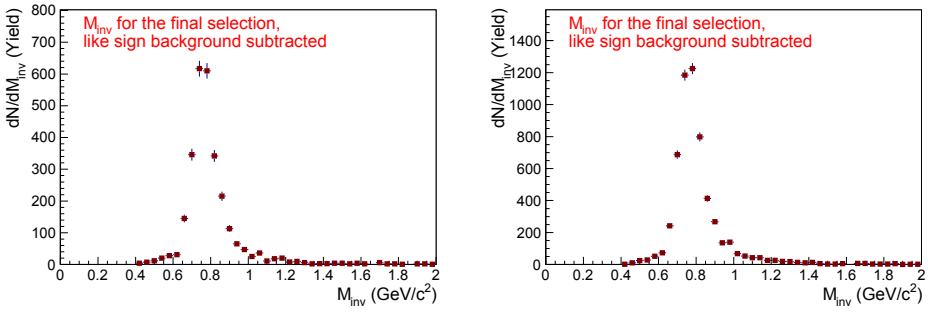

Figure 5.11: Uncorrected invariant mass distributions with like sign background subtracted for the C0OM2 (left) and CCUP2 (right) data samples. Track pairs with primary vertex within 10 cm from the central interaction region, empty VZERO detectors, $|y| < 0.5$, $p_T < 150$ MeV/c and PID cut.

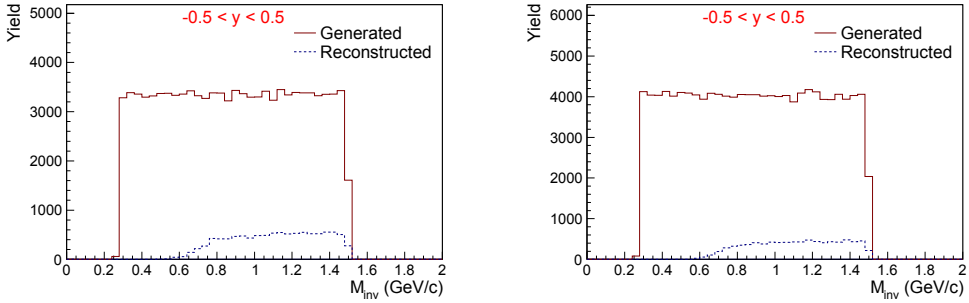

Figure 5.12: Number of generated events and number of reconstructed events in the rapidity range $-0.5 < y < 0.5$, and invariant mass range $2m_\pi \leq M_{inv} \leq 1.5$ GeV/c^2. for run 137231 in the C0OM2 data sample (left) and run 139038 in the CCUP2 data sample (right).

distributions for each of them. The $(Acc \times Eff)_{\rho^0}$ for this approach is shown in Figure 5.13. The second approach was to only use one rapidity interval, $-0.5 < y < 0.5$. The product of the acceptance and efficiency for this approach is shown in Figure 5.14. The trigger classes C0OM2 and CCUP2 both requires that both the pions reach the TOF detector. This will exclude the low momentum tracks. Because of this $(Acc \times Eff)_{\rho^0}$ goes to zero at ~ 500 MeV/c^2, and has a steep slope up to ~ 800 MeV/c^2. This is in the same region as the mass of the ρ^0. This fact makes it important with high statistics in the simulation used for the $(Acc \times Eff)_{\rho^0}$ estimate. Therefore the approach with only one bin in rapidity was chosen. The $(Acc \times Eff)$ was also checked using Starlight events, and the difference was used to estimate the systematic error on the $(Acc \times Eff)$, as will be discussed in Chapter 6

5.6.2 Starlight simulation for $\gamma\gamma \to e^+e^-$

A simulation using the Starlight event generator was made to use for acceptance and efficiency corrections and shape analysis for the process $Pb + Pb \to Pb + Pb + e^+e^-$,

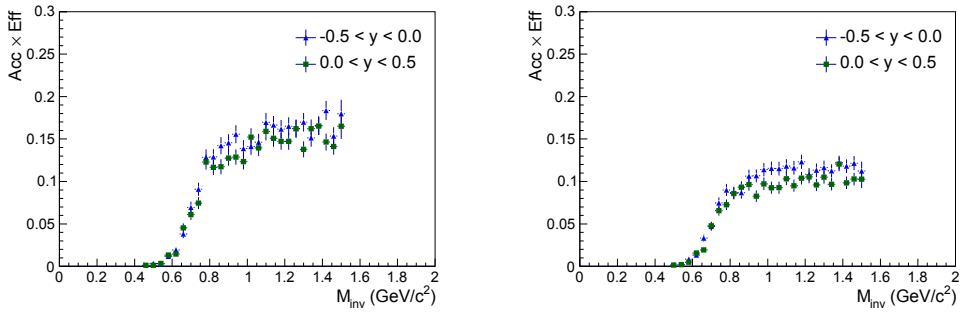

Figure 5.13: $(Acc \times Eff)$ for one run in the C0OM2 data sample (left) and the CCUP2 data sample (right), using two bins in rapidity.

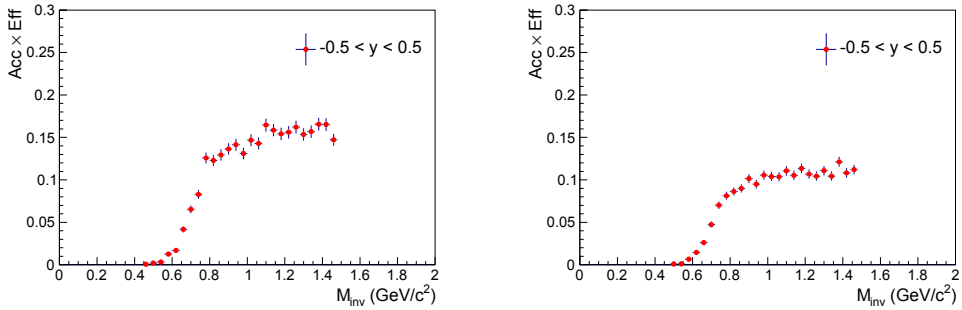

Figure 5.14: $(Acc \times Eff)$ for one run in the C0OM2 data sample (left) and the CCUP2 data sample (right), using one bin in rapidity.

where the underlying process is $\gamma\gamma \rightarrow e^+e^-$. In total 127,000 events were generated anchored in the runs with C0OM2 trigger, and 126,200 events anchored in the runs with the CCUP2 trigger. The photon–photon center of mass energy was in the interval $0.4 < W < 2.5$ GeV/c^2. To increase the statistics in the central barrel a preselection of the events based on the pseudorapidity was done, and the tracks were required to have pseudorapidites in the range $-1.5 < \eta < 1.5$.

5.6.3 Estimate of incoherent contribution at low p_T

The transverse momentum cut $p_T < 150$ MeV/c will leave mostly the coherent events, but also some incoherent events will remain. To account for this, one has to find the fraction of incoherent events with $p_T < 150$ MeV/c. To do this, a coherent and an incoherent sample of events were generated by Starlight. The events were processed through GEANT and the AliRoot simulation framework and reconstructed with the same track and event selection as used in data. The two p_T–distributions (Monte Carlo templates) were fitted to data leaving only the normalization of each distribution as free parameters. The result is shown in Figure 5.15 The data points are indicated with full circles, the coherent simulation is indicated with a full red line, the incoherent simulation is indicated with a full blue line, and the sum of the incoherent and coherent simulations is indicated with a dashed green line. The two templates fully reproduce

the p_T spectrum, and there seems to be no need for any additional component.

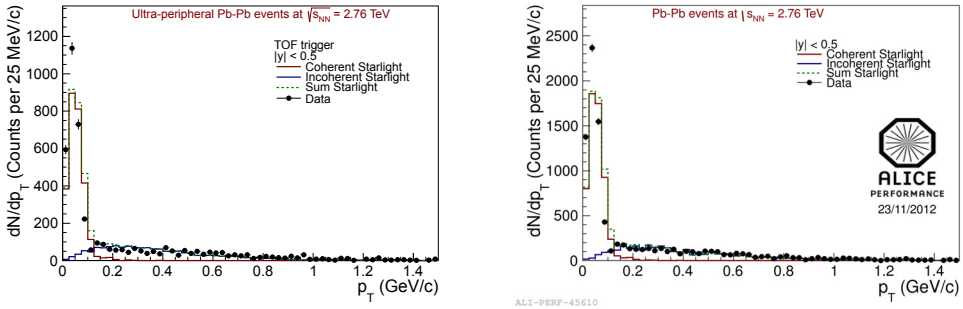

Figure 5.15: Transverse momentum distributions for collision data, Starlight simulation of coherent photoproduced ρ^0's, and Starlight simulation of incoherent photoproduced ρ^0's, for the C0OM2 (left) and CCUP2 (right) data samples.

To estimate the fraction of coherent events under the coherent peak, the fraction between the number of incoherent simulated events and the sum of incoherent and coherent events, which satisfy the p_T selection criterion of $p_T < 150$ MeV/c, is used:

$$f_{incoh} = \frac{\text{N Incoherent}(p_T < 150\text{MeV/c})}{\text{N total}(p_T < 150\text{MeV/c})} \tag{5.1}$$

Here "N Incoherent($p_T < 150$MeV/c)" is taken from the MC template. The total number of events with $p_T < 150$ MeV/c can be taken either from the histogram from data, or the histogram of the sum of the two MC templates. Even though there is a small difference in the shape of the two histograms, the number of events with $p_T < 150$ MeV/c is almost the same. Using the histogram of the sum of the two MC templates and a bin width of 15 MeV/c the fraction of incoherent events was estimated to be 8.0% and 7.0% for the C0OM2 and CCUP2 data samples respectively.

5.7 Luminosity determination

To determine the cross–section for a reaction, one has to know the integrated luminosity of the analysed data. The luminosity is given by the number of particles in each bunch (N), the number of bunches (N_b), the bunch crossing frequency (f), and the transverse size of the beam (σ):

$$\mathscr{L} = f \cdot N_b \cdot \frac{N^2}{4\pi\sigma^2} \tag{5.2}$$

The instantaneous luminosity has the units $\frac{1}{(\text{area})\cdot(\text{time})}$. For a given data sample, one has an integrated luminosity, $\int \mathscr{L} \mathrm{d}t$, which has the unit $\frac{1}{(\text{area})}$. The parameters in Equation 5.2 are, however, hard to determine directly. One therefore often determines the luminosity from the event rate for a process with a known cross section. The luminosity will then be:

$$\int \mathscr{L} \mathrm{d}t = \frac{\text{number of triggers of type A}}{\text{cross–section for trigger A}} \tag{5.3}$$

For this analysis two different methods are used to estimate the luminosity. One is based on ZDC triggers and the other on minimum bias events.

5.7.1 1ZED

In the first method the trigger input 1ZED from the ZDC detectors is used. The cross–sections for this trigger is determined by a vdM–scan and is [27]:

$$\sigma_{\text{1ZED}} = \left(371.4 \pm 0.3(\text{stat.}) \, ^{+24}_{-19}(\text{syst.})\right) \text{b} \tag{5.4}$$

The formula to calculate the analysed luminosity is shown i Equation 5.5

$$\mathscr{L}_{1ZED} = (\text{fraction analysed}) \cdot f[\text{UPC}] \cdot \frac{N_{1ZED}}{\sigma_{1ZED}} \tag{5.5}$$

where

$$(\text{fraction analysed}) = \frac{\text{Number of C0SMH triggers analysed}}{\text{Number of L2A(C0SMH) triggers from the OCDB}}, \tag{5.6}$$

and N_{1ZED} is the number of 1ZED trigger inputs. $f[\text{UPC}]$ is a correction factor for downscaling and trigger dead time which is discussed below.

5.7.2 MB

Another method to determine the luminosity is to use physics selected minimum bias events and the VZERO centrality. There are two values for the lead–lead cross section:

- Direct measurement by ALICE using ZDC [27]:$7.5 \pm 0.1(\text{stat.}) \, ^{+0.6}_{-0.5}(\text{syst.})$ b
- Glauber model calculation using the measured inelastic pp cross section [83]: 7.64 ± 0.22(syst.) b.

The two numbers are fully consistent. For this analysis $\sigma_{PbPb} = 7.64 \pm 0.22$(syst.) b is used to calculate the luminosity. The minimum bias trigger can than be used to estimate the luminosity:

$$\mathscr{L}_{MB} = f[\text{UPC}] \cdot \frac{\#\text{MB}[0-80\%]}{0.8 \cdot \sigma_{PbPb}}, \tag{5.7}$$

where $f_{ds}[\text{UPC}]$ is the downscaling factor for C0OM2 or CCUP2, and $\#\text{MB}[0-80\%]$ is the number of analysed events passing the physics selection in the given centrality range.

5.7.3 Downscaling correction

Downscaling is another source of systematic error for the dead time, especially for the CCUP2 trigger which were taken with higher instantaneous luminosity. This has been studied in detail and gave the following results [84]. The CCUP2 trigger class was downscaled with three different downscaling factors; 0.1, 0.2 and 0.5. To estimate the error, the algorithm for downscaling used in the CTP was implemented and the

bunch crossing distributions for the three downscaling factors was calculated [84]. The actual downscaling was compared to the nominal value, and the biggest deviation found was less than 0.8%. Therefore a conservative estimate of the systematic error on the downscaling is less than 0.8%. f_{ds} denotes the downscaling factors, $f_{ds}[C0OM2] = 1$, and $f_{ds}[CCUP2] = 0.1$, 0.2 or 0.5.

To check the dead time of the different trigger classes the double L0b/L0a ratios of ultra–peripheral triggers and the SPD high multiplicity trigger C0SMH was calculated (Figure 5.16). If the dead time of the compared trigger classes are the same. the double ratio should be unity. For the first two runs with C0OM2 trigger, the double ratio is found to be close to unity, whereas for later runs with that trigger the double ratio differs from unity with $\sim$20%. For runs with CCUP2 trigger, the double ratio differs from unity with a factor of $\sim$2.5.

The L0a/L0b ratios of C0OM2 and CCUP2 thus are biased. The L0a/L0b ratio of the CCUP2 trigger class is found to be 0.119 ± 0.004, using numbers from the OCDB. This is lower than for other trigger classes. The explanation for this is that the CCUP2 can trigger on after–pulses of hadronic interactions, while the veto on VZERO prevents CCUP2 to fire together with an MB trigger. As a consequence, these CCUP2 triggers on after–pulses of MB triggers are shadowed since the read–out has already started at the MB event. No after–pulses are observed for the trigger class C0SMH and therefore the L0a/L0b ratio of this trigger class is used to define:

$$f[\text{UPC}] = f_{ds}[\text{UPC}] \times \frac{\#\text{L0a(C0SMH)}}{\#\text{L0b(C0SMH)}}, \tag{5.8}$$

where UPC = C0OM2 or CCUP2, and #L0a and #L0b are the number of L0a and L0b triggers respectively.

There are two contributions to the systematic error of Equation 5.8:

- The fraction of analysed MB events, relative to analysed C0OM2, CCUP may be different. This is less than 1%.
- The error on the downscaling factor is 0.8%.

The total systematic error of Equation 5.8 is then 1.3%.

5.7.4 Luminosity results

The calculated luminosities can be seen in Tables 5.5 and 5.6, for the runs with C0OM2 and CCUP2 respectively. The luminosities were calculated using Equation 5.5 for the 1ZED method and Equation 5.7 for the MB method.

The luminosity calculated using the 1ZED method is $\sim$6% higher than the luminosity calculated using the MB method, but consistent within errors. In this analysis the luminosity from the 1ZED method is used, because σ_{1ZED} is based on a vdM–scan, while σ_{PbPb} is based on a theoretical calculation. The difference is taken into account in the systematic error. The integrated luminosities used are listed in Table 5.7

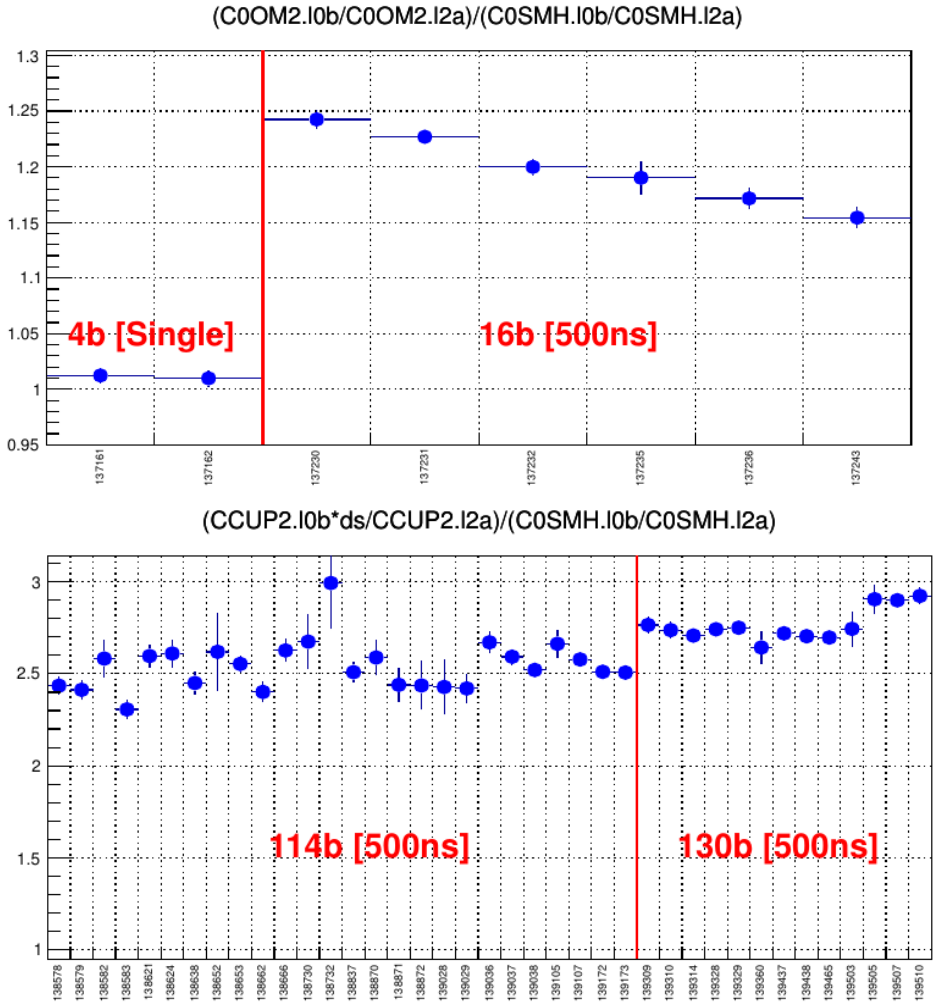

Figure 5.16: The double L0b/L0a ratio of C0OM2 (top) and CCUP2 (bottom) with C0SMH. Changes of filling schemes are indicated by red vertical lines and the filling schemes are specified by number of colliding bunches and in brackets the distance between bunches inside a bunch train. The filling schemes of runs 137161 and 137162 consisted of four single colliding bunches with 22250 ns separation. The CCUP2 L0b counters have been corrected for downscaling, denoted as ds [84].

Run number	Luminosity MB [mb^{-1}]	Luminosity 1ZED [mb^{-1}]
137161	8.6±0.5	$9.0^{+0.5}_{-0.6}$
137162	5.6±0.3	$6.0^{+0.3}_{-0.4}$
137230	7.0±0.4	$7.2^{+0.4}_{-0.5}$
137231	20.±1.2	$21.3^{+1.1}_{-1.4}$
137232	7.9±0.5	$8.4^{+0.4}_{-0.5}$
137235	2.0±0.1	$2.2^{+0.1}_{-0.1}$
137236	4.5±0.3	$4.9^{+0.2}_{-0.3}$
137243	4.3±0.3	$5.0^{+0.3}_{-0.3}$
Sum	60.4±3.6	$63.9^{+3.3}_{-4.1}$

Table 5.5: Analysed integrated luminosity in the runs with C0OM2 trigger. The luminosities was calculated using Equations 5.5 and 5.7.

Run number	Luminosity MB [mb^{-1}]	Luminosity 1ZED [mb^{-1}]
139038	27.1±1.6	$28.9^{+1.5}_{-1.9}$
139107	35.2±2.1	$37.5^{+1.9}_{-2.4}$
139173	21.7±1.3	$23.3^{+1.2}_{-1.5}$
139314	16.0±1.0	$16.9^{+0.9}_{-1.1}$
139329	18.0±1.1	$19.0^{+1.0}_{-1.2}$
139437	34.7±2.1	$36.9^{+1.9}_{-2.4}$
139465	44.4±2.7	$46.9^{+2.4}_{-3.0}$
139507	23.2±1.4	$24.4^{+1.2}_{-1.6}$
Sum	220.4±13.2	$233.7^{+12.0}_{-15.1}$

Table 5.6: Analysed integrated luminosity in the runs with CCUP2 trigger. The luminosities was calculated using Equations 5.5 and 5.7.

Trigger Class	Luminosity [mb^{-1}]
C0OM2	64^{+3}_{-4}
CCUP2	234^{+12}_{-15}

Table 5.7: Integrated luminosities used in this analysis.

Chapter 6

Results

In this chapter the results from the analysis of photoproduction of ρ^0 mesons and the analysis of two–photon production of e^+e^- pairs are presented. For the photoproduction of ρ^0 the method used for signal extraction is explained, and the systematic error estimation is discussed. In the end the calculation of the cross section is described, and the result presented. For the production of e^+e^- pairs, the invariant mass and transverse momentum distributions are presented, and two different methods of calculating the cross section for the process are explained.

6.1 Signal extraction for ρ^0

The uncorrected invariant mass distributions (Figure 5.11) is corrected for acceptance and efficiency, using the method described in 5.6.1, on a bin–by–bin basis. Because of the low efficiency, and therefore large errors, below 0.6 GeV/c^2, only bins from 0.6 GeV/c^2 to 1.5 GeV/c^2 are corrected. All other bins are set to zero. The corrected invariant mass distributions can be seen in Figure 6.1.

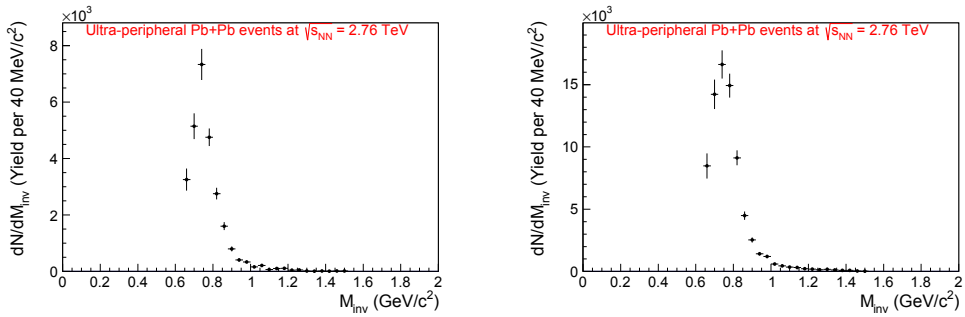

Figure 6.1: Corrected invariant mass for the C0OM2 (left) and CCUP2 (right) data samples.

The total invariant mass distribution, shown in Figure 6.1, is fitted with a Breit–Wigner function with continuum correction (Equation 6.1) [85].

$$\frac{\mathrm{d}\sigma}{\mathrm{d}M_{\pi\pi}} = \left| A\frac{\sqrt{M_{\pi\pi}M_{\rho^0}\Gamma(M_{\pi\pi})}}{M_{\pi\pi}^2 - M_{\rho^0}^2 + iM_{\rho^0}\Gamma(M_{\pi\pi})} + B \right|^2 \tag{6.1}$$

where

$$\Gamma(M_{\pi\pi}) = \Gamma_0 \cdot \frac{M_{\rho^0}}{M_{\pi\pi}} \times \left[\frac{M_{\pi\pi}^2 - 4m_\pi^2}{M_{\rho^0}^2 - 4m_\pi^2}\right]^{3/2} \tag{6.2}$$

is the momentum dependent width of the ρ^0 and M_{ρ^0} is the mass of the ρ^0. A is the amplitude of the Breit-Wigner function, and B is the amplitude of the direct $\pi^+\pi^-$ production. A few other parametrisations of the ρ^0 shape are available. The formula above has, however, become a standard for photoproduced ρ^0, and has been used earlier by e.g. STAR [39–41] and ZEUS [86]. The fitted distributions are shown in Figure 6.2 for the C0OM2 data sample, and in Figure 6.3 for the CCUP2 data sample.

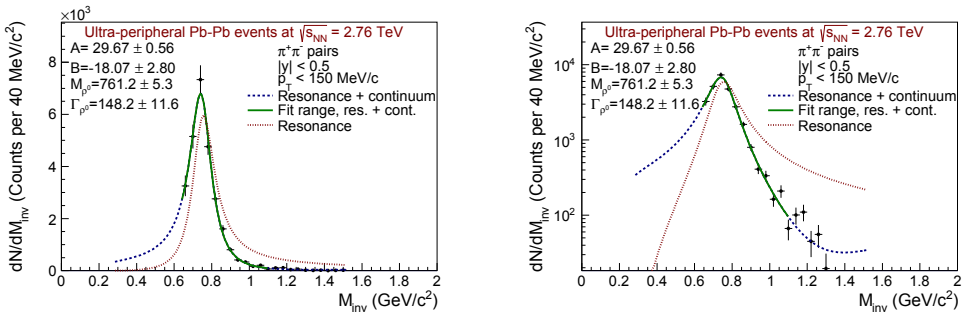

Figure 6.2: The invariant mass distribution for the C0OM2 data sample fitted with a Breit–Wigner function with continuum correction. Linear (left) and logarithmic (right) scale. The data points are marked with a full circle, the blue dashed line is the resonance plus the continuum, the full green line is the resonance plus the continuum in the range used to make the fit and the red dotted line is only the resonance. Statistical errors are shown.

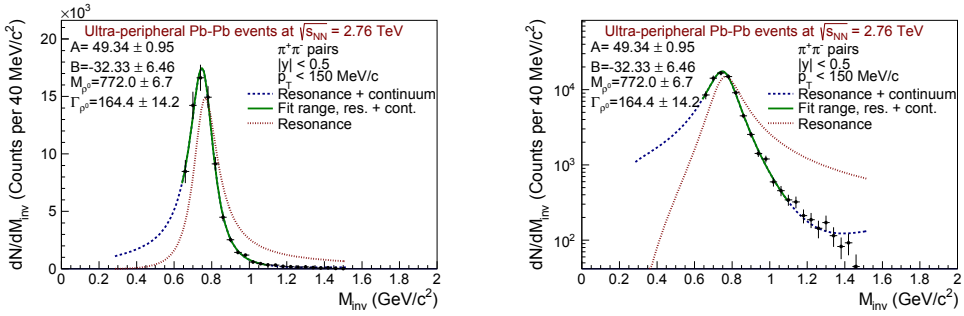

Figure 6.3: The invariant mass distribution for the CCUP2 data sample fitted with a Breit–Wigner function with continuum correction. Linear (left) and logarithmic (right) scale. The data points are marked with a full circle, the blue dashed line is the resonance plus the continuum, the full green line is the resonance plus the continuum in the range used to make the fit and the red dotted line is only the resonance. Statistical errors are shown.

The fit range was varied to obtain an estimate of the systematic uncertainty. The different results for the invariant mass and width can be seen in Tables 6.1 and 6.2, for the C0OM2 and CCUP2 data samples respectively. For the C0OM2 data sample

the fit values for the mass varies from $M_{\rho^0} = 755.9 \pm 3.2$ MeV/c^2 to $M_{\rho^0} = 768.4 \pm 5.4$ MeV/c^2, and the fit values for the width varies from $\Gamma_{\rho^0} = 130.7 \pm 6.6$ to $\Gamma_{\rho^0} = 164.3 \pm 5.8$ MeV/c^2. For the CCUP2 data sample the mass varies from $M_{\rho^0} = 764.3 \pm 3.4$ MeV/c^2 to $M_{\rho^0} = 776.1 \pm 6.9$ MeV/c^2, and the width varies from $\Gamma_{\rho^0} = 145.3 \pm 8.6$ MeV/c^2 to $\Gamma_{\rho^0} = 174.9 \pm 8.7$ MeV/c^2. For the CCUP2 data sample, the fit using the range 680 MeV/c^2 to 1000 MeV/c^2 is excluded, since this fit does not work due to the narrow fit range, and gives unreasonable values for M_{ρ^0} and Γ_{ρ^0}

The values for the mass and the width from the fits are compared to the values from Particle Data Group (PDG) [7] for photoproduced ρ^0 mesons, which are $M_{\rho^0}^{PDG} = 768.5 \pm 1.1$ MeV/c^2 and $\Gamma_{\rho^0}^{PDG} = 150.7 \pm 2.9$ MeV/c^2. For both the C0OM2 and CCUP2 data samples, the fit using the range 640 MeV/c^2 – 1100 MeV/c^2 is chosen as the one to be used for further calculations. For this selection the mass M_{ρ^0} for C0OM2 is 1.4 sigma below the PDG value, while all other results are within one sigma of the PDG value.

To extract the number of coherently produced ρ mesons, the parameter B, which represents the amplitude of non–resonant direct $\pi^+\pi-$ production, is set to zero, and the resulting fit function is integrated over the range $2M_\pi \leq M_{inv} \leq M_\rho^{PDG} + 5\Gamma_\rho^{PDG}$, which corresponds to 0.279 GeV/c$^2 \leq M_{inv} \leq$ 1.521 GeV/c^2. These integration limits are the same as those used by STAR and ZEUS. The results are listed in Table 6.1 for the C0OM2 data sample, and in Table 6.2 for the CCUP2 data sample.

The first column in Tables 6.1 and 5.6 is the range used for which data points to be included to make the fit. This should not be confused with the range of the integral used to extract the number of ρ^0 mesons, which was not varied.

Fit range (GeV/c^2)	**Extracted ρ^0's**	**|B/A|**	**M$_\rho$ (GeV/c^2)**	**Γ_ρ (GeV/c^2)**
640 – 1,000	33395 ± 3247	0.57 ± 0.12	759.4 ± 6.5	147.3 ± 14.0
640 – 1,100	$\mathbf{33012 \pm 2667}$	$\mathbf{0.61 \pm 0.10}$	$\mathbf{761.2 \pm 5.3}$	$\mathbf{148.2 \pm 11.6}$
640 – 1,200	31561 ± 1510	0.78 ± 0.09	768.4 ± 5.4	163.6 ± 6.4
640 – 1,300	33359 ± 2493	0.56 ± 0.08	758.8 ± 4.8	145.2 ± 10.5
640 – 1,400	33318 ± 1950	0.51 ± 0.05	757.0 ± 3.7	137.7 ± 7.7
640 – 1,500	33157 ± 1614	0.48 ± 0.04	755.9 ± 3.2	131.8 ± 6.0
680 – 1,000	33475 ± 4855	0.60 ± 0.20	760.3 ± 7.9	150.9 ± 21.6
680 – 1,100	33131 ± 3125	0.63 ± 0.12	761.5 ± 5.5	150.3 ± 13.8
680 – 1,200	32155 ± 1421	0.79 ± 0.07	767.0 ± 5.0	164.3 ± 5.8
680 – 1,300	33392 ± 2791	0.56 ± 0.10	758.8 ± 4.8	145.5 ± 11.8
680 – 1,400	33055 ± 2200	0.51 ± 0.06	757.3 ± 3.8	136.5 ± 8.6
680 – 1,500	32709 ± 1777	0.48 ± 0.04	756.7 ± 3.4	130.7 ± 6.6

Table 6.1: Number of extracted ρ's obtained with different ranges used as input to fit the corrected invariant mass distribution to a Breit–Wigner function, for the C0OM2 trigger sample. All error are statistical errors from the fit.

Fit range (GeV/c^2)	Extracted ρ^0's	$\lvert B/A \rvert$	M_ρ (GeV/c^2)	Γ_ρ (GeV/c^2)
640 – 1,000	90994 ± 7555	0.62 ± 0.12	770.5 ± 6.6	162.5 ± 13.1
640 – 1,100	$\mathbf{90181 \pm 7964}$	$\mathbf{0.66 \pm 0.13}$	$\mathbf{772.0 \pm 6.7}$	$\mathbf{164.4 \pm 14.2}$
640 – 1,200	88273 ± 4200	0.74 ± 0.10	775.4 ± 5.9	172.2 ± 7.0
640 – 1,300	89369 ± 2989	0.70 ± 0.04	773.7 ± 4.0	169.8 ± 4.7
640 – 1,400	91274 ± 3272	0.62 ± 0.04	769.8 ± 3.9	163.9 ± 5.2
640 – 1,500	91604 ± 4463	0.49 ± 0.04	764.3 ± 3.4	147.5 ± 6.8
680 – 1,000	62985 ± 5193	1.44 ± 0.12	792.4 ± 5.0	176.7 ± 10.0
680 – 1,100	88027 ± 5173	0.79 ± 0.14	776.1 ± 6.9	174.9 ± 8.7
680 – 1,200	89067 ± 3502	0.76 ± 0.07	774.8 ± 5.0	173.5 ± 5.5
680 – 1,300	90445 ± 3039	0.70 ± 0.04	772.7 ± 4.2	170.1 ± 4.6
680 – 1,400	91825 ± 3284	0.62 ± 0.04	769.3 ± 4.0	164.1 ± 5.1
680 – 1,500	90501 ± 5623	0.48 ± 0.06	764.8 ± 3.5	145.3 ± 8.6

Table 6.2: Number of extracted ρ's obtained with different ranges used as input to fit the corrected invariant mass distribution to a Breit–Wigner function, for the CCUP2 trigger sample. All error are statistical errors from the fit.

The chosen fit, using the range 640 MeV/c^2 – 1100 MeV/c^2, gives $33,102 \pm 2667$ (stat.) and $90,181 \pm 7964$ (stat.) extracted ρ^0's for C0OM2 and CCUP2 respectively. These numbers are later used for the calculation of the differential cross section.

6.2 Systematic errors

6.2.1 Uncertainty in luminosity determination

The systematic uncertainty in the luminosity determination comes from the systematic error in the cross section for the 1ZED trigger, determined by a vDM–scan [27]:

$$\sigma_{1\mathrm{ZED}} = \left(371.4^{+24}_{-19}(\mathrm{syst.})\right)\,\mathrm{b} \tag{6.3}$$

The relative uncertainty in the cross section is:

$$(\Delta\sigma_{1\mathrm{ZED}})_+ = \frac{24\mathrm{b}}{371.4\mathrm{b}} = +6.5\% \quad (\Delta\sigma_{1\mathrm{ZED}})_- = \frac{-19\mathrm{b}}{371.4\mathrm{b}} = -5.1\% \tag{6.4}$$

Since the cross section goes into the denominator when the luminosity is calculated positive and negative errors are switched and one gets:

$$(\Delta\mathscr{L})_+ = +5.1\% \quad (\Delta\mathscr{L})_- = -6.5\% \tag{6.5}$$

In the calculation of the cross section the luminosity goes into the denominator, and the positive and negative errors are again switched. The luminosity then gives a contribution to the total uncertainty in the cross section determination of +6.5%/-5.1%.

6.2.2 Contribution from $\gamma\gamma \to \mu^+\mu^-$

Since it is not possible to distinguish muons from pions from the TPC $\mathrm{d}E/\mathrm{d}x$, there can be a contamination from muons from the two–photon process $\gamma\gamma \to \mu^+\mu^-$ in the

data sample. Starlight simulations give that the cross section, when both tracks are required to be within the central barrel acceptance for two–photon production of $\mu^+\mu^-$ pairs is 4% of the cross section of photoproduction of ρ^0. It is furthermore reasonable to assume that there are about as many electron pairs as muon pairs in the sample. A comparison of the raw yields of ρ^0 candidates and e^+e^- candidates gives 100 e^+e^- candidates and 2,699 ρ^0 candidates in the C0OM2 data sample, which is 3.7%. In CCUP2 sample there are 310 e^+e^- candidates which is 5.6% of the 5,528 ρ^0 candidates. Contamination from muon pairs can only contribute to a lower cross section, therefore the systematic uncertainty from contamination of $\mu^+\mu^-$ pairs is +0%/-3.7% for the C0OM2 data sample, and +0%/-5.6% for the CCUP2 data sample. These numbers are consistent with the estimate from Starlight. The contribution from $\gamma\gamma \to \pi^+ + \pi^-$ is expected to be smaller and is not considered [87].

6.2.3 Uncertainty in signal extraction

The uncertainty in the signal extraction is obtained by varying the range used as input to fit the corrected invariant mass distribution to a Breit–Wigner function (Equation 6.1), and comparing the number of extracted ρ mesons. The uncertainty in the signal extraction is taken as the difference between the number of extracted ρ^0's from the chosen fit, using the range 640 MeV/c^2 – 1100 MeV/c^2, and the smallest and the largest number of extracted ρ^0's. This gives an uncertainty of $^{+1.4}_{-4.4}$% for the C0OM2 data sample, and $^{+1.8}_{-2.4}$% for the CCUP2 data sample.

6.2.4 Uncertainty from the correction of acceptance and efficiency

The acceptance and efficiency is estimated using a simulation of $\pi^+\pi^-$ pairs with a flat invariant mass distribution. The systematic uncertainty originating from the acceptance and efficiency correction is estimated by comparing the estimated $(Acc \times Eff)$ from the flat distribution with an estimate of $(Acc \times Eff)$ using a Starlight simulation of photoproduced ρ^0's decaying into two pions.

Because of the limited statistics it is not possible to compare the two estimates bin by bin. Instead an average $(Acc \times Eff)$ is estimated using the fraction of reconstructed to generated $\pi^+\pi^-$ pairs in the invariant mass interval 640 MeV/c^2 – 1100 MeV/c^2, which is the same interval used to make the fit. The estimated average $(Acc \times Eff)_{avg}$ from the two simulations are listed in Table 6.3. The estimated average correction factor from Starlight is 9.3% higher than for the flat distribution for C0OM2 and 11.7% higher CCUP2. It is assumed that for other distributions it can differ by the same amount in the negative direction. Therefore the systematic uncertainty from the acceptance and efficiency is estimated to be $\pm$9.3% for C0OM2 and $\pm$11.7% for CCUP2.

	C0OM2 $(Acc \times Eff)_{avg}$	CCUP2 $(Acc \times Eff)_{avg}$
Flat distribution	0.118 $\pm$ 0.002 (stat.)	0.084 $\pm$ 0.001 (stat.)
Starlight	0.107 $\pm$ 0.002 (stat.)	0.075 $\pm$ 0.001 (stat.)

Table 6.3: Average $(Acc \times Eff)$ estimates from a flat invariant mass distribution simulation and a Starlight simulation.

6.2.5 Uncertainty in correction for incoherent contribution

The fraction of incoherent events is estimated using Equation 5.1. To estimate the uncertainty the bin width of the histogram in Figure 5.15 is varied, and both the collision data and the simulated data is used as denominator in Equation 5.1. The bin width must be a factor of 150 to get a whole number of bins below 150 MeV/c. The results can be seen in Table 6.4 for the C0OM2 data sample, and in Table 6.5 for the CCUP2 data sample. The difference between using the collision data points or the simulated spectrum to find the total number of events with $p_T < 150$ MeV/c is found to be negligible.

Bin width	Fraction 1	Fraction 2
1 MeV/c	6.8%	6.8%
5 MeV/c	7.9%	7.8%
10 MeV/c	8.1%	8.0%
15 MeV/c	8.1%	8.0%
25 MeV/c	8.2%	8.1%
50 MeV/c	8.2%	8.0%
150 MeV/c	8.6%	8.6%

Table 6.4: The estimated fraction of events with $p_T < 150$ MeV/c that comes from incoherent photoproduction, for different bin widths, for the C0OM2 data sample. In the "Fraction 1" column the ratio between the estimated number of incoherent events with $p_T < 150$ MeV/c and the total number of events from collision data with $p_T < 150$ MeV is used. In the "Fraction 2" column the ratio between the estimated number of incoherent events with $p_T < 150$ MeV/c and the total number of reconstructed simulated events with $p_T < 150$ MeV/c is used.

Bin width	Fraction 1	Fraction 2
1 MeV/c	4.9%	4.8%
5 MeV/c	6.7%	6.6%
10 MeV/c	6.9%	6,8%
15 MeV/c	7.1%	7.0%
25 MeV/c	7.1%	7.1%
50 MeV/c	7.1%	7.0%
150 MeV/c	7.4%	7.5%

Table 6.5: The estimated fraction of events with $p_T < 150$ MeV/c that comes from incoherent photoproduction, for different bin widths, for the CCUP2 data sample. In the "Fraction 1" column the ratio between the estimated number of incoherent events with $p_T < 150$ MeV/c and the total number of events from collision data with $p_T < 150$ MeV is used. In the "Fraction 2" column the ratio between the estimated number of incoherent events with $p_T < 150$ MeV/c and the total number of reconstructed simulated events with $p_T < 150$ MeV/c is used.

The extreme cases of choice of binning, 1 MeV/c (150 bins below $p_T = 150$ MeV/c) and 150 MeV/c (1 bin below $p_T = 150$ MeV/c), are included for comparison, even though they did not give an exact representation of the data. As discussed in section 5.6.3 a binning of 15 MeV/c is used to extract the incoherent contribution at low p_T.

Including the two extreme binning options this gave a result of $f_{incoh} = (8^{+0.6}_{-1.2}\%)$ for the C0OM2 data sample, and $f_{incoh} = (7^{+0.5}_{-2.2}\%)$ for the CCUP2 data sample. If the two extreme cases are ignored the results are $f_{incoh} = (8^{+0.1}_{-0.2}\%)$ and $f_{incoh} = (7^{+0.1}_{-0.4}\%)$ for the C0OM2 and the CCUP2 data samples, respectively.

6.2.6 Combinatorial uncertainty

In STAR a second–order polynomial function was used to describe the combinatorial background. This function appeared as an extra part to the Breit–Wigner function (Equation 3.29), and the background from like–sign pairs was used to determine the parameters.

In ALICE the like–sign background is too low to be fitted to a second order polynomial, instead the like–sign pairs are used directly to estimate combinatorial background. The combinatorial background was 1.9% of the final selection for the C0OM2 data sample, and 1.5% for the CCUP2 data sample. In this analysis it is assumed that the uncertainty in the combinatorial background is as big as the contribution, and therefore $\Delta_{combinatorial}(\text{C0OM2}) = \pm 1.9\%$ and $\Delta_{combinatorial}(\text{CCUP2}) = \pm 1.5\%$.

6.2.7 Summary of systematic errors

Source	Contribution (C0OM2)	Contribution (CCUP2)
Luminosity	$^{+6.5}_{-5.1}\%$	$^{+6.5}_{-5.1}\%$
$\gamma\gamma \to \mu^+\mu^-$	$^{+0}_{-3.7}\%$	$^{+0}_{-5.6}\%$
Signal extraction	$^{+1.5}_{-4.4}\%$	$^{+1.7}_{-2.4}\%$
$(Acc \times Eff)$	$\pm 9.3\%$	$\pm 11.7\%$
Subtraction incoherent	$^{+0.6}_{-1.2}\%$	$^{+0.5}_{-2.2}\%$
Like sign pairs	$\pm 1.9\%$	$\pm 1.5\%$
Total	$^{+12}_{-13}\%$	$\pm 14\%$

Table 6.6: Contributions to the systematic uncertainties for the differential cross section for the C0OM2 and CCUP2 data samples.

6.3 Cross sections

6.3.1 Individual cross sections

The yield, N_{ρ^0}, is estimated taking the integral of the Breit–Wigner fit function of the corrected invariant mass spectrum. The fit was performed with different fit ranges, see Tables 6.1 and 6.2.

As explained in section 5.6.3 there is a fraction of incoherent events under the coherent peak at low transverse momentum. This fraction has to be subtracted from the total yield. The fractions are estimated to be $f_{incoh} = 8.0\%$ and $f_{incoh} = 7.0\%$ for the

C0OM2 and CCUP data samples respectively. The formula for calculating the differential cross section then becomes:

$$\frac{\mathrm{d}\sigma(\mathrm{Pb}+\mathrm{Pb}\rightarrow\mathrm{Pb}+\mathrm{Pb}+\rho^0)}{\mathrm{d}y}=\frac{1}{|\Delta y|}\frac{(1-f_{incoh})\cdot N_{\rho^0}}{\mathscr{L}_{int}} \tag{6.6}$$

Here, $|\Delta y|=|y_{max}-y_{min}|=|0.5-(-0.5)|=1$ is the rapidity range of the measured ρ^0 mesons.

Using ρ^0 yields, 33012 ± 2667 for C0OM2 and $90,181\pm7964$ for CCUP2, from the chosen fits, the luminosities from Table 5.7, and the fractions of incoherent events under the coherent peak explained in Section 5.6.3 one gets the results listed in Table 6.7. The systematic uncertainties are calculated using the numbers from Table 6.6.

Data sample	$\mathrm{d}\sigma/\mathrm{d}\mathbf{y}(\lvert\mathbf{y}\rvert\leq\mathbf{0.5})$
C0OM2	$(475\pm38(\mathrm{stat.})\ ^{+55}_{-62}$ (syst.) mb
CCUP2	$(359\pm32(\mathrm{stat.})\ \pm49$ (syst.) mb

Table 6.7: Differential cross section for photoproduction of ρ^0 mesons at $\sqrt{s_{NN}}=2.76$ TeV, for the two data samples.

6.3.2 Cross section difference

The differential cross section from the two data samples differ by a factor 1.32. The combined statistical error is 50 ad the difference corresponds to 2.3 sigma. There has been an effort from the UPC analysis group to find the reason for this deviation [88]. The first hypothesis is if the difference in the cross section comes from a single run. To check this the integral of the invariant mass distribution around the ρ^0 peak was taken, and divided by the luminosity. This is shown in Figure 6.4. The conclusion is that the difference does not come from a single run.

Further checks were done checking the activity in other detectors. For the FMD detector the activity is similar for both data sets, therefore a hypothesis that the efficiency of the veto in the VZERO detectors can be checked using the FMDs was falsified. Another hypothesis was that there is background in the C0OM2 data sample that can be removed by a veto on activity in the ZDC neutron counters. A cut on the ZDC energy of $E_{ZDC}<500$ GeV was therefore introduced. This had no influence on the difference in the cross sections. No evidence was found for the hypothesis that the VZERO veto in the CCUP2 trigger was too tight.

A final check is to see if there are events in the C0OM2 data sample that are not vetoed, even though they should have been. These events can be found by analysing raw ADC values. However the statistics is limited because the ADC information was only available in 13 of the events with a ρ^0 candidate. Four of these 13 events show some VZERO activity, despite the veto, but the statistics is too limited to draw a conclusion.

The samples were taken with different triggers, although with TOF contributing to both. They were also collected during very different beam conditions with the reaction rate being more than a factor 10 higher for CCUP2 than for C0OM2. The latter affects the trigger dead time corrections, as discussed in Section 5.7.3. Since it has not been

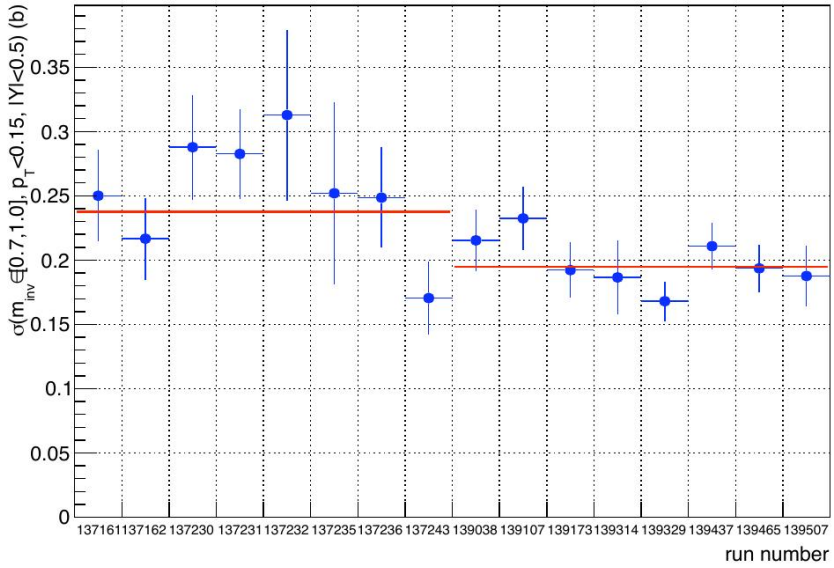

Figure 6.4: Integral of invariant mass distribution around the ρ^0 peak, depending on run number [88].

possible to find a reason to reject any of the two samples, the average will be used, and the difference will be added to the systematic error.

6.3.3 Final cross section

The final differential cross section is calculated as the weighted mean between the cross sections for the two samples using the formula:

$$\left(\frac{\mathrm{d}\sigma}{\mathrm{d}y}\right)_{final} = \frac{\sum_i x_i \cdot w_i}{\sum_i w_i}. \tag{6.7}$$

The weights, w_i, are calculated from the square of the statistical errors. δx_i, $w_i = 1/(\delta x_i)^2$. The statistical error on the average is given by

$$\delta\left(\frac{\mathrm{d}\sigma}{\mathrm{d}y}\right)_{final} = (\sum_i w_i)^{-1/2}, \tag{6.8}$$

This gives the final cross section

$$\left(\frac{\mathrm{d}\sigma}{\mathrm{d}y}\right)_{final} = (406 \pm 24\ (\mathrm{stat.}))\ \mathrm{mb} \tag{6.9}$$

To estimate the final systematic uncertainty for the weighted mean of the differential cross section the upper and lower limits are calculated separately. The relative lower limit in the uncertainty is calculated using the mean of the lower uncertainties for the

two data samples, and the relative difference between the weighed mean of the cross section and the lowest of the two measurements of the cross section (from the CCUP2 data sample). The upper limit is calculated in the same way, using the mean of the upper uncertainties for the two data samples, and the relative difference between the weighed mean of the cross section and the measured cross section from the C0OM2 data sample. The mean upper limit from the two data samples is 13%, and the mean lower limit is 14%. The difference from the weighted mean to the lowest of the two measurements is 12%, and the difference to the highest measurement from the weighed mean is 17%. This gives:

$$\delta\left(\frac{\mathrm{d}\sigma}{\mathrm{d}y}\right)_{-} = \sqrt{(14\%)^2 + (12\%)^2} = 18\% \tag{6.10}$$

$$\delta\left(\frac{\mathrm{d}\sigma}{\mathrm{d}y}\right)_{+} = \sqrt{(13\%)^2 + (17\%)^2} = 21\% \tag{6.11}$$

This gives a final result for the differential cross section of:

$$\frac{\mathrm{d}\sigma}{\mathrm{d}y} = (406 \pm 24\ (\text{stat.})\ ^{+86}_{-72}\ (\text{syst.}))\ \text{mb} \tag{6.12}$$

The measured differential cross section is compared with model calculations from the Starlight [26, 35], GGM [36, 37] and GM [38] models (see Figure 6.5). These models are explained in Section 3.5.

The GGM model is about a factor two above the measured differential cross section, while both Starlight and the GM model are consistent with the measurement within the systematic uncertainty.

6.3.4 Comparison with results from RHIC

STAR at RHIC has published the total ρ^0 cross section (integrated over all rapidities) at three different energies. To be able to compare with the current result, the cross section has to be extrapolated to full rapidity. The two models who were in best agreement with the measured cross section, Starlight and the GM model, is used for this purpose.

The extrapolation factor from $|y_{\rho^0}| < 0.5$ to full rapidity was found to be 10.6 and 9.1 for the Starlight and GM models, respectively. The average of these two factors, which is 9.9, was used to scale the cross section to full rapidity, and the difference between the individual values was added to the systematic error. This gives a total cross section of

$$\sigma(total) = (4000 \pm 560\ (\text{stat.})\ ^{+900}_{-770}\ (\text{syst.}))\ \text{mb} \tag{6.13}$$

The total cross section is compared to previous results obtained by the STAR experiment at RHIC in Table 6.8 and Figure 6.6. It is worth noting that this is about 50% of the total inelastic hadronic Pb–Pb cross section.

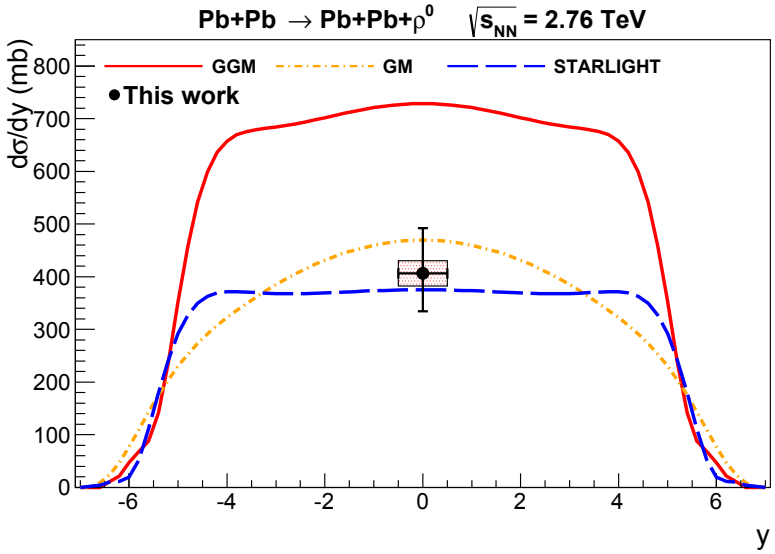

Figure 6.5: The differential cross section is compared with the models Starlight [26, 35], GGM [36, 37], and GM [38]. The systematic error for the measured differential cross section is shown with black bars, while the statistical error is shown with the red box.

	$W_{\gamma p}$ at y = 0	$d\sigma/dy(|y| < 0.5)$	σ(total)
STAR ($\sqrt{s_{NN}} = 62.4$ GeV)	7 GeV		$120 \pm 15 \pm 22$ mb
STAR ($\sqrt{s_{NN}} = 130$ GeV)	10 GeV		$460 \pm 220 \pm 110$ mb
STAR ($\sqrt{s_{NN}} = 200$ GeV)	12 GeV		$530 \pm 19 \pm 57$ mb
ALICE ($\sqrt{s_{NN}} = 2.76$ TeV)	46 GeV	$406 \pm 57^{+86}_{-72}$ mb	$4007 \pm 560^{+900}_{-770}$ mb

Table 6.8: Measured cross sections from STAR and ALICE.

6.4 Nuclear break up

In photoproduction of ρ^0 and other vector mesons the exchange of additional soft photons can lead to nuclear break up [43]. (See Figure 6.7.) This process is dominated by excitation to a Giant Dipole Resonance (GDR), followed by neutron emission.

The nuclei can break up in different ways:

- **0n0n**: No nuclear break up. No neutrons in any direction. This is a one–photon interaction.
- **Xn0n**: One of the nuclei breaks up. At least one neutron in one direction, and no neutrons in the other direction. This is a two–photon interaction.
- **XnXn**: Both nuclei break up. At least one neutron in both direction. This is a three–photon interaction.

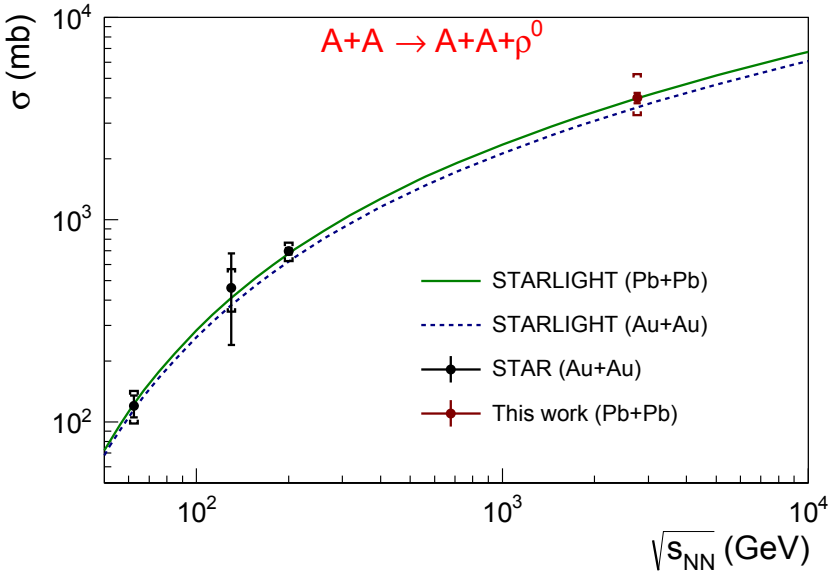

Figure 6.6: Total cross section measured by ALICE compared with results from STAR at $\sqrt{s_{NN}}$ = 62.4 GeV, $\sqrt{s_{NN}}$ = 130 GeV, $\sqrt{s_{NN}}$ = 200 GeV , and Starlight model calculations for Pb–Pb and Au–Au.

- **Xn**: At least one nucleus break up. At least one neutron emitted in one or both directions. This is a two– or three-photon interaction, and the cross section is the sum of the Xn0n and XnXn cross sections.

To detect the emitted neutrons the neutron counters in the Zero–Degree Calorimeters are used. In Figure 6.8 the distribution of deposited energy is shown for events with two accepted tracks and a vertex within $\pm$10 cm from the center of the interaction region. The peak centred around 0 GeV represents 0 neutrons emitted. The reason that the energy goes below zero, is because a pedestal value is subtracted from the energy. The next peak is centred around 1380 GeV, as expected since this is the beam energy per nucleon. To distinguish between zero detected neutrons and one or more detected neutrons a limit is set at 690 GeV, which is half the beam energy, deposited in the ZDC neutron counter. The systematic error was estimated by changing the limit between zero neutrons detected and one or more neutrons detected with $\pm$200 GeV.

Since no aspect of the extraction of the ρ^0 yield depends on how many neutrons are emitted in the ZDCs, it makes sense to compare the relative direct yield to models. For the relative yield there is furthermore no systematic difference between the C0OM2 and CCUP2 samples, so they can be combined. The result is shown in Table 6.11, where also the corresponding numbers from Starlight and Rebyakova, Strikman and Zhalov (RSZ) [51] are shown. The results are in broad agreement with the calculations and typically lie between the predictions of Starlight and RSZ.

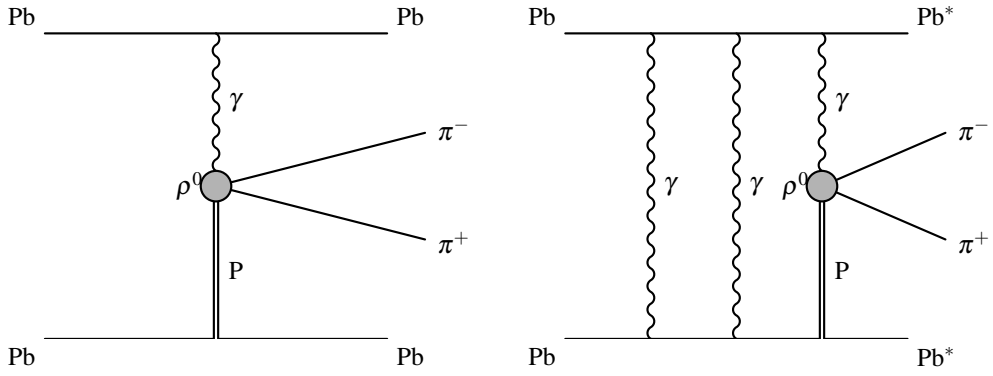

Figure 6.7: Coherent photoproduction of ρ^0 with (right) and without (left) exchange of additional photons.

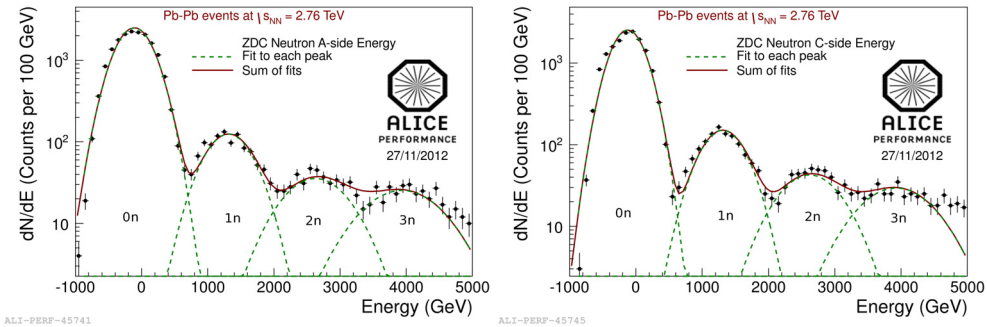

Figure 6.8: Energy deposited in the ZDC neutron counters for the A–side (left) and C–side (right), for events with C0OM2 trigger, two accepted tracks and z–position of the vertex within 10 cm from the center of the interaction region.

6.5 $\gamma\gamma \to e^+e^-$ analysis

6.5.1 Event characteristics and events selection

The $Acc \times Eff$ for $\gamma\gamma \to e^+e^-$ was determined using Starlight events as described in section 5.6.1. In the analysis the same track and event selection as for the ρ^0 analysis was used, with the following exceptions: The transverse momentum of the pair was required to be $p_T < 0.2$ GeV/c, to select the coherently produced e^+e^- pairs. This limit was increased from the one of $p_T < 0..15$ GeV/c in the ρ^0 analysis since bremsstrahlung energy loss leads to a larger broadening of the peak for e^+e^- than for $\pi^+\pi^-$. In the low track momentum region, there will be contamination from pions (Figure 5.3). Therefore the individual tracks were required to have momenta larger than p_{trk} = 0.25 GeV/c. As can be seen from Figure 5.3 the electrons has an energy loss ranging from about 1.5 to about 2.1. Therefore a cut in the energy loss of $1.5 < \mathrm{d}E/\mathrm{d}x < 2.1$ was applied. For the simulated data, the same cuts as in collision data was applied, except the cut in energy loss of the particles. As can be seen from Figure 5.5 the energy loss for the electrons is shifted to the left for the simulated data, compared with the col-

	N events	Percentage	Starlight	RSZ
Total	2699	100%	100%	100%
0n0n	2183	$(80.9 \pm 1.7$ (stat.) $^{+0.6}_{-0.9}$ (syst.))%	78.9%	84.2%
Xn0n	420	$(15.6 \pm 0.8$ (stat.) $^{+0.8}_{-0.3}$ (syst.))%	15.9%	12.1%
XnXn	96	$(3.6 \pm 0.4$ (stat.) $^{+0.1}_{-0.3}$ (syst.))%	5.2%	3.7%
Xn	516	$(19.1 \pm 0.8$ (stat.) $^{+0.9}_{-0.6}$ (syst.))%	21.1%	15.8%

Table 6.9: Percentages of events in the different break up modes, from raw yields in the C0OM2 data sample, compared with model calculations from Starlight [35, 43] and RSZ [51].

	N events	Percentage	Starlight	RSZ
Total	5528	100%	100%	100%
0n0n	4620	$(83.6 \pm 1.2$ (stat.) $^{+0.7}_{-0.7}$ (syst.))%	78.9%	84.2%
Xn0n	742	$(13.4 \pm 0.5$ (stat.) $^{+0.6}_{-0.3}$ (syst.))%	15.9%	12.1%
XnXn	166	$(3.0 \pm 0.2$ (stat.) $^{+0.1}_{-0.2}$ (syst.))%	5.2%	3.7%
Xn	908	$(16.4 \pm 0.5$ (stat.) $^{+0.7}_{-0.5}$ (syst.))%	21.1%	15.8%

Table 6.10: Percentages of events in the different break up modes, from raw yields in the CCUP2 data sample, compared with model calculations from Starlight [35, 43] and RSZ [51].

lision data. Because of this, using the same cut in energy loss for the simulated data as for collision data, would remove electrons that should have been selected. It was decided to have no cut in energy loss for the simulated data, since the simulation only contains electrons. More details about the identification of electrons can be found in Section 5.5.3

6.5.2 Histograms of selected events

In Figures 6.9 and 6.10 the invariant mass and transverse momentum distributions for the selected events are compared with the simulated distributions for both data samples. The simulated distribution is scaled to the same number of events as the distribution from collision data. The shape of the distribution is well reproduced with Starlight.

6.5.3 Calculation of cross section

The acceptance times efficiency for the reconstruction of the process $\gamma\gamma \to e^+e^-$, $(Acc \times Eff)_{\gamma\gamma\to e^+e^-}$, can be estimated by taking the fraction of the number of reconstructed simulated events after the events selection to the number of generated events:

$$(Acc \times Eff)_{\gamma\gamma\to e^+e^-} = \frac{N^{\text{sim}}_{\text{rec}}}{N^{\text{sim}}_{\text{gen}}(0.45 \leq M_{inv} \leq 2.5; |\eta| < 1.5)} \tag{6.14}$$

The cross section of the process $\gamma\gamma \to e^+e^-$ is then:

$$\sigma_{\gamma\gamma\to e^+e^-}(0.45 \leq M_{inv} \leq 2.5; |\eta| < 1.5) = \frac{1}{(Acc \times Eff)_{\gamma\gamma\to e^+e^-}} \cdot \frac{N^{\text{data}}_{\text{rec}}}{\mathscr{L}} \tag{6.15}$$

	N events	Percentage	Starlight	RSZ
Total	8227	100%	100%	100%
0n0n	6803	$(82.7 \pm 1.0$ (stat.) $^{+0.6}_{-0.7}$ (syst.))%	78.9%	84.2%
Xn0n	1162	$(14.1 \pm 0.4$ (stat.) $^{+0.6}_{-0.3}$ (syst.))%	15.9%	12.1%
XnXn	262	$(3.2 \pm 0.2$ (stat.) $^{+0.1}_{-0.2}$ (syst.))%	5.2%	3.7%
Xn	1424	$(17.3 \pm 0.5$ (stat.) $^{+0.7}_{-0.5}$ (syst.))%	21.1%	15.8%

Table 6.11: Percentages of events in the different break up modes, from raw yields in the C0OM2+CCUP2 data samples, compared with model calculations from Starlight [35, 43] and RSZ [51].

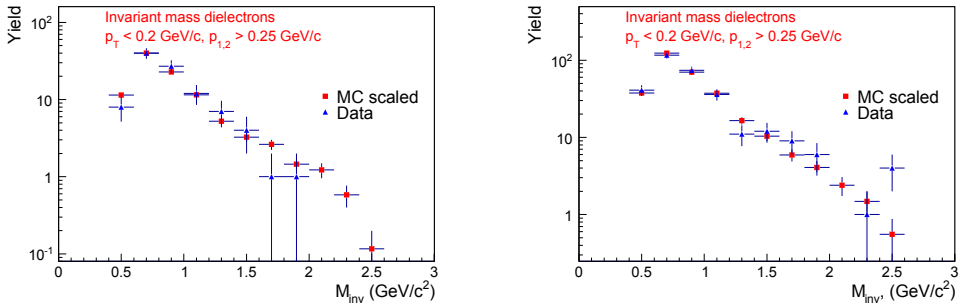

Figure 6.9: Comparison of invariant mass distributions of collision data and the Starlight simulation for the C0OM2 (left) and CCUP2 (right) data samples. The data points from collision data are indicated with blue triangles, while the Starlight data points are indicated with red squares. The simulated distributions are scaled to the same number of events as in collision data.

In Equation 6.14 and Equation 6.15 $N_{\rm rec}^{\rm sim}$ is the number of reconstructed events from simulation; $N_{\rm gen}^{\rm sim}$ is the number of generated events from simulation; $N_{\rm rec}^{\rm data}$ is the number of reconstructed events from collision data, and $\mathscr{L}$ is the integrated luminosity of the analysed data. The numbers used in the cross section calculation are listed in Table 6.12. The $(Acc \times Eff)_{\gamma\gamma\to e^+e^-}$ is calculated from $N_{rec}^{sim}/N_{gen}^{sim}$. Using Equation 6.15

	Reconstructed (data)	Reconstructed (sim)	Generated	Int. luminosity
C0OM2	100	1,716	127,000	(64^{+3}_{-4}) mb^{-1}
CCUP2	310	1,677	126,200	(234^{+12}_{-15}) mb^{-1}

Table 6.12: Numbers used in the calculation of the cross section.

and the numbers in Table 6.12 one obtains the cross sections listed in Table 6.13. The systematic errors in Table 6.13 are calculated from the error in the luminosity.

A weighted mean of the cross sections from the two data samples is calculated using Equation 6.7. The result is

$$\sigma_{\gamma\gamma\to e^+e^-}(0.45 \leq M_{inv} \leq 2.5; |\eta| < 1.5) = (103 \pm 5 \text{ (stat.) } ^{+14}_{-6} \text{ (syst.)}) \text{ mb}. \quad (6.16)$$

Here the systematic error is the square sum of the systematic errors in the individual

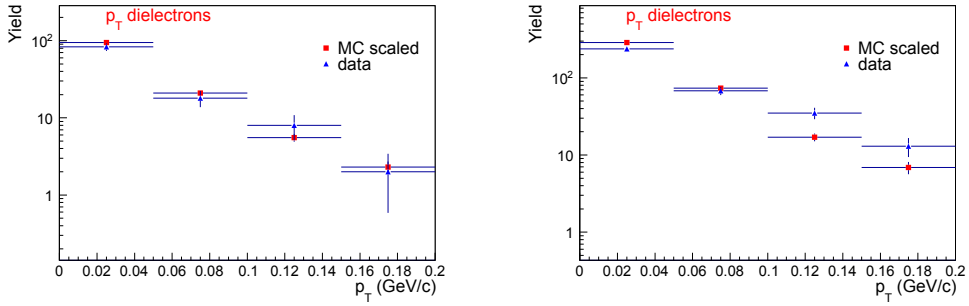

Figure 6.10: Comparison of transverse momentum distributions of collision data and the Starlight simulation for the C0OM2 (left) and CCUP2 (right) data samples. The data points from collision data are indicated with blue triangles, while the Starlight data points are indicated with red squares.The simulated distributions are scaled to the same number of events as in collision data.

	Cross section [mb]
C0OM2	116 ± 12 (stat.) $^{+8}_{-6}$ (syst.)
CCUP2	100 ± 6 (stat) $^{+7}_{-5}$ (syst.)
Weighted mean	103 ± 5 (stat.) $^{+14}_{-6}$ (syst.)
Starlight	84.3 mb

Table 6.13: The measured cross section for the process $\gamma\gamma \to e^+e^-$ compared to the cross section from Starlight.

measurements, and the difference between the weighted mean and the individual measurements. The cross section from Starlight with the corresponding selection can be obtained from the simulated sample. The cross section before the preselection is 2.56 b. To calculate the cross section for the process, with events with $|\eta| < 1.5$, a simulation of 20,000 selected events was used. These 20,000 events corresponds to 607,582 events without preselection. The cross section for one event with both tracks within $|\eta| < 1.5$ is then:

$$\frac{20,000}{607,652} \cdot 2.561 \text{ b} = 0.0843 \text{ b} = 84.3 \text{ mb} \tag{6.17}$$

The cross section from Starlight is 18% lower than the measured one. A similar trend was observed for higher invariant masses [46]. The deviation is, however, only slightly above two sigma if the statistical and systematic errors are added in quadrature, so it is not possible to draw any definite conclusions about a possible deviation from Starlight.

6.5.4 Differential two–photon cross section

The $Acc \times Eff$ correction can also be calculated bin–by–bin in invariant mass to obtain the corrected $d\sigma/dM_{inv}$ distribution. The resulting acceptance times efficiency distributions are shown in Figure 6.11 for both the C0OM2 and CCUP2 data samples. Events

were selected from the two data samples, using the cuts described above, resulting in the uncorrected invariant mass distributions shown in Figure 6.12. The uncorrected distributions were then corrected for acceptance and efficiency.

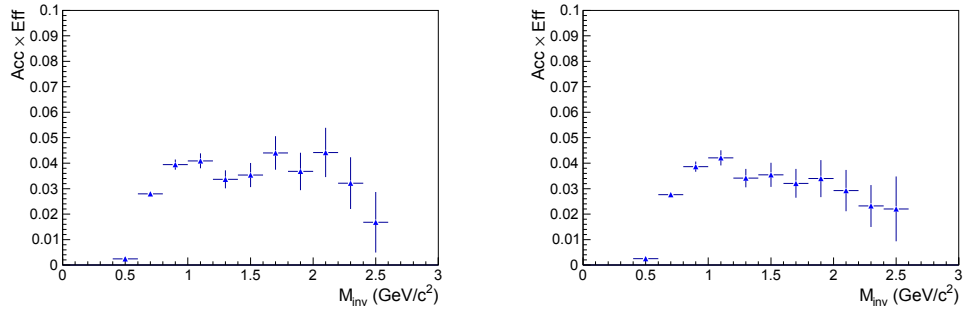

Figure 6.11: $(Acc \times Eff)_{\gamma\gamma \to e^+e^-}$ as a function of invariant mass, for the C0OM2 (left) and CCUP2 (right) data samples.

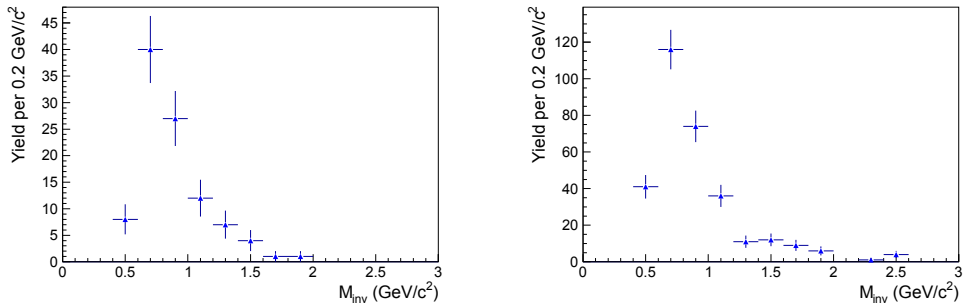

Figure 6.12: Uncorrected invariant mass distributions of $\gamma\gamma \to e^+e^-$ for the C0OM2 (left) and CCUP2 (right) data samples.

The cross section as a function of invariant mass, $\frac{d\sigma}{dM_{inv}}$, was calculated using the formula

$$\frac{d\sigma}{dM_{inv}} = \frac{N_{e^+e^-}}{\mathscr{L} \cdot \Delta M_{inv}} \cdot \frac{1}{Acc \times Eff} \tag{6.18}$$

where $N_{e^+e^-}$ is the number of e^+e^- pairs in each bin in invariant mass; $\mathscr{L}$ is the integrated luminosity from Table 5.7; and ΔM_{inv} is the invariant mass bin width, which in this case is 0.2 GeV/c^2. In Figure 6.13 the measured cross section from collision data is compared with the cross section calculated by Starlight. The distribution of the generated cross section as a function of invariant mass is calculated using the formula

$$\frac{d\sigma_{SL}}{dM_{inv}} = \frac{N_{e^+e^-}(bin)}{N_{e^+e^-}(tot)} \cdot \frac{\sigma_{SL}^{tot}}{\Delta M_{inv}} \tag{6.19}$$

where $N_{e^+e^-(bin)}$ is the number of entries in each invariant mass bin; $N_{e^+e^-}(tot)$ is the total number of generated e^+e^- pairs; σ_{SL}^{tot} is the total cross section of the process $\gamma\gamma \to e^+e^-$ from Starlight, which is $\sigma_{SL}^{tot} = 84$ mb; and ΔM_{inv} is the invariant mass bin width, which is 0.2 GeV/c^2.

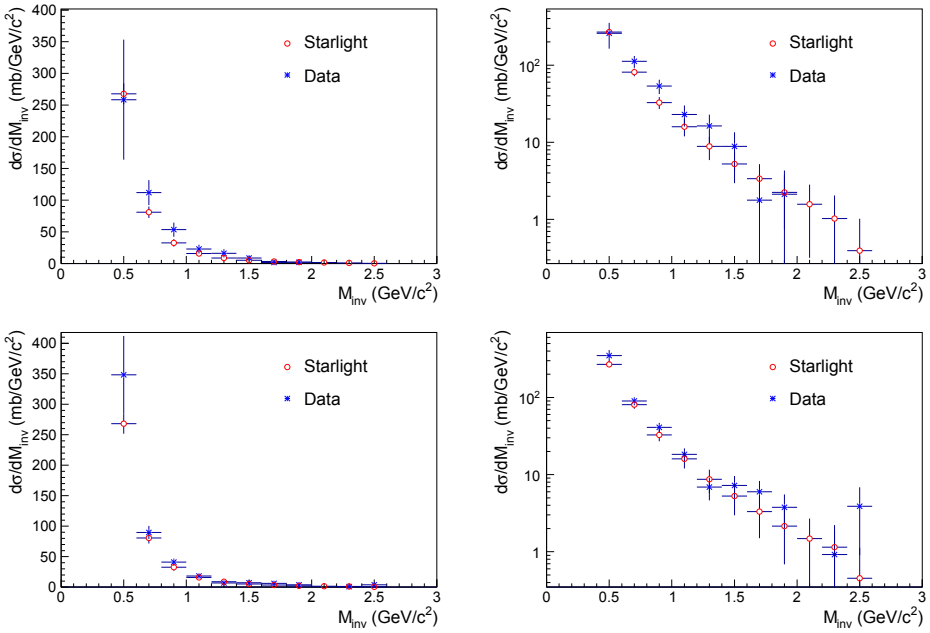

Figure 6.13: The measured cross section for the process $\gamma\gamma \to e^+e^-$ as a function of invariant mass, for the C0OM2 (top row) and CCUP2 (bottom row) data samples, on linear (left column) and logarithmic (right column) scale.

Chapter 7

Conclusions

In this thesis results for photoproduction of ρ^0 mesons and two–photon production of e^+e^- pairs produced in Pb–Pb collisions at $\sqrt{s_{NN}} = 2.76$ TeV, measured by the ALICE experiment has been presented. These results were obtained during the first heavy–ion run with a rather low luminosity and show the feasibility of studying ultra–peripheral collisions at heavy–ion colliders at the highest energies. They also illustrate the strong photon fluxes associated with relativistic heavy ions and the importance of Vector Meson Dominance, which lead to a cross section for photoproduction of ρ^0 mesons equal to about half the inelastic hadronic cross section.

The measured differential cross section for photoproduction of ρ^0 is in agreement with Starlight and model calculations by Gonçalves and Machado, and a factor two below the Glauber calculations by Frankfurt, Strikman and Zhalov. This is similar to trends observed by the STAR experiment at RHIC. The good agreement with Starlight is a bit surprising since in that model the total ρ^0+nucleus cross section is equal to the inelastic cross section [22]. In a proper Glauber calculation for an opaque nucleus one would expect the elastic cross section to be about equal to the inelastic cross section. This would lead to a cross section about four times larger than in Starlight, clearly not consistent with the current results, nor with the results from RHIC. The calculation by FSZ does include a proper treatment of the Glauber model. The cross section is however reduced by roughly a factor of two from non–diagonal transitions, $\gamma \rightarrow \rho' \rightarrow \rho$. But apparently this reduction is not enough and their calculation overpredicts the cross section by nearly a factor of two.

The calculation by GM is based on the colour dipole model and is consistent with data. The use of the colour dipole model for a soft, non–perturbative state like the ρ^0 has, however, been criticized [51]

For two–photon production of e^+e^- pairs, the measured cross section is consistent with Starlight leading order calculations. This put constrains on other models which take into account higher order terms and strong field effects. One QED calculation has found that higher–order terms do not modify the mid–rapidity cross section for $M_{inv} \gg m_e$, while another study concluded that higher order terms may lead to a reduction by $\sim$30% [89]. A direct comparison with these models is not possible since no cross sections for the same selection as used here is available in the published literature. The results obtained should, however, set constraints on these and possible future calculations.

Future runs with higher luminosity will enable one to study more rare probes and

higher mass final states in ultra–peripheral collisions. These include heavy vector mesons such as the $\psi(2S)$ and Υ and also various two–photon final states, e.g. $K^s_0 K^s_0$, η_c, and W^+W^-. The next heavy–ion run is foreseen to be at $\sqrt{s} = 5.5$ TeV. Measuring photoproduction at mid–rapidity would extend the γ–nucleon center–of–mass energy to $W_{\gamma p} = 65$ GeV.

Appendix A

Glossary

AB Adeluyi and Bertulani's model

AGS Alternating Gradient Synchrotron

ALICE A Large Ion Collider Experiment

AliEn Alice Environment

AOD Analysis Object Data

ATLAS A Large LHC Apparatus

BNL Brookhaven National Laboratory

BRAHMS Broad Range Hadron Magnetic Spectrometer

BUPC Barrel Ultra–Peripheral Collisions trigger

CERN The European Organization for Nuclear Research

CINT C++ Interpeter

CMS Compact Muon Solenoid

CP Charge Parity

CSS Cisek, Szczurek and Schäfer's model

CTB Central Trigger Barrel

CTP Central Trigger Processor

CU Control Unit

DAQ Data Acquistion System

DC Drift Chamber

DCA Distance of Closest Approach

DCS Detector Control System

DDL Detector Data Link

DIS Deep Inelastic Scattering

DU Device Unit

EMC European Muon Collaboration

EMCAL Electromagnetic Calorimeter

ESD Event Summary Data

FMD Forward Multiplicity Detector

FSM Finite State Machine

FUPC Forward UPC Trigger

GDC Global Data Consentrator

GDR Giant Dipole Resonance

GGM Gribov Glauber Model, by Frankfurt, Strikman and Zhalov

GM Gonçalves and Machado's model

GVDM Generalized Vector Meson Dominance Model

HERA Hadron-Elektron-Ringanlage, or Hadron-Electron Ring Accelerator

HLT High Level Trigger

HMPID High Momentum Particle Identification Detector

ITS Inner Tracking System

JCOP Joint Control Project

L0 Trigger Level 0

L1 Trigger Level 1

L2 Trigger Level 2

LDC Local Data Consentrator

LHC Large Hadron Collider

LHCb LHC beauty

LM Lappi and Mantysaari's model

LU Logical Unit

MC Monte Carlo

MWPC Multiwire Proportional Chamber

MRPC Multigap Resistive Plate Chamber

nPDF Nuclear Parton Distribution Function

OCDB Offline Conditions Data Base

PDF Parton Distribution Function

PDG Particle Data Group

PHENIX Pioneering High–Energy Nuclear Interactions Experiment

PHOBOS PHOBOS experiment at RHIC

PHOS Photon Spectrometer

PID Particle Identification

PLC Programmable Logic Controller

PMD Photon Multiplicity Detector

PVSS Prozessvisualisierungs- und Steuerungssystem – Process visualization and control system

QCD Quantum chromodynamics

QED Quantum electrodynamics

QGP Quark Gluon Plasma

RHIC Relativistic Heavy Ion Collider

RICH Ring–Imaging Čerenkov Detector

RSZ Rebyakova, Strikman and Zhalov's model

SCADA Supervisory Control and Data Acquistion

SDD Silicon Drift Detector

SPD Silicon Pixel Detector

SPS Super Proton Synchrotron

SSD Silicon Strip Detector

STAR Solenoidal Tracker at RHIC

TOF Time–Of–Flight detector

TPC Time Projection Chamber

TRD Transition Radiation Detector

UPC Ultra-peripheral collisions

vdM–scan van der Meer–scan

WLCG Worldwide LHC Computing Grid

ZDC Zero–Degree Calorimeter

ZEM Zero–Degree Electromagnetic Calorimeter

ZN ZDC Neutron Detector

ZP ZDC Proton Detector

Bibliography

[1] CERN Document Server, http://cdsweb.cern.ch. 1.1

[2] G. Aad *et al.*, ATLAS Collaboration, Phys.Lett. **B716**, 1 (2012), arXiv:1207.7214. 1

[3] S. Chatrchyan *et al.*, CMS Collaboration, Phys.Lett. **B716**, 30 (2012), arXiv:1207.7235. 1

[4] L. McLerran, The Color Glass Condansate and Small x Physcs: 4 Lectures, http://arxiv.org/abs/hep-ph/0104285, 2001. 2.2

[5] D. Griffiths, *Introductions to elementary particles* (John Wiley & Sons Inc, 1987). 2.2.1

[6] W. Greiner and J. Reinhardt, *Quantum Electrodynamics*, Second corrected ed. (Springer, 1996), p. 202. 2.2.1

[7] J. Beringer *et al.*, Particle Data Group, Phys.Rev. **D86**, 010001 (2012). 2.2.2, 6.1

[8] H. Fritzsch and K.-H. Streng, Physics Letters B **72**, 385 (1978). 2.2.2

[9] C. A. Salgado *et al.*, Journal of Physics G: Nuclear and Particle Physics **39**, 015010 (2012). 2.5

[10] N. Armesto, J.Phys. **G32**, R367 (2006), arXiv:hep-ph/0604108. 2.2.2, 2.2.2

[11] B. Muller, J. Schukraft, and B. Wyslouch, Ann.Rev.Nucl.Part.Sci. **62**, 361 (2012), arXiv:1202.3233. 2.2.3

[12] GSI Helmholtzzentrum für Schwerionenforschung GmbH Webpage, http://www.gsi.de, Accessed 24th October, 2011. 2.6

[13] S. Voloshin and Y. Zhang, Z. Phys. C **70**, 665 (1996). 2.3

[14] K. Aamodt *et al.*, ALICE Collaboration, Phys. Rev. Lett. **105**, 252302 (2010). 2.3, 2.7

[15] K. Aamodt *et al.*, ALICE Collaboration, Physics Letters B **696**, 30 (2011). 2.3, 2.8

[16] B. Abelev *et al.*, ALICE Collaboration, Phys.Lett. **B720**, 52 (2013), arXiv:1208.2711. 2.8

[17] E. Fermi, arXiv:hep-th/0205086, 1924. 3.1

[18] C. F. von Weizsacker, Z.Phys. **88**, 612 (1934). 3.1

[19] E. J. Williams, Kgl. Danske Videnskab Selskab, Mat.–fys. Medd **13, No. 4** (1935). 3.1

[20] J. D. Jackson, *Classical Electrodynamics 2nd ed* (John Wiley & Sons, New York, 1975). 3.1, 3.2

[21] A. J. Baltz *et al.*, Physics Reports **458**, 1 (2008). 3.2, 3.4

[22] C. A. Bertulani, S. R. Klein, and J. Nystrand, Annu. Rev. Nucl. Part. Sci. **55**, 271 (2005). 3.2, 3.4, 3.4.1, 3.4.1, 3.4.2, 3.1, 3.5, 7

[23] R. N. Cahn and J. D. Jackson, Phys. Rev. D **42**, 3690 (1990). 3.3

[24] G. Baur and L. G. Ferreira Filho, Nucl.Phys. **A518**, 786 (1990). 3.3

[25] J. Nystrand and S. R. Klein, LBNL **42524** (1998). 3.3, 3.3, 3.3, 3.6.1

[26] S. R. Klein and J. Nystrand, Phys. Rev C. **60**, 014903 (1999). 3.4, 3.4.1, 3.5, 3.2, 3.3, 3.5, 3.6.1, 3.7.2, 6.3.3, 6.5

[27] B. Abelev *et al.*, ALICE Collaboration, Phys.Rev.Lett. **109**, 252302 (2012), arXiv:1203.2436. 3.4, 5.7.1, 5.7.2, 6.2.1

[28] A. Toia, J.Phys. **G38**, 124007 (2011), arXiv:arXiv:1107.1973. 3.4

[29] G. McClellan *et al.*, Phys. Rev. D **4**, 2683 (1971). 3.4.1

[30] H. J. Behrend, F. Lobkowicz, E. H. Thorndike, A. A. Wehmann, and M. E. Nordberg, Phys. Rev. Lett. **24**, 1246 (1970). 3.4.1

[31] G. McClellan *et al.*, Phys. Rev. Lett. **26**, 1593 (1971). 3.4.1

[32] A. Bunyatyan, Nucl.Phys.Proc.Suppl. **179-180**, 69 (2008). 3.4

[33] J. J. Sakurai, Annals of Physics **11**, 1 (1960). 3.4.1

[34] M. G. Ryskin, Z.Phys. **C57**, 89 (1993). 3.4.1

[35] Starlight Monte Carlo Generator, `http://starlight.hepforge.org`. 3.5, 3.3, 3.5, 3.7.1, 6.3.3, 6.5, 6.9, 6.10, 6.11

[36] L. Frankfurt, M. Strikman, and M. Zhalov, Phys.Lett. **B537**, 51 (2002), arXiv:hep-ph/0204175. 3.5, 3.3, 3.5, 3.6.1, 6.3.3, 6.5

[37] L. Frankfurt, M. Strikman, and M. Zhalov, Phys.Rev. **C67**, 034901 (2003), arXiv:arXiv:hep-ph/0210303. 3.5, 3.3, 3.5, 3.6.1, 6.3.3, 6.5

[38] V. P. Goncalves and M. V. T. Machado, Phys.Rev. **C84**, 011902 (2011), arXiv:arXiv:1106.3036. 3.5, 3.3, 3.5, 6.3.3, 6.5

[39] G. Agakishiev *et al.*, STAR Collaboration, Phys.Rev. **C85**, 014910 (2012), arXiv:1107.4630. 3.6, 3.6.1, 3.4, 3.5, 3.10, 6.1

[40] C. Adler and others, STAR Collaboration, Phys. Rev. Lett **89**, 272302 (2002). 3.6, 3.6.1, 3.6, 3.4, 3.5, 6.1

[41] B. I. Abelev *et al.*, STAR Collaboration, Phys. Rev. C **77**, 034910 (2008). 3.6, 3.6.1, 3.7, 3.8, 3.4, 3.5, 3.6.1, 3.9, 6.1

[42] S. Afanasiev *et al.*, PHENIX Collaboration, Phys.Lett. **B679**, 321 (2009), arXiv:0903.2041. 3.6, 3.6.2, 3.11, 3.6

[43] A. J. Baltz, S. R. Klein, and J. Nystrand, Phys.Rev.Lett. **89**, 012301 (2002), arXiv:nucl-th/0205031. 3.6.1, 6.4, 6.9, 6.10, 6.11

[44] V. P. Goncalves and M. V. T. Machado, Eur. Phys. J. C **40**, 519 (2005). 3.6.1

[45] B. Abelev *et al.*, ALICE Collaboration, Phys. Lett. B **718**, 1273 (2013). 3.7, 3.7.1, 3.12, 3.7.1, 3.7.1, 3.7.1, 3.7.2, 3.7.2, 3.7.2

[46] E. Abbas *et al.*, ALICE Collaboration, Eur. Phys. J. C **73**, 2617 (2013), arXiv:1305.1467. 3.7, 3.7.1, 3.7.1, 3.13, 3.7.1, 3.7.1, 3.7.1, 3.7.2, 3.7.2, 3.7.2, 3.14, 6.5.3

[47] R. Aaij *et al.*, LHCb collaboration, J.Phys. **G40**, 045001 (2013), arXiv:1301.7084. 3.7

[48] S. Chatrchyan *et al.*, CMS Collaboration, JHEP **1201**, 052 (2012), arXiv:1111.5536. 3.7

[49] S. Chatrchyan *et al.*, CMS Collaboration, (2013), arXiv:1305.5596. 3.7

[50] J. E. Gaiser, *Charmonium spectroscopy from radiative decays of the J/ψ and ψ'*, PhD thesis, Stanford Linear Accelerator Center, Stanford University, 1982. 3.7.1

[51] V. Rebyakova, M. Strikman, and M. Zhalov, Phys. Lett. B **710**, 647 (2012). 3.7.1, 3.7.2, 6.4, 6.9, 6.10, 6.11, 7

[52] A. Adeluyi and C. A. Bertulani, Phys. Rev. C **85**, 044904 (2012). 3.7.2

[53] V. P. Gonçalves and M. V. T. Machado, Phys. Rev. C **84**, 011902 (2011). 3.7.2

[54] A. Cisek, W. Schäfer, and A. Szczurek, Phys. Rev. C **86**, 014905 (2012). 3.7.2

[55] T. Lappi and H. Mantysaari, Phys.Rev. **C87**, 032201 (2013), arXiv:1301.4095. 3.7.2

[56] The ALICE Collaboration, Technical Proposal for A Large Ion Collider Experiment at the CERN LHC, `http://cdsweb.cern.ch/record/293391`, 1995. 4

[57] The ALICE Collaboration, Journal of Instrumentation **3**, S08002 (2008). 4, 4.1.1, 4.2, 4.1, 4.1.2, 4.1.3, 4.1.4, 4.1.5, 4.1.5, 4.6, 4.2, 4.7, 4.2, 4.3.1, 4.8, 4.3, 4.3.1, 4.3.2, 4.9, 4.10, 4.4, 4.3.2, 4.3.3, 4.4.1, 4.4.2, 4.11, 4.7, 4.12, 4.13, 5.1, 5.4

[58] The ALICE Collaboration, ALICE Technical Design Report of the Inner Tracking System (ITS), http://aliceinfo.cern.ch/Documents/TDR/index.html, 1999. 4.1.1

[59] D. R. Nygren, LBL internal report (1974). 4.1.2

[60] D. R. Nygren, Phys. Scripta **23**, 584 (1981). 4.1.2

[61] J. Alme *et al.*, Nuclear Instruments and Methods in Physics Research Section A: Accelerators, Spectrometers, Detectors and Associated Equipment **622**, 316 (2010). 4.1.2

[62] The ALICE Collaboration, ALICE Technical Design Report of the Time Projection Chamber, http://edms.cern.ch/document/398930, 2000. 4.1.2

[63] The ALICE Collaboration, ALICE Technical Design Report of the Transition Radiation Detector, http://aliceinfo.cern.ch/Documents/TDR/index.html, 2001. 4.1.3

[64] The ALICE Collaboration, ALICE Technical Design Report of the Time Of Flight System, http://aliceinfo.cern.ch/Documents/TDR/index.html, 2000. 4.1.4, 4.1.4

[65] A. Silenzi, *The topological trigger system of the TOF detector for the ALICE experiment at the LHC*, PhD thesis, Alma Mater Studiorum Universita di Bologna, 2010. 4.1.4, 4.5

[66] The ALICE Collaboration, ALICE Technical Design Report of the Trigger, Data Acquisition, High–Level Trigger and Control System, https://edms.cern.ch/document/456354/1, 2004. 4.5, 4.6, 4.7

[67] E. Abbas *et al.*, ALICE Collaboration, (2013), arXiv:1306.3130. 4.4.1

[68] ALICE Electronic Logbook, https://alice-logbook.cern.ch. 4.6, 4.7, 4.8, 4.9

[69] ALICE CTP group, List of ALICE Trigger Class Codes, http://epweb2.ph.bham.ac.uk/user/krivda/alice/. 4.6, 4.7

[70] ALICE trigger system for newcomers, http://www.ep.ph.bham.ac.uk/twiki/bin/view/ALICE/AliceTriggerIntroduction, Accessed 16th March, 2012. 4.4.2

[71] F. Antinori, Naming sheme for ALICE trigger classes v0.1, http://aliceinfo.cern.ch/Offline/sites/aliceinfo.cern.ch.secure.Offline/files/uploads/trigger/class-naming-01.pdf, Accessed 16th March, 2012. 4.4.2

[72] The ALICE Collaboration, ALICE Technical Design Report of High–Level Trigger, https://wiki.kip.uni-heidelberg.de/ti/HLT/index.php/Design_Reports, 2003. 4.5

[73] B. Wagner, 2013, Private communication. 5.1

[74] The ALICE Offline group, The ALICE Offline Bible Rev. 22. 5.1

[75] The ALICE Offline project, `http://aliceinfo.cern.ch/Offline`, Accessed 8th December, 2011. 5.2

[76] R. Bruun and F. Rademakers, ROOT - An Object Oriented Data Analysis Framework, Proceedings AIHENP'96 Workshop, Lausanne, Sep. 1996, Nucl. Inst. & Meth. in Phys. Res. A 389 (1997) 81-86. See also `http://root.cern.ch/`. 5.2

[77] S. Agostinelli *et al.*, Nuclear Instruments and Methods in Physics Research Section A: Accelerators, Spectrometers, Detectors and Associated Equipment **506**, 250 (2003). 5.2

[78] GEANT: A simulation toolkit, NIM A 506 (2003), pp 205-303, `http://cern.ch/Geant4`. 5.2

[79] J. Zhu *et al.*, Grid Architecture for ALICE Experiment, in *The 14th International Conference on Advanced Communication Technology (ICACT)*, pp. 1209 –1214, IEEE, 2012. 5.3, 5.1

[80] P. Saiz *et al.*, Nuclear Instruments and Methods in Physics Research Section A: Accelerators, Spectrometers, Detectors and Associated Equipment **502**, 437 (2003), Proceedings of the VIII International Workshop on Advanced Computing and Analysis Techniques in Physics Research. 5.3

[81] S. Bagnasco *et al.*, Journal of Physics: Conference Series **119**, 062012 (2008). 5.3

[82] A. Kalweit, ALICE Collaboration, Journal of Physics G: Nuclear and Particle Physics **38**, 124073 (2011). 5.5.3

[83] B. Abelev *et al.*, ALICE Collaboration, (2013), arXiv:1301.4361. 5.7.2

[84] C. Mayer and E. Kryshen, Luminosity determination for central barrel upc triggers in pb–pb runs, ALICE Internal Note, 2012. 5.7.3, 5.16

[85] P. Söding, Phys. Lett. **19**, 702 (1966). 6.1

[86] M. Derrick *et al.*, ZEUS Collaboration, Z.Phys. **C69**, 39 (1995), arXiv:hep-ex/9507011. 6.1

[87] M. Klusek-Gawenda and A. Szczurek, Phys.Rev. **C87**, 054908 (2013), 1302.4204. 6.2.2

[88] C. Mayer, 2013, Private communication. 6.3.2, 6.4

[89] A. J. Baltz, Phys.Rev. **C71**, 024901 (2005), nucl-th/0409044. 7